DYNAMICAL FRICTION: FACT OR FICTION?

Dissertation

zur

Erlangung der naturwissenschaftlichen Doktorwürde
(Dr. sc. nat.)

vorgelegt der

Mathematisch-naturwissenschaftlichen Fakultät

der

Universität Zürich

von

Tobias Goerdt

aus

Deutschland

Promotionskomitee

Prof. Dr. Ben Moore (Vorsitz)
Prof. Dr. Daniel Wyler

Zürich, 2007

Contents

Zusammenfassung

Die vorliegende Doktorarbeit beschäftigt sich mit verschiedenen Effekten der dynamischen Reibung innerhalb von Kleinstgalaxien sowie deren Entstehung.

Das Zentrum der Fornax Zwergengalaxie, welche grösstenteils aus dunkler Materie besteht, wird von fünf Kugelsternhaufen in einem Abstand von ungefähr einem Kiloparsec umkreist. Besässe die Galaxie ein Halo aus kalter dunkler Materie mit einem zum Zentrum hin ansteigenden Dichteprofil (Spitze), wären die beobachteten Kugelsternhaufen schon innerhalb von wenigen Gigajahren im Zentrum der Galaxie versunken. Eine Erklärung für die Tatsache, dass diese bis zur heutigen Zeit überlebt haben, liefert ein flaches Halo aus dunkler Materie. Denn in dieser Konstellation dauert die Einsinkzeit der Kugelsternhaufen mehrere Hubblezeiten, wie numerische Simulationen und analytische Berechnungen zeigen. Die Kugelsternhaufen bleiben de facto am Rand des flachen Kerns stehen. Fornax besitzt also ein sehr seichtes inneres Dichteprofil. Die Grösse des Kernradius' lässt sich durch die Position des innersten Kugelsternhaufens bestimmen. Sollte sich die Phasenraumdichte des Kerns in ihrem Urzustand befinden, liesse dieses Dichteprofil auf warme dunkle Materie schliessen mit einer oberen Grenzmasse des dazugehörigen Teilchens von einem halben Kiloelektronenvolt. Dunkle Materie in diesem Massenbereich würde auch das Substrukturproblem lösen.

Satelliten, die in harmonische Kerne mit konstanter Dichte einsinken, durchleben anfangs eine Phase von sehr rapider (Super-Chandrasekhar) dynamischer Reibung, nach deren Ende sie keinerlei Reibung mehr ausgesetzt sind, wie analytische Berechnungen und N-Körper Simulationen zeigen. Im vorliegenden Spezialfall von harmonischen Potenzialen geschieht dies, weil sich die Hintergrundteilchen auf Epizyklen um den einfallenden Satelliten bewegen, da dort stabile Lösungen existieren. Das gesamte System bewegt sich schnell auf diese dauerhafte Konfiguration zu. Während dies geschieht, erfährt der Satellit einen kurzen Moment verstärkter Reibung. Sobald sich das System im Gleichgewicht befindet, gibt es keinen Impulsaustausch zwischen Hintergrundteilchen und Satellit mehr, sodass die Reibung verschwindet. Für Dichteprofile, die in ihrem Innern dem Potenzgesetz $\rho \propto r^{-\alpha}$ folgen, heizt der einfallende Satellit den Hintergrund auf und verringert somit den Wert von α. Für anfängliche Werte von $\alpha < 0.5$ erzeugt der Satellit einen kleinen Kern mit konstanter Dichte und bleibt, wie auch im Fall von $\alpha = 0$, stehen.

Die Existenz von Doppelkerngalaxien, wie VCC 128, die vor kurzem von

Debattista et al. (2006) beobachtet worden ist, stellt ein Problem für Modelle kalter dunkler Materie dar, weil diese Modelle eindeutig zentrale Spitzen vorhersagen. VCC 128 besitzt zwei dichte, fünfzig Parsec voneinander entfernte Sternhaufen. Die Zeitskala, welche die beiden Kernteile in Halos mit verschieden steilen Spitzen benötigen, um ins Zentrum einzusinken und dort zu verschmelzen, wird in der vorliegenden Arbeit untersucht. Die Einsinkzeit für den Fall eines Halos bestehend aus klassischer kalter dunkler Materie beträgt wenige Millionen Jahre. Deswegen scheint es sehr unwahrscheinlich, ein solches System beobachten zu können. Die statistische Auswertung solcher Systeme wird im Folgenden untersucht und damit die möglichen Werte für die innere Steigung der Dichteprofile von Galaxien eingeschränkt - schwächere Steigungen ergeben längere Reibungszeitskalen. Ausserdem gilt es zu bedenken, dass Doppelkerne ausschliesslich in Kernen mit konstanter Dichte längerfristig überleben können.

Sollte dunkle Materie aus Neutralinos bestehen, so bildeten sich als erste Strukturen spitze Halos aus kalter dunkler Materie. Sie formten sich bei einer Rotverschiebung $z \approx 100 - 50$ mit Massen $10^{-6} - 10^{-3}$ $M_\odot$. Die Überlebenschancen dieser Mikrohalos, die in unserer Galaxie den Gezeitenkräften von Sternen, Molekülwolken und anderer Substruktur aus dunkler Materie ausgesetzt sind, werden hier studiert. Mithilfe von N-Körper Simulationen wird die Gültigkeit von analytischen Berechnungen über die impulsive Aufheizung getestet. Ein grosser Nachteil der analytischen Kalkulationen ist, dass dort die durchschnittlich zugeführte Energie mit der durchschnittlichen Bindungsenergie anstelle des realen Massenverlustes des Systems verglichen wird. Dieses Energiekriterium führt zu einer Überschätzung der losgelösten Massen und zu einer Unterschätzung der Zerstörungszeitskala, da Halos aus kalter dunkler Materie in ihrem Inneren sehr stark gebunden sind. Zwar kann ein signifikanter Anteil des Materials von Mikrohalos aus kalter dunkler Materie durch Begegnungen mit galaktischer Substruktur oder Sternen losgelöst werden, die spitzen Zentralregionen bleiben jedoch intakt. Deswegen erwartet man eine signifikante gleichverteilte Komponente mit einer schmalen Signatur im Phasenraum, die mit direkten Experimenten entdeckt werden kann, sowie eine grosse Anzahl überlebender spitzer Kerne mit Eigenbewegungen von mehreren Bogensekunden pro Jahr, die indirekt über ihre Annihilation in Gammastrahlen entdeckt werden können.

Ultrakompakte Zwergengalaxien (UCDs) bilden eine neue, interessante

Galaxienklasse. Sie besitzen Ähnlichkeit zu sehr grossen Kugelsternhaufen. So wird denn auch für möglich erachtet, dass diese UCDs entstanden sind durch das Einsinken von Kugelsternhaufen via dynamischer Reibung und der daraus resultierenden Verschmelzung im Galaxienzentrum zu einem einzelnen, dichten Kern. Dieser Entstehungsprozess wird im Folgenden mithilfe von hochauflösenden numerischen Simulationen studiert. Es werden damit Dichteprofile und Halblichtradien erzeugt, die mit den beobachteten Werten sehr gut übereinstimmen. Allerdings hat dieses Entstehungsmodell zwei grosse Unstimmigkeiten: Die beobachteten UCDs sind heller und haben ein höheres Masse-zu-Licht-Verhältnis als die Vorhersagen aus der Simulation. Deswegen wird ein zweites mögliches Entstehungsszenario untersucht, welches besagt, dass UCDs die dichten Kerne von zerstörten Scheibengalaxien sind. Dies stimmt mit allen Beobachtungsdaten überein und liefert sogar eine Vorhersage über die radiale Verteilung von UCDs in Galaxienhaufen.

Summary

This thesis presents a study on the effect of dynamical friction in dwarf galaxies and their formation.

The dark matter dominated Fornax dwarf spheroidal has five globular clusters orbiting at $\sim 1\,\mathrm{kpc}$ from its centre. In a cuspy cold dark matter (CDM) halo the globulars would sink to the centre from their current positions within a few Gyr, presenting a puzzle as to why they survive undigested at the present epoch. A solution to this timing problem is to adopt a cored dark matter halo. Under these conditions, the sinking time becomes many Hubble times, as numerical simulations and analytic calculations show; the globulars effectively stall at the dark matter core radius. The Fornax dwarf spheroidal has a shallow inner density profile with a core radius constrained by the observed positions of its globular clusters. If the phase space density of the core is primordial then it implies a warm dark matter particle and gives an upper limit to its mass of $\sim 0.5\,\mathrm{keV}$, consistent with that required to significantly alleviate the substructure problem.

In constant density (harmonic) cores, sinking satellites undergo an initial phase of very rapid (super-Chandrasekhar) dynamical friction, after which they experience no dynamical friction at all, as analytic calculations and N-body simulations show. This occurs because, for the special case of harmonic potentials, there are stable solutions where the background particles move on epicycles about the in-falling satellite. The system moves rapidly into this stable configuration. In doing so, the satellite experiences a brief moment of enhanced friction. Once in equilibrium, there is no net momentum transfer between the background particles and the satellite and friction ceases. For density profiles with a central power law profile, $\rho \propto r^{-\alpha}$, the infalling satellite heats the background and causes α to decrease. For $\alpha < 0.5$ initially, the satellite generates a small central constant density core and stalls as in the $\alpha = 0$ case.

The existence of galaxies with binary nuclei, like VCC 128 observed recently by Debattista et al. (2006), provide a puzzle for cold dark matter models which ubiquitously predict central cusps. VCC 128 has two dense stellar clusters separated by 50 parsecs. The dynamical friction timescale is calculated for these two nuclei to sink and coalesce within different dark matter cuspy haloes. For a CDM halo, this should happen within a few million years, thus to observe this system in its current state appears to be unlikely.

The statistics of such systems is investigated and thus constraints are placed on the inner cusp slopes of the galaxies - shallower slopes give rise to longer friction timescales. Furthermore long lived binary nuclei can only exist in constant density cores - which again may be connected to the nature of the dark matter.

If the dark matter particle is a neutralino then the first structures to form are cuspy CDM haloes collapsing at redshifts $z \approx 100 - 50$ in the mass range $10^{-6} - 10^{-3}$ $\mathrm{M}_{\odot}$. A detailed study of the survival of these micro-haloes in the Galaxy is carried out as they experience tidal encounters with stars, molecular clouds, and other dark matter substructures. The validity of analytic impulsive heating calculations is tested using high resolution N-body simulations. A major limitation of analytic estimates is that mean energy inputs are compared to mean binding energies, instead of the actual mass lost from the system. This energy criterion leads to an overestimate of the stripped mass and underestimate of the disruption timescale since CDM haloes are strongly bound in their inner parts. A significant fraction of material from CDM micro-haloes can be unbound by encounters with Galactic substructure and stars, however the cuspy central regions remain relatively intact. Thus a significant smooth component with narrow features in phase space is expected, which may be uncovered by direct detection experiments, as well as numerous surviving cuspy cores with proper motions of arc-minutes per year, which can be detected indirectly via their annihilation into gamma-rays.

Ultra compact dwarf galaxies (UCDs) are a new and interesting class of galaxies that have some resemblance to very large globular clusters. Indeed, a popular formation mechanism for UCDs is via the sinking of globular clusters by dynamical friction, thus merging at the galactic centre to form a single dense nucleus. This process is studied with high resolution numerical simulations. It produces density profiles and half light radii which fit the observed UCDs very well. Unfortunately, this model has two major drawbacks. The observed UCDs are too luminous and have a mass-to-light ratio which is too high. Therefore a second possible formation scenario is investigated - that UCDs are the dense nuclei of stripped disk galaxies. This explanation seems to match all the observational constraints and also gives a prediction of their radial distribution in clusters.

1 Introduction

In this chapter, I provide general notions about cosmology, globular clusters and dark matter as well as the formation and evolution of cosmic structures within the context of the standard cosmological model, based on a spatially homogeneous and isotropic expanding universe. I will briefly review and discuss how dynamical friction and modern numerical computational techniques can be joined together to improve our understanding of the nature and evolution of the universe.

1.1 Cosmology

Cosmology, from the Greek: κοσμολογία [cosmologia, κόσμος (cosmos) order + λόγος (logos) word, reason, plan] is the quantitative (usually mathematical) study of the universe in its totality, and by extension, humanity's place in it. The study of the universe has a long history involving science, philosophy, esotericism, and religion.

Physical cosmology is the branch of physics and astrophysics that deals with the study of the physical origins of the universe and its nature on the very largest scales. In its earliest form it was what is now known as celestial mechanics, the study of the heavens. The Greek philosophers Aristarchus of Samos, Aristotle and Ptolemy proposed different cosmological theories. In particular, the geocentric Ptolemaic system was the accepted theory to explain the motion of the heavens until Nicolaus Copernicus, and subsequently Johannes Kepler and Galileo Galilei proposed a heliocentric system in the 16th century. This is known as one of the most famous examples of epistemological rupture in physical cosmology.

With Isaac Newton and the 1687 publication of Principia Mathematica, the problem of the motion of the heavens was finally solved. Newton provided a physical mechanism for Kepler's laws and his law of universal gravitation allowed the anomalies in previous systems, caused by gravitational interaction between the planets, to be resolved. A fundamental difference between Newton's cosmology and those preceding it was the Copernican principle that the bodies on earth obey the same physical laws as all the celestial bodies. This was a crucial philosophical advance in physical cosmology.

Modern scientific cosmology is usually considered to have begun in 1917 with Albert Einstein's publication of his final modification of general relativity in the paper "Cosmological Considerations of the General Theory of Relativity." General relativity prompted cosmogonists such as Willem de Sitter, Karl Schwarzschild and Arthur Eddington to explore the astronomical consequences of the theory, which enhanced the growing ability of astronomers to study very distant objects. The resolution of the debate on the structure of the cosmos came with the detection of novae in the Andromeda galaxy by Edwin Hubble in 1923 and 1924. Their distance established spiral nebulae well beyond the edge of the Milky Way and as galaxies of their own. Subsequent modelling of the universe explored the possibility that the cosmological constant introduced by Einstein in his 1917 paper may result in an expanding universe, depending on its value. Thus the big bang theory was proposed by the Belgian priest Georges Lemaître in 1927 which was subsequently corroborated by Edwin Hubble's discovery of the red shift in 1929 and later by the discovery of the cosmic microwave background radiation by Arno Penzias and Robert Woodrow Wilson in 1964. These findings were a first step to rule out some of many alternative physical cosmologies.

Recent observations made by the COBE and WMAP satellites observing this background radiation have effectively, in many scientists' eyes, transformed cosmology from a highly speculative science into a predictive science, as these observations matched predictions made by a theory called Cosmic inflation, which is a modification of the standard big bang theory. This has led many to refer to modern times as the "Golden age of cosmology".

1.2 The Friedmann-Lemaître universe

The idea that the universe should be uniform led to the formulation of the Cosmological Principle, on which most of the current cosmogonic pictures are based. In one of its versions, the Cosmological Principle states that the universe is homogeneous and isotropic in its spatial part. Under this assumption about the symmetry of the space-like hypersurfaces, it is possible to show that a system of coordinates can always be found in which the line element is written as:

$$\mathrm{d}s^2 = a^2 \left(\frac{\mathrm{d}r^2}{1 - kr^2} + r^2 \mathrm{d}\Omega^2 \right), \tag{1}$$

where $k = +1, 0, -1$ describes the curvature of space. With a suitable definition of the units of r, in the above expression the curvature constant k can be considered to have only three possible values; $k = 0$ for a spatially flat universe, $k = +1$ for a closed (positive curvature) universe and $k = -1$ for an open (negative curvature) universe. If the matter content of the universe can be described by a perfect fluid, such equations reduce to the system of two equations

$$H^2(t) \equiv \left(\frac{\dot{a}}{a}\right)^2 = \frac{8\pi G}{3}\rho - \frac{k}{a^2} + \frac{\Lambda}{3}, \tag{2}$$

$$-\frac{\ddot{a}}{a} = \frac{4\pi G}{3}(\rho + 3p) \tag{3}$$

where ρ is the density and $a(t)$ represents the cosmic expansion factor. This quantity gives the rate at which two points of fixed comoving coordinates r_1 and r_2 increase their distance as $a(t)$ increases and its time dependence leads to the Hubble constant $H(t)$. Determinations of the Hubble constant by using redshift-independent methods to measure galaxy distances give us

$$H(t_0) = 100h \mathrm{km\,s^{-1} Mpc^{-1}}, \tag{4}$$

where the Hubble parameter h is introduced to parametrise uncertainties in the determination of the distance-scale of the universe. The combined results of the WMAP satellite study of cosmic microwave background anisotropies, large-scale structure and type Ia supernovae observations (Bennet et al. 2003) yield a best fit value of the Hubble constant of $H(t_0) = 71$ km s^{-1} Mpc^{-1}. In equation (2), Λ represents the cosmological constant term which a number of recent observations indicate representing a substantial fraction of the total energy content of the universe (Spergel et al. 2003). Based on equation (3), we define the critical density $\rho_{\mathrm{c}}(t)$ corresponding to $k = \Lambda = 0$:

$$\rho_{\mathrm{c}} \equiv \frac{3H^2(t)}{8\pi G}, \tag{5}$$

such that density values ρ above, below or equal to ρ_{c} refer to closed, open or flat universes (in the absence of a cosmological constant term), respectively. Once the equation of state (i.e., the relation between energy density and pressure) is specified, the two Friedmann equations can be solved for the expansion factor $a(t)$. One of the fundamental consequences of the standard cosmological model is the prediction that the universe has undergone in the past a hot phase, during which the cosmic temperature took a much higher value than that, $T_0 \sim 2.7K$, which is today observed for the cosmic microwave background. The resulting cosmological framework of the hot Big Bang in a spatially homogeneous and isotropic universe is so widely accepted that it received the denomination of Standard Model (not to be confused with the Standard Model for electroweak interactions). Indications point in favour of this model and the most striking and direct supports can be summarised as follows (Kazantzidis 2005):

- The observed proportionality between the recession velocity of galaxies and their distance (Hubble law), which is a natural consequence of assuming the FLRW metric of equation (1).
- The detection and the high degree of isotropy of the cosmic microwave background radiation, which is the evidence of a primordial hot stage of the universe, characterised by a high degree of homogeneity
- The observed light element abundances, which match remarkably well the predictions of primordial nucleosynthesis, that represents an unavoidable step in the evolution of the hot universe.

1.3 Globular cluster

A globular cluster is a spherical collection of stars that orbits a galactic core as a satellite. Globular clusters are very tightly bound by gravity, which gives them their spherical shapes and relatively high stellar densities toward their centres. Globular clusters, which are found in the halo of a galaxy, contain considerably more stars and are much older than the less dense galactic, or open clusters, which are found in the disk. A globular cluster is sometimes known more simply as a globular; the word is derived from the Latin globulus (a small sphere). Globular clusters are fairly common; there are about 150 currently known globular clusters in the Milky Way, with perhaps 10-20 more undiscovered (Ashman et al. 1992). Large galaxies can have more: Andromeda, for instance, may have as many as 500 (Barmby & Huchra 2001). Some giant elliptical galaxies, such as M87 (Strom et al. 1981), may have as many as 10,000 globular clusters. These globular clusters orbit the galaxy out to large radii, 40 kiloparsec or more (Dauphole et al. 1996).

In contrast to open clusters, most globular clusters remain gravitationally-bound for time periods comparable to the life spans of the majority of their stars. (A possible exception is when strong tidal interactions with other large masses result in the dispersal of the stars.) At present the formation of globular clusters remains a poorly understood phenomenon. It remains uncertain whether the stars in a globular cluster form in a single generation, or are spawned across multiple generations over a period of several hundred million years. This star-forming period is relatively brief, however, compared to the age of many globular clusters. Observations of globular clusters show that these stellar formations arise primarily in regions of efficient star formation, and where the interstellar medium is at a higher density than in normal star-forming regions. Globular cluster formation is prevalent in starburst regions and in interacting galaxies (Elmegreen & Efremov 1999).

After they are formed, the stars in the globular cluster begin to gravitationally interact with each other. As a result the velocity vectors of the stars are steadily modified, and the stars lose any history of their original velocity. The characteristic interval for this to occur is the relaxation time. This is related to the characteristic length of time a star needs to cross the cluster as well as the number of stellar masses in the system. The value of the relaxation time varies by cluster, but the mean value is on the order of 10^9 years. Core-collapse is thought to occur when the more massive stars in a globular encounter their less massive companions. As a result of the encounters the larger stars tend to lose kinetic energy and start to settle toward the core. Over a lengthy period of time this leads to a concentration of massive stars near the core, a phenomenon called mass segregation.

Binary stars form a significant portion of the total population of stellar systems, with up to half of all stars occurring in binary systems. Numerical simulations of globular clusters have demonstrated that binaries can hinder and even reverse the process of core collapse in globular clusters. When a star in a cluster has a gravitational encounter with a binary system, a possible result is that the binary becomes more tightly bound and kinetic energy is added to the solitary star. When the massive stars in the cluster are sped up by this process, it reduces the contraction at the core and limits core collapse. When a globular cluster has a close encounter with a large mass, such as the core region of a galaxy, it undergoes a tidal interaction. The difference in the pull of gravity between the part of the cluster nearest the mass and the pull on the furthest part of the cluster results in a tidal force. A "tidal shock" occurs whenever the orbit of a cluster takes it through the plane of a galaxy.

As a result of a tidal shock, streams of stars can be pulled away from the cluster halo, leaving only the core part of the cluster. These tidal interaction effects create tails of stars that can extend up to several degrees of arc away from the cluster. These tails typically both precede and follow the cluster along its orbit. The tails can accumulate significant portions of the original mass of the cluster, and can form clump-like features. Tidal interactions add kinetic energy into a globular cluster, dramatically increasing the evaporation rate and shrinking the size of the cluster. Not only does tidal shock strip off the outer stars from a globular cluster, but the increased evaporation accelerates the process of core collapse. The same physical mechanism may be at work in dwarf spheroidal galaxies such as the Sagittarius dwarf, which appears to be undergoing tidal disruption due to its proximity to the Milky Way.

The distinction between cluster types is not always clear-cut, and objects have been found that blur the lines between the categories. For example, BH 176 in the southern part of the Milky Way has properties of both an open and a globular cluster (Ortolani, Bica & Barbuy 1995). Huxor et al. (2005) discovered a completely new type of star cluster in the Andromeda Galaxy, which is, in several ways, very similar to globular clusters. The new-found clusters contain hundreds of thousands of stars, a similar number of stars that can be found in globular clusters. The clusters also share other characteristics with globular clusters, e.g. the stellar populations and metalicity. What distinguishes them from the globular clusters is that they are much larger - several hundred light years across - and hundreds of times less dense. The distances between the stars are, therefore, much greater within the newly discovered extended clusters. Parametrically, these clusters lie somewhere between a (low dark-matter) globular cluster and a (dark matter-dominated) dwarf spheroidal galaxy. How these clusters are formed is not yet known, but their formation might well be related to that of globular clusters. Why M31 has such clusters, while the Milky Way does not, is not yet known. It is also unknown if any other galaxy contains these types of clusters, but it would be very unlikely that M31 is the sole galaxy with extended clusters.

1.4 Dark matter

Dark matter refers to hypothetical matter of unknown composition that does not emit or reflect enough electromagnetic radiation to be observed directly, but whose presence can be inferred from gravitational effects on visible matter. According to present observations of structures larger than galaxy-sized as well as Big Bang cosmology, dark matter accounts for the vast majority of mass in the observable universe. Fritz Zwicky used it for the first time to declare the observed phenomena consistent with dark matter observations as the rotational speeds of galaxies and orbital velocities of galaxies in clusters, gravitational lensing of background objects by galaxy clusters such as the Bullet cluster, and the temperature distribution of hot gas in galaxies and clusters of galaxies. Dark matter also plays a central role in structure formation and galaxy evolution, and has measurable effects on the anisotropy of the cosmic microwave background. All these lines of evidence suggest that galaxies, clusters of galaxies, and the universe as a whole contain far more matter than that which interacts with electromagnetic radiation: the remainder is called the "dark matter component".

The composition of dark matter is unknown, but may include ordinary and heavy neutrinos, recently postulated elementary particles such as WIMPs and axions, astronomical bodies such as dwarf stars and planets (collectively called MACHOs), and clouds of non-luminous gas. Current evidence favours models in which the primary component of dark matter is new elementary particles, collectively called non-baryonic dark matter. The dark matter component has vastly more mass than the "visible" component of the universe. At present, the density of ordinary baryons and radiation in the universe is estimated to be equivalent to about one hydrogen atom per cubic metre of space. Only about 4% of the total energy density in the universe (as inferred from gravitational effects) can be seen directly. About 22% is thought to be composed of dark matter. The remaining 74% is thought to consist of dark energy, an even stranger component, distributed diffusely in space. Some hard-to-detect baryonic matter makes a contribution to dark matter, but constitutes only a small portion. Determining the nature of this missing mass is one of the most important problems in modern cosmology and particle physics. It has been noted that the names "dark matter" and "dark energy" serve mainly as expressions of our ignorance, much as the marking of early maps with "terra incognita".

The first to provide evidence and infer the existence of a phenomenon that has come to be called "dark matter" was Swiss astrophysicist Fritz Zwicky in 1933. He applied the virial theorem to the Coma cluster of galaxies and obtained evidence of unseen mass. Zwicky estimated the cluster's total mass based on the motions of galaxies near its edge. When he compared this mass estimate to one based on the number of galaxies and total brightness of the cluster, he found that there was about 400 times more mass than expected.

The gravity of the visible galaxies in the cluster would be far too small for such fast orbits, so something extra was required. This is known as the "missing mass problem". Based on these conclusions, Zwicky inferred that there must be some non-visible form of matter which would provide enough of the mass and gravity to hold the cluster together.

Much of the evidence for dark matter comes from the study of the motions of galaxies. Many of these appear to be fairly uniform, so by the virial theorem the total kinetic energy should be half the total gravitational binding energy of the galaxies. Experimentally, however, the total kinetic energy is found to be much greater: in particular, assuming the gravitational mass is due to only the visible matter of the galaxy, stars far from the centre of galaxies have much higher velocities than predicted by the virial theorem. Galactic rotation curves, which illustrate the velocity of rotation versus the distance from the galactic centre, cannot be explained by only the visible matter. Assuming that the visible material makes up only a small part of the cluster is the most straightforward way of accounting for this. Galaxies show signs of being composed largely of a roughly spherically symmetric, centrally concentrated halo of dark matter with the visible matter concentrated in a disc at the centre. Low surface brightness dwarf galaxies are important sources of information for studying dark matter, as they have an uncommonly low ratio of visible matter to dark matter, and have few bright stars at the centre which impair observations of the rotation curve of outlying stars.

Clowe et al. (2006) observed dark separate from ordinary matter through measurements of the Bullet Cluster, actually two nearby clusters of galaxies that collided about 150 million years ago (Markevitch et al. 2004). They analysed the effects of gravitational lensing to determine total mass distribution in the pair and compared that to X-ray maps of hot gases, thought to constitute the large majority of ordinary matter in the clusters. The hot gases interacted during the collision and remain closer to the centre. The individual galaxies and the dark matter did not interact and are farther from the centre.

There are places where dark matter seems to be a small component or totally absent. Globular clusters show no evidence that they contain dark matter, though their orbital interactions with galaxies do show evidence for galactic dark matter. For some time, measurements of the velocity profile of stars seemed to indicate concentration of dark matter in the disk of the Milky Way galaxy, however, now it seems that the high concentration of baryonic matter in the disk of the galaxy (especially in the interstellar medium) can account for this motion. Galaxy mass profiles are thought to look very different from the light profiles. The typical model for dark matter galaxies is a smooth, spherical distribution in virialized halos. Such would have to be the case to avoid small-scale (stellar) dynamical effects.

Another important tool for future dark matter observations is gravitational lensing. Lensing relies on the effects of general relativity to predict masses without relying on dynamics, and so is a completely independent means of measuring the dark matter. Strong lensing, the observed distortion of background galaxies into arcs when the light passes through a gravitational lens, has been observed around a few distant clusters including Abell 1689. By measuring the distortion geometry, the mass of the cluster causing the phenomena can be obtained. In the dozens of cases where this has been done, the mass-to-light ratios obtained correspond to the dynamical dark matter measurements of clusters.

Perhaps more convincing, a technique has been developed over the last 10 years called weak lensing which looks at microscale distortions of galaxies observed in vast galaxy surveys due to foreground objects through statistical analyses. By examining the shear deformation of the adjacent background galaxies, astrophysicists can characterise the mean distribution of dark matter by statistical means and have found mass-to-light ratios that correspond to dark matter densities predicted by other large-scale structure measurements. The correspondence of the two gravitational lens techniques to other dark matter measurements has convinced almost all astrophysicists that dark matter actually exists as a major component of the universe's composition.

Dark matter is crucial to the Big Bang model of cosmology as a component which corresponds directly to measurements of the parameters associated with Friedmann cosmology solutions to general relativity. In particular, measurements of the cosmic microwave background anisotropies correspond to a cosmology where much of the matter interacts with photons more weakly than the known forces that couple light interactions to baryonic matter. Likewise, a significant amount of non-baryonic, cold matter is necessary to explain the large-scale structure of the universe.

Observations suggest that structure formation in the universe proceeds hierarchically, with the smallest structures collapsing first and followed by galaxies and then clusters of galaxies. As the structures collapse in the evolving universe, they begin to "light up" as the baryonic matter heats up through gravitational contraction and the object approaches hydrostatic pressure balance. Ordinary baryonic matter had too high a temperature, and too much pressure left over from the big bang to collapse and form smaller structures, such as stars, via the Jeans instability. Dark matter acts as a compactor of structure. This model not only corresponds with statistical surveying of the visible structure in the universe but also corresponds precisely to the dark matter predictions of the cosmic microwave background. This bottom up model of structure formation requires something like cold dark matter to succeed. Large computer simulations of billions of dark matter particles have been used to confirm that the cold dark matter model of structure formation is consistent with the structures observed in the universe through galaxy surveys, such as the Sloan Digital Sky Survey and 2dF Galaxy Redshift Survey, as well as observations of the Lyman-alpha forest. These studies have been crucial in constructing the Lambda-CDM model which measures the cosmological parameters, including the fraction of the universe made up of baryons and dark matter.

Data from a number of lines of evidence, including galaxy rotation curves, gravitational lensing, structure formation, and the fraction of baryons in clusters and the cluster abundance combined with independent evidence for the baryon density, indicate that 85-90% of the mass in the universe does not interact with the electromagnetic force. This "dark matter" is evident through its gravitational effect. Several categories of dark matter have been postulated.

- Baryonic dark matter
- Non-baryonic dark matter which is divided into three different types:
    - Hot dark matter - nonbaryonic particles that move ultrarelativistically (Umemura & Ikeuchi 1985)
    - Warm dark matter - nonbaryonic particles that move relativistically
    - Cold dark matter - nonbaryonic particles that move non relativistically (Vittorio & Silk 1984)

Davis et al. wrote in 1985: Candidate particles can be grouped into three categories on the basis of their effect on the fluctuation spectrum (Bond et al. 1983). If the dark matter is composed of abundant light particles which remain relativistic until shortly before recombination, then it may be termed "hot". The best candidate for hot dark matter is a neutrino [..]

A second possibility is for the dark matter particles to interact more weakly than neutrinos, to be less abundant, and to have a mass of order 1eV. Such particles are termed "warm dark matter", because they have lower thermal velocities than massive neutrinos [..] there are at present few candidate particles which fit this description. Gravitinos and photinos have been suggested (Pagels and Primack 1982; Bond, Szalay and Turner 1982) [..] Any particles which became nonrelativistic very early, and so were able to diffuse a negligible distance, are termed "cold" dark matter (CDM). There are many candidates for CDM including supersymmetric particles

The Concordance Model requires that, to explain structure in the universe, it is necessary to invoke cold (non-relativistic) dark matter. Large masses, like galaxy-sized black holes can be ruled out on the basis of gravitational lensing data. Possibilities involving normal baryonic matter include brown dwarfs or perhaps small, dense chunks of heavy elements; such objects are known as massive compact halo objects, or "MACHOs". However, studies of big bang nucleosynthesis have convinced most scientists that baryonic matter such as MACHOs cannot be more than a small fraction of the total dark matter.

At present, the most common view is that dark matter is primarily non-baryonic, made of one or more elementary particles other than the usual electrons, protons, neutrons, and known neutrinos. The most commonly proposed particles are axions, sterile neutrinos, and WIMPs (Weakly Interacting Massive Particles, including neutralinos). None of these are part of the standard model of particle physics, but they can arise in extensions to the standard model. Many supersymmetric models naturally give rise to stable WIMPs in the form of neutralinos. Heavy, sterile neutrinos exist in extensions to the standard model that explain the small neutrino mass through the seesaw mechanism.

1.5 The ΛCMD model

ΛCDM is an abbreviation for Λ-Cold Dark Matter. It is frequently referred to as the concordance model of big bang cosmology, since it attempts to explain cosmic microwave background observations, as well as large scale structure observations and supernovae observations of the accelerating expansion of the universe. It is the simplest known model that is in general agreement with observed phenomena.

Λ stands for the cosmological constant which is a dark energy term that allows for the current accelerating expansion of the universe. The cosmological constant is often described in terms of Ω_Λ, the fraction of the energy density of a flat universe in the form of the cosmological constant. Currently, $\Omega_\Lambda \simeq 0.74$, implying 74% of the energy density of the present universe is in this form. Cold dark matter is the model where the dark matter is explained as being cold (i.e. not thermalized), non-baryonic, collisionless dust. This component makes up 22% of the energy density of the present universe. The remaining 4% is all of the matter and energy that makes up the atoms and photons that are the building blocks of planets, stars, and gas clouds in the universe.

The model assumes a nearly scale-invariant spectrum of primordial perturbations and a universe without spatial curvature. It also assumes that it has no observable topology, so that the universe is much larger than the observable particle horizon. These are predictions of cosmic inflation. These are the simplest assumptions for a consistent, physical model of cosmology. However, ΛCDM is a model. Cosmologists anticipate that all of these assumptions will not be borne out exactly, after more is learned about the applicable fundamental physics. In particular, cosmic inflation predicts spatial curvature at the level of 10^{-4} to 10^{-5}. It would also be surprising if the temperature of dark matter were absolute zero. Moreover, ΛCDM says nothing about the fundamental physical origin of dark matter, dark energy and the nearly scale-invariant spectrum of primordial curvature perturbations: in that sense, it is merely a useful parameterisation of ignorance.

The model has six parameters. The Hubble constant determines the rate of expansion of the universe, as well as the critical density for closure of the universe, ρ_0. Densities for baryons, dark matter and dark energy are given as Ω_s, which are the ratio of the true density to the critical density: e.g. $\Omega_\mathrm{b} = \rho_\mathrm{b}/\rho_0$. Since the ΛCDM model assumes a flat universe, these densities sum to one, and the density of dark energy is not a free parameter. The optical depth to reionization determines the red shift of reionization. Information about the density fluctuations is determined by the amplitude of the primordial fluctuations (from cosmic inflation) and the spectral index, which measures how the fluctuations change with scale ($n_\mathrm{s} = 1$ corresponds to a scale-invariant spectrum).

One of the major shortcomings of any CDM model is the difficulty in

Parameter	Value	Description
H_0	70.9 km $s^{-1}Mpc^{-1}$	Hubble Parameter
Ω_b	0.0444	Baryon density
Ω_m	0.276	Total matter density
τ	0.079	Optical depth to reionization
A_s	0.813	Scalar fluctuation amplitude
n_s	0.948	Scalar spectral index
ρ_0	0.94×10^{-26} kg m^{-3}	Critical density
Ω_Λ	0.732	Dark energy density
z_{ion}	10.5	Reionization red-shift
σ_8	0.772	Galaxy fluctuation amplitude
t_0	13.73 Gyr	Age of the universe

Table 1: The 6 basic plus 5 derived parameters of the concordance ΛCDM theory.

matching the steep observed luminosity function with the flat mass spectrum of haloes predicted from simulations or Press-Schechter models. From cosmological N-body simulations this problem manifests itself as a lack of observed substructure in the vicinity of our Milky Way and other galaxies. Several alternative dark matter candidates have been proposed to address this and related problems, such as the harmonic core at the centre of the Fornax dwarf spheroidal, many of which can be tested using observations of galaxies on small scales. An alternative cosmology, which provides a natural explanation for the lack of substructure, is warm dark matter, which introduces an additional free parameter - the free streaming scale.

1.6 Galaxy formation

The formation and evolution of galaxies is still one of the most active research areas in cosmology. Some ideas, however, have gained wide acceptance. Galaxy formation is presently believed to proceed directly from structure formation theories, formed as a result of tiny quantum fluctuations in the wake of the Big Bang. N-body simulations have been able to predict the types of structures, morphologies, and distribution of galaxies which we observe today both in our present universe, and - by examining distant galaxies - in the early universe.

Above I have briefly discussed the dynamics of a homogeneous universe. Clearly, the observed universe is far from being homogeneous - there is an enormous richness of structure ranging from dwarf galaxies, to groups and clusters of galaxies, and finally to huge superclusters. For the observer, galaxies appear as islands of stars, with stellar densities 10^8 times larger than the mean stellar density. Their typical size is roughly 10 kpc, yet their average distance is of order 1 Mpc. Nevertheless, the common assumption is that on scales somewhat larger than 100 Mpc homogeneity is approached. If the universe is smoothed on larger scales, it will appear homogeneous. Despite its small-scale lumpiness the global dynamics of the universe can still be described by the Friedmann-Lemaître models.

The currently favoured theories of structure formation in the universe assume that the structure grows due to gravitational instability out of the primordial density fluctuations. Note that these theories are in principle completely specified by their initial conditions. In the simplest case, there are already fully given by the form of the initial fluctuation spectrum, and by the values of the cosmological parameters. However, the problem encountered in practice is that it is highly non-trivial to compare the predictions of such a model (the clustering of dark matter) with the objects that are actually observed (galaxies).

At this point, it is worth pointing out that the dominant interaction that governs the dynamics and evolution of galaxies, stellar systems in general, and of large-scale structure in the universe is gravitation. Although dissipative gas physics is clearly important for galaxy formation, it likely plays only a minor role for the structure of elliptical galaxies, for cluster of galaxies, for the dynamics of large-scale structure, and the other gas-poor objects. The relative importance of the gravitational interaction is corroborated since it appears that the majority of the mass in the universe consists of dark matter, which has been detected only by its gravitational interactions. Modern cosmology assumes that there is a class of yet unidentified particles contributing as dark matter to the mass density. While the dark matter has not been directly detected on earth so far, there is a lot of indirect evidence that demonstrates its existence. This indirect evidence stems from the dark matter's gravitational effects on its surroundings, seen for example in the orbital motions of galaxies within clusters, or in the rotation curves of galaxies, or in the kinematics of their satellites.

The dark matter is believed to interact with other matter only by gravity. This idea brings a great simplification, because the dynamics of the dark matter can then be studied using the laws of gravity alone, without having to worry about the much more complicated physical processes related to gas that ultimately forms the stars in the visible parts of the galaxies. The study of the growth of density perturbations under their self-gravity in an expanding universe is therefore one of the major topics in cosmology. As long as the fluctuations are small, the equations of motion can be linearised by expanding around the homogeneous solution. The resulting linear theory together with its higher-order extensions are among the best methods to study the formation of large-scale structure. However, especially in the context of galaxy formation, analytic techniques are severely limited by the inherently nonlinear character of gravity. In galaxies, the mean density is more than $\sim 10^7$ times larger than the background density, making linear theory useless. There are a few special analytic solutions for the nonlinear collapse of structures, most notably the spherical collapse model. While these solutions offer invaluable insight into the relevant dynamics, they provide no adequate description for the highly asymmetric processes in hierarchical galaxy formation.

Consequently, direct numerical simulation of the gravitational dynamics has become an indispensable tool in cosmology. At the heart of these methods lies the gravitational N-body problem, which describes the dynamics of a collection of N point particles under their mutual gravity. For example, the stars in a galaxy, or the dark matter particles in the universe are often modelled as N-body systems.

After the Big Bang, the universe had a period when it was remarkably homogeneous, as can be observed in the Cosmic Microwave Background, the fluctuations of which are less than one part in one hundred thousand. All the structure we observe today was formed as a consequence of the growth of primordial fluctuations. The primordial fluctuations caused gas to be attracted to areas of denser material, hierarchically forming superclusters, clusters, galaxies, star clusters and stars. One consequence of this model is that the location of galaxies indicates areas of higher density of the early universe. Hence the distribution of galaxies is closely related to the physics of the early universe. The observed components of galaxies (including our own Milky Way) that must be explained in, or at least not be at odds with, a theory of galactic evolution, include:

- the stellar disk is quite thin, dense, and rotates
- the stellar halo is very large, sparse, and does not rotate (or has perhaps

even a slight retrograde rotation), with no apparent substructure

- halo stars are typically much older and have much lower metalicities than disk stars (there is a correlation, but there is no absolute connection between these data)
- some astronomers have identified an intermediate population of stars, variously called the "metal weak thick disk", the "intermediate population II". If these are indeed a distinct population, they would be described as metal-poor (but not as poor as the halo stars), old (but not as old as the halo stars), and orbiting very near the disk, in a sort of "puffed-up", thicker disk shape.
- globular clusters are typically old and metal-poor as well, but there are a few which are not nearly as metal-poor as most, and/or have some younger stars. Some stars in globular clusters appear to be as old as the universe itself (by entirely different measurement and analysis methods)!
- in each globular cluster, all the stars were born at virtually the same time (except for a few globulars that show multiple epochs of star formation)
- globular clusters with smaller orbits (closer to the galactic centre) have orbits which are somewhat flatter (less inclined to the disk), and less eccentric (more circular), while those further out have orbits in all inclinations, and tend to be more eccentric.
- High Velocity Clouds, clouds of neutral hydrogen are "raining" down on the galaxy, and presumably have been from the beginning (these would be the necessary source of a gas disk from which the disk stars formed).

The earliest modern theory of the formation of our galaxy (known by astronomers as ELS (Eggen, Lynden-Bell & Sandage 1962) describes a single (relatively) rapid monolithic collapse, with the halo forming first, followed by the disk. Another view (Searle & Zinn 1978) describes a more gradual process, with smaller units collapsing first, then later merging to form the larger components. An even more recent idea is that significant portions of the stellar halo could be stellar debris from destroyed dwarf galaxies and globular clusters that once orbited the Milky Way. The halo would then be a "new"er component made of "recycled" old parts. In recent years, a great deal of focus has been put on understanding merger events in the evolution of galaxies. Rapid technological progress in computers have allowed much better simulations of galaxies, and improved observational technologies have provided much more data about distant galaxies undergoing merger events.

Giant elliptical galaxies are probably formed by mergers on a grander scale. In the Local Group, the Milky Way and M31 (the Andromeda Galaxy) are gravitationally bound, and currently approaching each other at high speed. Since we cannot determine the speed of M31 perpendicular to the line from us to it, we do not know if it will collide with the Milky Way. If the two galaxies do meet they will pass through each other, with gravity distorting both galaxies severely and ejecting some gas, dust and stars into intergalactic space. They will travel apart, slow down, and then again be drawn towards each other, and again collide. Eventually both galaxies will have merged completely, streams of gas and dust will be flying through the space near the newly formed giant elliptical galaxy. Out of the gas ejected from the merger, new globular clusters and maybe even new dwarf galaxies may form and become the halo of the elliptical. The globulars from both M31 and the Milky Way will also form part of the halo; globulars are so tightly held together that they are largely immune to large scale galactic interactions. On the stellar scale, little will happen. If anybody is around to watch the merger, it will be a slow, but magnificent event, with the sight of a distorted M31 spectacularly spanning the entire sky. M31 is actually already distorted: the edges are warped. This is probably because of interactions with its own galactic companions, as well as possible mergers with dwarf spheroidal galaxies in the recent past - the remnants of which are still visible in the disk populations.

In our epoch, large concentrations of galaxies (clusters and superclusters) are still assembling. This "bottom-up" picture is referred to as hierarchical structure formation [similar to the Searle & Zinn (1978) picture of galaxy formation, on a larger scale]. While we have learned a great deal about our and other galaxies, the most fundamental questions about formation and evolution remain only tentatively answered.

Dwarf galaxies, the observed counterparts to dark matter substructures provide a fascinating testbed for constraining such dark matter candidates. This is especially important today, since galaxy dynamics belongs to the strongest methods to test dark matter candidates due to the lack of confirmation of a signal from direct and indirect detection experiments which attempt to measure the neutralino properties.

1.7 Dynamical friction

Dynamical friction is a term related to loss of momentum and kinetic energy of moving bodies through a gravitational interaction with surrounding matter in space. It is sometimes referred to as gravitational drag, and was first discussed in detail by Subrahmanyan Chandrasekhar in 1943.

The mentioned effect must exist according to the principle of conservation of (potential and kinetic) energy and to the principle of conservation of momentum. The momentum is conserved as any gravitational interactions between two or more bodies correspond to elastic collisions between those bodies. E.g. when a heavy body B moves through a cloud of lighter bodies, the gravitational interaction between B and the light bodies causes the light bodies to accelerate and gain momentum and kinetic energy. Since energy and momentum are conserved, B has to lose a part of its momentum and energy equal to the sums of all momenta and energies gained by the light bodies. Because of the loss of momentum and kinetic energy of the body under consideration the effect is called dynamical friction. The greater the density of the surrounding media, the stronger the force from dynamical friction. Similarly, the force is proportional to the square of the mass of the object. The force is also proportional to the inverse square of the velocity. This means the fractional rate of energy loss drops rapidly at high velocities.

Dynamical friction is particularly important in the formation of planetary systems and interactions between galaxies. During the formation of planetary systems, dynamical friction between the protoplanet and the protoplanetary disk causes energy to be transferred from the protoplanet to the disk. This results in the inward migration of the protoplanet. When galaxies interact through collisions, dynamical friction between stars causes matter to sink toward the centre of the galaxy and for the orbits of stars to be randomised. This process is called violent relaxation and can change two spiral galaxies into one larger elliptical galaxy.

1.7.1 The Chandrasekhar picture

One way of thinking about this process is that the light bodies near the heavy body B are attracted by its gravity toward its position and therefore the density at that location increases and is referred to as a gravitational wake. In the meantime, B has moved forward. Therefore, the gravitational attraction of the wake pulls B backward and slows it down. Of course the mechanism works the same for all masses of interacting bodies and for any relative velocities between them. However, while in the above case the most probable outcome is the loss of momentum and energy by the body under consideration, in the general case it might be either loss or gain (when one body loses momentum and energy in an elastic collision the other one gains them).

Consider the motion of a system B with mass M through a medium consisting of many individual 'particles' of mass $m \ll M$. As an example, think of a satellite galaxy moving through the dark matter halo of its parent galaxy. Due to gravitational focusing M creates an overdensity of particles behind its path (the wake). The backreaction of this wake on M is called dynamical friction and causes M to slow down. Consequently, energy is transferred from the massive to the less massive bodies: dynamical friction is a manifestation of mass segregation.

Assuming, for simplicity, a uniform density medium with an isotropic velocity distribution $f(v_{\mathrm{m}})$ of the particles $m \ll M$, then

$$\underline{F}_{\mathrm{df}} = M\frac{\mathrm{d}\underline{v}_{\mathrm{M}}}{\mathrm{d}t} = -\frac{4\pi G^2 M^2}{v_{\mathrm{M}}^2}\ln\Lambda\rho(< v_{\mathrm{M}}) \tag{6}$$

with $\ln\Lambda$ the Coulomb logarithm and

$$\rho(< v_{\mathrm{M}}) = 4\pi\int_0^{v_{\mathrm{M}}} f(v_{\mathrm{m}})v_{\mathrm{m}}^2\mathrm{d}v_{\mathrm{m}} \tag{7}$$

the mass density of background particles with velocities $v_{\mathrm{m}} < v_{\mathrm{M}}$. The derivation of this equation (see Binney & Tremaine 1987) is due to Chandrasekhar (1943), and one therefore often speaks of Chandrasekhar dynamical friction. The full dynamical friction formula then becomes

$$\underline{F}_{\mathrm{dyn}} = -\frac{4\pi\ln\Lambda G^2\rho M^2}{\nu_{\mathrm{M}}^3}\left[\mathrm{erf}\left(\frac{\nu}{\sqrt{2}\sigma}\right) - \frac{\sqrt{2}\nu}{\sigma\sqrt{\pi}}\mathrm{exp}\left(\frac{\nu^2}{2\sigma^2}\right)\right]\underline{v}_{\mathrm{M}}, \tag{8}$$

where G is the gravitational constant, M is the mass of the moving object, ρ is the density, and v_{M} is the velocity of the object in the frame in which the surrounding matter was initially at rest (Carroll & Ostlie 1996). Note that $\underline{F}_{\mathrm{df}} \propto M^2$: the amount of material that is deflected (i.e. the 'mass' of the wake) is proportional to M and the gravitational force that this wake exerts on M is proportional to M times its own mass. Note that $\underline{F}_{\mathrm{df}} \propto v_{\mathrm{M}}^{-2}$ in the limit of large $v_{\rm M}$, but $\underline{F}_{\rm df} \propto v_{\rm M}$ in the limit of small $v_{\rm M}$ [i.e. for sufficiently small $v_{\rm M}$ one may replace $f(v_{\rm m})$ with $f(0)$]. Note that $\underline{F}_{\rm df}$ is independent of m!

One has that $\Lambda = b_{\rm max}/b_{\rm min}$ with $b_{\rm min}$ and $b_{\rm max}$ the minimum and maximum impact parameters for which encounters can be considered effective: Encounters with $b > b_{\rm max}$ do not cause a significant deflection, and these therefore do not contribute significantly to the wake. Encounters with $b < b_{\rm min}$ cause very strong deflection so that these also do not contribute to the wake. We can estimate $b_{\rm min}$ as the impact parameter that corresponds to a close encounter, and thus $b_{\rm min} \simeq GM/ < v^2 >$ with $< v^2 >^{1/2}$ the rms velocity of the background particles. The maximum impact parameter, $b_{\rm max}$, is much harder to estimate (see White 1976), and one typically takes $b_{\rm max} \simeq L$ with L the size of the system. Typical values that one encounters for the Coulomb Logarithm are $3 \lesssim \ln\Lambda \lesssim 30$. Note that Chandrasekhar Dynamical Friction is a purely local phenomenon: The dynamical friction force $\underline{F}_{\rm df}$ depends only on the local density $\rho(< v)$, and the backreaction owes to a local phenomenon, namely wake-creation due to gravitational focusing.

1.7.2 The Weinberg picture

However, a system A can also experience dynamical friction due to a system B when it is located outside of B (Lin & Tremaine 1983). Clearly, this friction cannot arise from a wake. Instead, it arises from torques between A and particles in B that are in resonance with A. Further on, it can be shown that the frictional effects arise entirely from near resonant particles.

Tremaine & Weinberg (1984) and Weinberg (1986) formulated a perturbative theory of dynamical friction which could be applied to spherical systems. Notice from equation (8), that most of the dynamical friction originates from particles with large impact parameters: it is the accumulation of many long range *small* interactions which leads to most of the dynamical friction; not the large angle scattering of close encounters. This is why perturbative methods can be used. Together they consider a general, small, perturbation to a single background particle; and then sum over all particles in the system to obtain to total torque induced on the perturber.

The two main assumptions are: (i) that the perturbation is small and (ii) that the frequency of the perturber changes with time, $\Omega_{\rm s} = \Omega_{\rm s}(t)$, *faster than the perturbation can grow non-linear.* For most potentials of interest this second assumption is satisfied. The perturber (the GC) will lose angular momentum to the background particles as a result of the dynamical friction, and Ω_s will then increase as the GC falls inwards.

Under this assumptions, the perturbation method gives us new physical insight into the dynamical friction problem. To the order of the perturbation approximation, *all* of the torque comes from background particles which are close to resonance with the perturber. Non-resonant particles do not contribute to the friction at all. This is a key difference between the perturbation solution and that of equation (8).

The essence of this perturbative approach to dynamical friction can be understood in the following way: consider a spherical potential, $\Phi(r)$, to which a small *non-axisymmetric* perturbation, Φ_s, is applied. The perturbation rotates with angular frequency Ω_s. In this case, the equations of motion of a test particle moving in a frame stationary with respect to the perturbation are given by:

$$\underline{\ddot{r}} + \underline{\nabla}[\Phi + \Phi_\mathrm{s}] + 2\underline{\Omega}_\mathrm{s} \times \underline{\dot{r}} + \underline{\Omega}_\mathrm{s} \times (\underline{\Omega}_\mathrm{s} \times \underline{r}) = 0 \tag{9}$$

where the third and fourth terms are the familiar Coriolis and Centrifugal inertial forces respectively.

The problem is symmetric about the plane containing the perturbation, so it makes sense to work in cylindrical coordinates: $\underline{r} = \underline{r}(R, \phi, z)$. Equation (9) then reduces to:

$$\ddot{R} - R\dot{\phi}^2 = -\frac{\partial[\Phi + \Phi_\mathrm{s}]}{\partial R} + 2R\dot{\phi}\Omega_\mathrm{s} + \Omega_\mathrm{s}^2 R \tag{10}$$

$$R\ddot{\phi} + 2\dot{R}\dot{\phi} = -\frac{1}{R}\frac{\partial \Phi_\mathrm{s}}{\partial \phi} - 2\dot{R}\Omega_\mathrm{s} \tag{11}$$

and equation (11) can be rearranged to give:

$$\frac{d}{dt}\left(R^2\dot{\phi}\right) = \dot{J}_\mathrm{z} = -\frac{\partial \Phi_\mathrm{s}}{\partial \phi} - 2R\dot{R}\Omega_\mathrm{s} \tag{12}$$

where J_z is the z-component of the specific angular momentum of the test particle and we have introduced the notation $\Omega_\mathrm{s} = |\underline{\Omega}_\mathrm{s}|$; and similarly for other vectors.

In order to solve equation (12), we have to specify the perturbation, $\Phi_\mathrm{s}(R, \phi)$, and the angular motion of the test particle, $\phi(t)$. While it is not necessary in general, it also greatly simplifies the analysis to assume that $\dot{R} = 0$, which we do from here on. With this assumption, we can still illustrate usefully the key points of the perturbation method.

We consider the perturbation: $\Phi_\mathrm{s} = A\mathrm{e}^{\mathrm{im}\phi}$. This is instructive since it is then one component of a more general Fourier series sum. We can find $\phi(t)$ if we assume that the perturbation is small. The usual trick is to suppose that over short times the particle trajectory is the same as in the unperturbed case. For the *unperturbed* case, $\Phi_\mathrm{s}, \Omega_\mathrm{s} \rightarrow 0$ and equation (12) gives: $\phi_{in} = \Omega_* t + \mathrm{const}$; where the subscript *in* reminds us that this is now with respect to an inertial frame. Transforming ϕ_in to the non-inertial frame rotating with Ω_s, gives: $\phi = (\Omega_* - \Omega_\mathrm{s})t + \mathrm{const}$.

Equation (12) may now be integrated to give:

$$J_z = -\mathrm{Re}\left\{\frac{A\exp[im(\Omega_* - \Omega_\mathrm{s})t]}{(\Omega_* - \Omega_\mathrm{s})}\right\} - R^2\Omega_\mathrm{s} \tag{13}$$

It is clear from equation (13) that J_z just oscillates with no time averaged change[1] (i.e. no dynamical friction) unless $\Omega_* = \Omega_\mathrm{s}$. At this *resonant* frequency the test particle appears to have a pathological specific angular momentum. In practise this just means that the approximation that the perturbation is small fails.

Tremaine & Weinberg (1984) show that if $\Omega_\mathrm{s} = \Omega_\mathrm{s}(t)$, then this problem can be solved. Provided Ω_s changes faster than the time taken for the perturbation to grow into the non-linear regime, then we can sum over all of the resonant interactions from the background particles and calculate the resulting torque on the perturber[2]. There are two regimes of interest: fast and slow passages through resonance. The fast passage through resonance recovers the LBK torque formula (Lynden-Bell & Kalnajs 1972). This is the perturbation theory equivalent of equation (8): it describes the dynamical friction. For slow passages through resonance, Tremaine & Weinberg (1984) find quite different behaviour. The torque is stronger than in the LBK case, reversible, and can lead to the capture (gravitational binding) of background particles by the perturber. These differences led Tremaine & Weinberg (1984) to refer to this as *dynamical feedback*, rather than friction.

The extent to which dynamical friction is a local (wake) versus global

---

[1] Recall that we have assumed that $R = \mathrm{const}$.

[2] Note that there is now an extra term which should also be included in equation 9: $\underline{\dot{\Omega}} \times \underline{r}$; we assume that this is small.

(resonant-coupling) effect is still being debated.

1.8 N-body simulations

A complete description of the processes of formation and evolution of cosmic structures is very complicated and far from having reached a satisfactory level of explanation. Formation of galaxies and galaxy clusters involves both gravitational dynamics and hydrodynamical processes. The situation is even less clear when trying to account for dissipative hydrodynamical effects. This really represents a serious limitation to our understanding of the large-scale galaxy distribution, since the observational mapping of the universe mostly passes through the detection of luminous structures, i.e. of the regions where dissipation plays a fundamental role. A complete description of the attempts devoted to describing the hydrodynamical effects involved in galaxy formation is beyond the scope of this thesis. In the framework of the gravitational instability picture, any non-gravitational effect is expected to be relevant only at quite small scales, where the characteristic time-scale for gravitational collapse, $t_{\rm dyn} \sim (G\rho)^{-1/2}$, becomes comparable to the cooling time-scale $t_{\rm cool}$. The determination of $t_{\rm cool}$ is surely less reliable than that of $t_{\rm dyn}$, since it relies on the knowledge of cooling mechanisms, local chemical composition, etc. Nevertheless, it is reasonable to assume that at scales larger than that of a typical galaxy the dynamics is entirely determined by the non-dissipative gravitational interaction. However, the difficulty of analytically following the gravitational evolution when such equations are not linearisable forces one to resort to numerical methods. In this context, N-body simulations furnish a fundamental contribution towards understanding in more detail the nature of non-linear gravitational dynamics. In fact, N-body codes describe the evolution of non-linear gravitational clustering by following particle trajectories under the action of the gravitational force. Initial conditions (i.e, initial fluctuation and velocity fields) are fixed in a consistent way at a sufficiently early time, so that linear theory is a good approximation at all the relevant scales. Then, the final result of gravitational clustering is compared with the observational data, in order to assess the reliability of the initial condition model. It is however clear that, since small scale virialized structures probably have almost no memory of initial conditions, structures on larger scales (e.g. filaments or voids) are much more useful in giving constraints about the nature of the primordial fluctuations.

A basic parameter which measures the capability of N-body codes to faithfully represent gravitational clustering is the width of their dynamical range for mass and length resolution. Mass resolution is fixed by the total number of particles employed. Since a given mass is assigned to each particle, we should require at the linear stage that fluctuations on a mass scale below that of a particle were negligible. The dynamical range for length resolution is fixed by the ratio of the size of the simulation box to the softening scale for the computation of the gravitational force. Very detailed tests are always required to measure the resolution of numerical codes, in order to be sure about the reliability of the subsequent clustering representation. Because of the limits imposed by computational costs and computer memory, different strategies can be adopted in order to compromise between numerical resource and extension of the dynamical range. Accordingly, three main categories of N-body simulations can be devised, which essentially differ in their prescriptions for evaluating the gravitational force between particles.

- Direct integration of the force acting on each particle, due to the presence of all the other particles (Aarseth 1984). Within this approach, the force softening scale is usually very small and the particle trajectories are calculated with great precision. However, the price to be payed for this accuracy is the high computational cost, which goes like N^2 (N being the number of particles). Therefore, only a rather limited number of particles ($\lesssim 10^4$) is usually employed. Early N-body work such as studies of relatively small stellar systems were approached using a direct summation of the forces on each body due to every other body in the system (Aarseth 1984). This direct $\mathcal{O}(N^2)$ approach is impractical for large numbers of bodies, N, but has enjoyed a revival due to incredible throughput of special purpose hardware such as GRAPE (Hut & Makino 1999). The GRAPE hardware performs the mutual force calculation for sets of bodies entirely in hardware and remains competitive with other methods on more standard floating hardware up to $N \sim 100000$.
- A popular scheme for larger N is the Particle-Mesh (PM) method which has long been used in electrostatics and plasma physics. The adoption of PM was strongly related to the realization of the existence of the $\mathcal{O}(N \log N)$ Fast Fourier Transform (FFT) in the 1960's. The FFT is used to solve for the gravitational potential from the density distribution interpolated onto a regular mesh. In astrophysics submesh

resolution is often desired, in which case the force can be corrected on sub-mesh scales with local direct sums as in the Particle-Particle Particle-Mesh (P^3M) method. PM is popular in stellar disk dynamics, and P^3M has seen widespread adoption in cosmology, PM codes have similarities with multigrid and other iterative schemes. However, working in Fourier space is not only more efficient, but it also allows efficient force error control through optimisation of the Green's function and smoothing. Fourier methods are widely recognised as ideal for large, fairly homogeneous, periodic gravitating simulations. Multigrid has some advantages in parallel due to the local nature of the iterations. The Particle-Particle correction can get expensive when particles cluster in a few cells. Both multigrid and P^3M can adapt to address this via a hierarchy of sub-meshes. With this approach the serial slow down due to heavy clustering tends toward a fixed multiple of the unclustered run speed.

In applications such as galactic dynamics where high resolution in phase space is desirable and particle noise is problematic, the smoothed gravitational potentials provided by an expansion in modes is useful. PM does this with Fourier modes; however, a more elegant approach is the Self-Consistent Field method (SCF) (Weinberg 1999). Using a basis set closely matched to the evolving system dramatically reduces the number of modes to be modelled; however, the system must remain close to axi-symmetric and similar to the basis. SCF parallelises well and is also used to generate initial conditions such as stable individual galaxies that might be used for merger simulations.

- Combination of the two above methods, in order to improve the force resolution of the PM code. The resulting "particle-particle-particle mesh" (PM) code corrects the small scale force acting on each particle by summing over the contributions from neighbour particles (Efstathiou et al. 1985).

- The code employed in this work, PKDGRAV2 (Stadel 2001) uses tree algorithms which are inherently $\mathcal{O}(N \log N)$. This approach recognises that details of the remote mass distribution become less important for accurate gravity with increasing distance. Thus the remote mass distribution can be expanded in multipoles on the different size scales set by a treenode hierarchy. The appropriate scale to use is set by the opening angle subtended by the tree-node bounds relative to the point where the force is being calculated. The original Barnes-Hut (Barnes & Hut 1986) method employed oct-trees but this is not especially advantageous, and other trees also work well (Jernighan & Porter 1989). The tree approach can adapt to any topology, and thus the speed of the method is somewhat insensitive to the degree of clustering.

A particularly useful property of tree codes is the ability to efficiently calculate forces for a subset of the bodies. This is critical if there is a large range of time-scales in a simulation and multiple independent timesteps are employed. At the cost of force calculations no longer being synchronised among the particles substantial gains in time-to-solution may be realized. Multiple timesteps are particularly important for current astrophysical applications where the interest and thus resolution tends to be focused on small regions within large simulated environments such as individual galaxies, stars or planets. Dynamical times can become very short for small numbers of particles. $\mathrm{P}^3\mathrm{M}$ codes are faster for full force calculations but are difficult to adapt to calculate a subset of the forces.

The Fast Multipole Method (FMM) recognises that the applied force as well as the mass distribution may be expanded in multipoles. This leads to a force calculation step that is $\mathcal{O}(N)$ as each tree node interacts with a similar number of nodes independent of N and the number of nodes is proportional to the number of bodies. Building the tree is still $\mathcal{O}(N \log N)$ but this is a small cost for simulations up to $N \sim 10^7$ (Dehnen 2000). For the majority of astrophysical applications the allowable force accuracies make it much more efficient to use fixed order Cartesian expansions and an opening angle criterion similar to standard tree codes. This approach has the nice property of explicitly conserving momentum (as do PM and $\mathrm{P}^3\mathrm{M}$ codes).

For further technical details about N-body codes I refer to the standard textbook by Hockney & Eastwood (1981).

2 Does the Fornax dwarf spheroidal have a central cusp or core?[3]

2.1 Abstract

The dark matter dominated Fornax dwarf spheroidal has five globular clusters orbiting at ~ 1 kpc from its centre. In a cuspy CDM halo the globulars would sink to the centre from their current positions within a few Gyrs, presenting a puzzle as to why they survive undigested at the present epoch. We show that a solution to this timing problem is to adopt a cored dark matter halo. We use numerical simulations and analytic calculations to show that, under these conditions, the sinking time becomes many Hubble times; the globulars effectively stall at the dark matter core radius. We conclude that the Fornax dwarf spheroidal has a shallow inner density profile with a core radius constrained by the observed positions of its globular clusters. If the phase space density of the core is primordial then it implies a warm dark matter particle and gives an upper limit to its mass of ~ 0.5 keV, consistent with that required to significantly alleviate the substructure problem.

2.2 Introduction

The Fornax dwarf spheroidal is a dark matter dominated satellite orbiting the Milky Way. It has five globular clusters that are at a projected distance from the centre of 1.60, 1.05, 0.43, 0.24 and 1.43 kpc (Mackey & Gilmore 2003) as well as further substructure at a projected distance of 0.67 kpc (Coleman et al. 2005). These star clusters move within a dense background of dark matter and should therefore be affected by dynamical friction, causing them to lose energy and spiral to the centre of the galaxy. We will show later that, if Fornax has a cosmologically consistent density distribution of dark matter, the orbital decay timescale of these objects from their current positions is $\lesssim 5$ Gyr. This is much shorter than the age of the host galaxy, presenting us with the puzzle of why these five globulars have not merged together at the centre forming a single nucleus (Tremaine, Ostriker & Spitzer 1976; Tremaine 1976).

Several groups have studied the origin of nuclei in galaxies: e.g. Lotz et al. (2001) carried out Monte Carlo simulations, which show that some, but

---

[3] This chapter has been published as Goerdt et al. (2006).

not all, of the nuclei of dwarf elliptical galaxies could indeed have formed through coalescence of their globular clusters. Additionally they observed several dE galaxies and found out that within the inner few scale lengths, their sample appeared to be depleted of bright clusters. Oh and Lin (2000) used numerical simulations to show that in dwarf galaxies with relatively weak external tidal perturbations, dynamical friction can lead to significant orbital decay of globular clusters and the formation of compact nuclei within a Hubble timescale.

Oh, Lin and Richer (2000) gave two possible models for the observed spatial distribution of Fornax globulars. One possibility they proposed is that the dark matter consists of massive black holes which transfer energy to the globulars, preventing them from sinking to the centre of the galaxy. Another possibility they investigated was to postulate a strong tidal interaction between the Milky Way and Fornax which also could inject energy into their orbits and the central core of the dSph. This latter idea is probably ruled out due to the proper motion observations of Fornax (Dinescu et al. 2004) which suggest it is already at closest approach on an extended orbit which never takes it close to the Milky Way.

Here we investigate another possibility for the lack of a nucleus in Fornax, namely that the central dark matter distribution has a very shallow cusp or core which dramatically increases the dynamical friction sinking timescale (Hernandez & Gilmore 1998). This would be inconsistent with dark haloes that form within the CDM cosmology which have cusps steeper than -1 on all mass scales from $10^{-6}\mathrm{M}_{\odot} - 10^{15}\mathrm{M}_{\odot}$ (Dubinski & Carlberg 1991; Diemand, Moore & Stadel).

Controversial evidence for cored mass distributions in dwarf spiral galaxies has been debated for over a decade (Moore 1994). The inner structure of spheroidal galaxies is harder to determine, however Kleyna et al. (2003) claimed that the second peak in the stellar number density in the nearby Ursa Minor dwarf spheroidal (UMi dSph), is incompatible with cusped cold dark matter haloes. With their observations they show that this substructure has a cold kinematical signature and that its radial velocity with respect to its host galaxy is very small. Such a cold configuration could only survive intact if the stars orbited within a cored mass distribution where the orbital frequencies are all identical (harmonic potential) and phase mixing does not occur.

The stellar kinematical data for Fornax suggest that it is dark matter dominated with a mass to light ratio of order 20 within its optical extent. Due to the uncertainty on the orbital anisotropy, the mass distribution can only be weakly constrained - the data is consistent with either cusped or cored density distributions (Łokas 2002). However the normalisation (or mass within the central 1 kpc) is better constrained. In the inner ~1 kpc of a cored halo the mean density is approximately six times lower than in a cusped halo. Furthermore the velocity distribution function of the background particles is hotter than a cusped halo. These facts conspire to significantly increase the dynamical friction timescale in a cored mass distribution.

In this paper we construct cored and cuspy dark matter potentials and calculate orbital decay and sinking times using high resolution numerical simulations together with analytic calculations (Chandrasekhar 1943). The haloes are consistent with the kinematical data for Fornax. We follow circular and eccentric orbits of single and multiple globular clusters. Although many dynamical friction studies have been carried out before (White 1983; Hernquist & Weinberg 1989; Capuzzo-Dolcetta & Vicari 2005), we are not aware of any studies within constant density cores at the resolution used in this paper, although the recent study explored the effects of sinking objects on various cusp structures (Merritt et al. 2004). In section 2.2 we present the numerical methods we used, the analytical computation of the sinking times which are compared to our high resolution numerical simulations. In section 2.3 we discuss our results and draw our conclusions.

2.3 Results

We carry out a series of self consistent simulations to examine the orbital behaviour of massive particles moving within a dark matter or stellar background. We use the parallel multi-stepping N-body tree-code, pkdgrav2, developed by Joachim Stadel (Stadel 2001). We construct stable particle haloes using the techniques developed by Kazantzidis, Magorrian & Moore (2004). These models have density distributions that are described by the α, β, γ law (Hernquist 1990):

$$\rho(r) = \frac{\rho_0}{\left(\frac{r}{r_\mathrm{s}}\right)^\gamma \left[1 + \left(\frac{r}{r_\mathrm{s}}\right)^\alpha\right]^{\frac{\beta-\gamma}{\alpha}}} \tag{14}$$

For our simulations we used "NFW-like" haloes (Navarro, Frenk & White 1996; Moore et al. 1999b) with $\alpha = 0.5 - 1.5$, $\beta = 3.0$ and $\gamma = 0.5 - 1.5$, or cored haloes with $\alpha = 0.5 - 1.5$, $\beta = 3.0$ and $\gamma = 0.0$. In the former case we have $\rho_0 = 0.0058\,\mathrm{M_\odot/pc^3}$ and $r_\mathrm{s} = 2.4\,\mathrm{kpc}$. This cuspy halo has a virial mass of $2.0 \times 10^9\,\mathrm{M_\odot}$. The concentration parameter is 15 but our results would not change with a lower concentration, since in either case we are within the asymptotic cusp part of the density profile.

We use a three shell model (Zemp 2006); 10^5 particles for the innermost sphere with 100 pc radius, 10^5 particles for the shell between 100 and 500 pc and 10^5 particles for the rest of the halo. The softening lengths of the particles in these shells are 1, 10 and 100 pc respectively. The results were found not to be sensitive to these values. The particle masses are $58\,\mathrm{M_\odot}$, $569\,\mathrm{M_\odot}$ and $3.2\ \times 10^4\,\mathrm{M_\odot}$. These models are stable in isolation but allow us to achieve very high resolution at the halo centre where we wish to follow the dynamical friction.

For a small cored halo we have $\rho_0 = 0.10\,\mathrm{M_\odot/pc^3}$ and $r_\mathrm{s} = 0.91\,\mathrm{kpc}$ (n.b. the radius at which the slope of the density profile is shallower than -0.1 is approximately 200 pc which defines the constant density region in this model). This halo has a virial mass of $2.0 \times 10^9\,\mathrm{M_\odot}$ and the concentration parameter is 40. Again, we use a three shell model that has 10^5 particles for the innermost sphere with 300 pc radius, 10^5 particles for the shell between 0.3 and 1.1 kpc and 3×10^5 particles for the rest of the halo. The softening lengths of the particles in these shells are 3, 30 and 300 pc respectively. The particle masses are $89\,\mathrm{M_\odot}$, $1640\,\mathrm{M_\odot}$ and $7572\,\mathrm{M_\odot}$. For a big cored dark matter halo we have basically the same parameters as for the halo with the small core, except for the scale length $r_s = 2.2\,\mathrm{kpc}$ (here the constant density region is approximately 1 kpc), the virial mass $M_\mathrm{vir} = 3.0 \times 10^{10}\,\mathrm{M_\odot}$ and the particle masses, which are in this case $106\,\mathrm{M_\odot}$, $3625\,\mathrm{M_\odot}$ and $1.2 \times 10^5\,\mathrm{M_\odot}$. The density profiles of these three haloes are shown in figure 1.

The density profiles agree fairly well with the constraints made by observations of Fornax (Łokas 2002, Walker et al. 2006). We did actually perform the same simulations and treatment as described in the following with the very haloes proposed by Łokas (2002) with the same results. We also repeated several of our simulations with haloes modelled with ten times as many particles than described above. These high resolution runs show exactly the same features as the low resolution runs, but with less noise.

Where available, we will present the high resolution graphs in this paper. The globular clusters are modelled as single particles of mass $M_\mathrm{GC} = 2 \times 10^5\,\mathrm{M_\odot}$ with a softening of 10 pc. We do not expect our conclusions to change

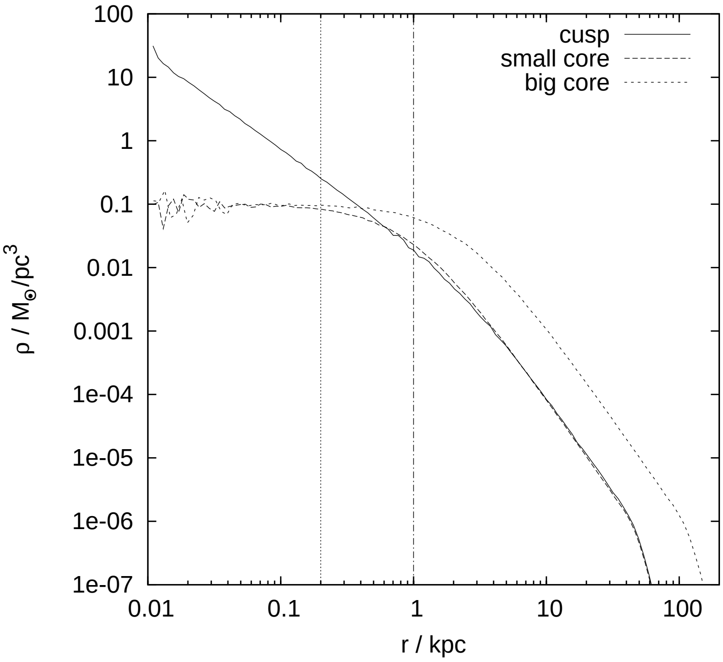

Figure 1: The initial radial density profiles for the three different haloes used in the simulations. The vertical lines indicate the size of the core of the cored haloes.

if we used a particle model for each globular since they are stable against tidal disruption within Fornax. We start the globulars outside the core, mostly on circular orbits and let them orbit, expecting them to spiral in to the centre of their respective host haloes due to dynamical friction. The distance from the centre of the host halo as a function of time, $r(t)$, can be computed using Chandrasekhar's dynamical friction formula (Binney & Tremaine 1987), which is given by:

$$\begin{aligned} F &= -\frac{4\pi\ln\Lambda(r)\rho(r)G^2M_{\rm GC}^2}{v_{\rm c}^2(r)}\left\{\mathrm{erf}\left[\frac{v_{\rm c}(r)}{\sqrt{2}\sigma(r)}\right]\right. \\ &- \left.\frac{2v_{\rm c}(r)}{\sqrt{2\pi}\sigma(r)}\exp\left[\frac{-v_{\rm c}^2(r)}{2\sigma^2(r)}\right]\right\}, \end{aligned} \tag{15}$$

which gives the force acting on the massive particle crossing the halo. The density profile $\rho(r)$ is given by our equation 14, and we assume that the velocity distribution is isotropic and Maxwellian at all radii. Of course this assumption does not hold, but is good enough for our purposes (Kazantzidis et al. 2004). We can then easily calculate the velocity dispersion using the Jeans equation:

$$\sigma^2(r) = \frac{G}{\rho(r)} \int_r^\infty \frac{M(r')\rho(r')}{r'^2} dr'. \tag{16}$$

We find similar sinking times for eccentric orbits, therefore for brevity we show only the circular orbits in this paper and leave the detailed parameter space study for a future paper which explores the technical aspects of dynamical friction in structures with different density profiles. Additionally we assume, that $M_{\rm GC} \gg m_{\rm par}$. This is a little problematic in the case of the cuspy and the big cored potential because the particles in the outermost shell have $m_{\rm par} = 3 \times 10^4\,{\rm M}_\odot$ and $m_{\rm par} = 1.2 \times 10^5\,{\rm M}_\odot$, respectively. However, these particles rarely penetrate the innermost 0.5 kpc of the halo. In equation 15, $\ln\Lambda(r)$, is the Coulomb logarithm:

$$\ln\Lambda(r) = \ln\frac{b_{\rm max}\sigma^2(r)}{GM_{\rm GC}}, \tag{17}$$

in this definition $b_{\rm max}$ is the largest impact parameter to be considered. This parameter is defined by one of the assumptions Chandrasekhar made while deriving the above dynamical friction formula: The intruder must be moving through a medium with constant density, therefore $b_{\rm max}$ is the greatest distance for which this is still valid. We keep $b_{\rm max}$ as a free parameter when fitting our analytic formulae to the simulations. We find for the cuspy haloes $b_{\rm max} = 0.25\,{\rm kpc}$ and for the cored ones $b_{\rm max} = 1.0\,{\rm kpc}$. In this equation $v_{\rm c}(r)$ is the circular velocity at radius r. The force exerted by dynamical friction on the perturber is tangential with respect to its movement and thus causes the cluster to lose angular momentum per unit mass at a rate

$$\begin{aligned} \frac{{\rm d}L}{{\rm d}t} &= \frac{Fr}{M_{\rm GC}} = -\frac{4\pi\ln\Lambda(r)\rho(r)G^2M_{\rm GC}r}{v_{\rm c}^2(r)}\left\{{\rm erf}\left[\frac{v_{\rm c}(r)}{\sqrt{2}\sigma(r)}\right]\right. \\ &- \left.\frac{2v_{\rm c}(r)}{\sqrt{2\pi}\sigma(r)}\exp\left[\frac{-v_{\rm c}^2(r)}{2\sigma^2(r)}\right]\right\}. \end{aligned} \tag{18}$$

Since the cluster continues to orbit at a speed $v_{\rm c}(r)$ as it spirals to the centre, its angular momentum per unit mass at radius r is at all times $L = rv_{\rm c}(r)$. Substituting the time derivative of this expression into equation 18 we obtain

$$\frac{{\rm d}r}{{\rm d}t} = -\frac{4\pi\ln\Lambda(r)\rho(r)G^2M_{\rm GC}r}{v_{\rm c}^2(r)\frac{{\rm d}[rv_{\rm c}(r)]}{{\rm d}r}}\left\{{\rm erf}\left[\frac{v_{\rm c}(r)}{\sqrt{2}\sigma(r)}\right]\right.$$

$$- \frac{2v_c(r)}{\sqrt{2\pi}\sigma(r)}\exp\left[\frac{-v_c^2(r)}{2\sigma^2(r)}\right]\Bigg\}. \tag{19}$$

Substituting values for the initial radii we obtain the analytical curves drawn in figure 2 plotted on top of the results from the numerical simulations.

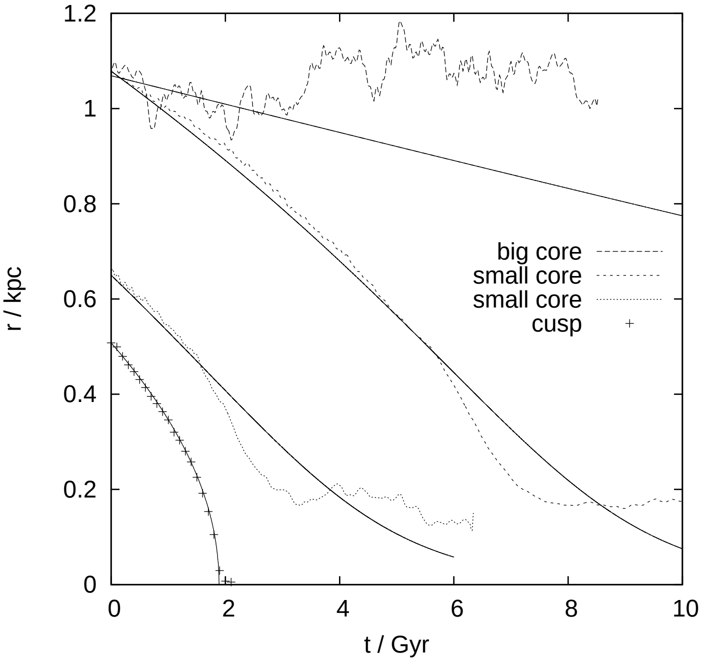

Figure 2: Radial distance of the single globular cluster from the centre of its host halo as a function of time. We start the calculations with the globular at different initial radii for clarity. Solid curves are the analytic estimates, dashed curves are from the numerical simulations.

For the cuspy potential the analytic calculation agrees very well with the numerical simulation. Haloes with a core give a poorer agreement. After an initial sinking rate that agrees well with the analytic expectation, the globulars sink faster as they approach twice the core radius, and then stop sinking at the core radius. The analytic formula predicts a continued, but slow infall to the centre. This resonance/scattering effect will be investigated in a more detailed paper (Read et al. 2006). We note, however, that it is not trivially due to the fact that the globular is of comparable mass to that enclosed by its orbit; the radius at which $M(r) = M_{GC}$ is $\sim$ three times smaller than the core radius (see Figure 4). The stalling results are apparent in both of the cored halo simulations (small core and big core). We conclude that the presence of a central density core leads to the infall of the clusters stopping at the core radius; the problem is in this sense scalable.

2.3.1 Particle noise and halo centring

It is difficult to define the centre of the constant density core. The potential has a negative minimum, but $\sqrt{N}$ noise perturbations can have deeper potentials than the core itself. Thus defining the centre using the most bound particle gives a large error in determining the centre. We found that a shrinking spheres method can work, so long as one takes the centre of mass of a sphere containing most of the core. If you continue to shrink the sphere based on a small number ($< 10^4$) particles, then this also picks out the largest Poisson fluctuation in the core. The centre defined using $\sim 10^5$ particles gives a robust estimate.

In our standard resolution simulations we use 10^5 particles in the high resolution region each of mass $89\,\mathrm{M}_\odot$. Simulating the entire halo at this resolution would require $\sim 4 \times 10^7$ particles. However, as discussed above, $\sqrt{N}$ noise can be substantial, even at this resolution. This may introduce spurious heating, preventing the globulars from sinking. We can investigate this by examining the orbit of the globular cluster. For a perfectly smooth spherical potential the orbit of the globular cluster would always remain in its initial orbital plane. Fluctuations from particle representation will cause deviations from this plane. Once the globular reaches the high density centre in the cases of the low resolution runs fluctuations in the orbital plane become very large (fluctuations in L_z/L $\sim$0.5%) - the relaxation time is very short and acts to counter dynamical friction. We therefore carried out simulations with ten times as many particles. At this resolution the fluctuations are greatly reduced (fluctuations in L_z/L $\sim$0.05%).

2.3.2 Multiple globular clusters

Finally we re-ran these simulations using five globulars to study the effect of having multiple sinking objects. Perhaps interactions between the globulars themselves may prevent them from sinking to the central cusp and merging. We distribute the globulars randomly, what position and plane of the orbit concerns, with distances to the centre between 0.2 and 0.8 kpc. The clusters are again placed on circular orbits around the centre of their host halo and are evolved with PKDGRAV2.

Interestingly, the clusters do not prevent one another from falling to the centre, but instead create an interesting prediction. Figure 3 shows the infall as a function of time for the five globulars in the cuspy dark matter halo. Notice that all of the clusters fall to the centre. However, clusters which start out at very similar radii arrive $\sim$ 1Gyr apart. At any given time, even for very similar initial conditions, the clusters occupy a range of radii. By contrast, for the case with a central dark matter core (see figure 4), although the globulars still arrive at different times due to interactions, they stall at the core radius; they do not sink to the centre even within 20 Gyrs[4]. Thus, if Fornax does have a central constant density core we should expect the clusters to stall at some minimum radius. No globular cluster could possibly get any closer to the centre of the halo than the core radius. The lower limit of the core size is constrained by the smallest observed projected cluster distances to be 0.24 kpc.

Finally, one can see in figure 5 that for the case where there is a cusp and the globular clusters do spiral in, they displace the dark matter from the centre. Dark matter particles move out of the nucleus. The density of the dark matter in the centre drops by more than an order of magnitude, an effect that does not happen in cored haloes. We note that several authors have recently studied this process in detail. For example El-Zant, Shlosman & Hoffman (2001) and Merritt et al. (2004) study the change in an initial cuspy density profile due to the frictional effects of sinking objects. This process allows initially cusped density profiles to be transformed into nearly harmonic cores as the globulars fall in. For the case of the five globulars in the Fornax halo, the maximum initial central density slope for which this can occur is approximately 0.5. Thus in order for these data to be consistent with a CDM halo, the central cusp must have been modified and flattened to a slope shallower than this value. Exotic scenarios which might achieve this include infall and subsequent blowout of massive gas clouds or star clusters (Read & Gilmore 2005).

---

[4] Recall that this stalling behaviour was also present in the run with a larger core size and so is not peculiar to the small core density profile.

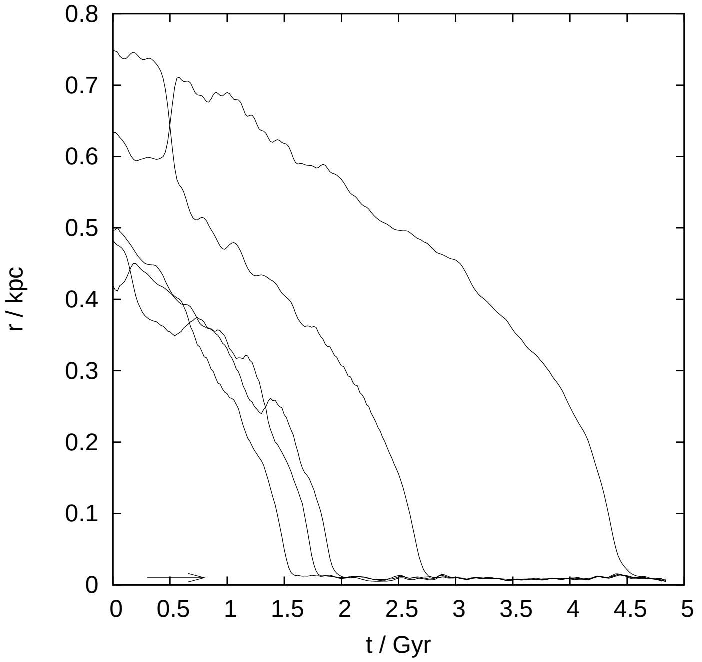

Figure 3: Radial distance of the five globular clusters from the centre of their host halo as function of time, as they orbit within a cusped density distribution. The arrow indicates the radius at which $M_{\mathrm{GC}} = M(r)$.

2.4 Conclusions

The Fornax dwarf spheroidal has five globular clusters orbiting at a projected radius of $\sim 1\,\mathrm{kpc}$ from its centre. Using a cuspy CDM potential with central slope steeper than 0.5 and normalised to match the inferred properties from the kinematical data, we find that these globulars would all sink to the halo centre within 5 Gyrs.

By contrast, we showed that if Fornax has a constant density central core then the dynamical friction time becomes arbitrarily long - the globulars stop sinking at the edge of the core, thus the present position of the *innermost* globular gives a lower limit of the core radius of the dark matter distribution. Since CDM uniquely predicts that all haloes are cusped, this suggests that the dark matter distribution within Fornax is not cold, but may be warm dark matter or some other candidate. Alternatively, the mass distribution has been modified through some exotic dynamical phenomenon such as rapid mass loss (Read & Gilmore 2005). If the phase space density of the core, measured

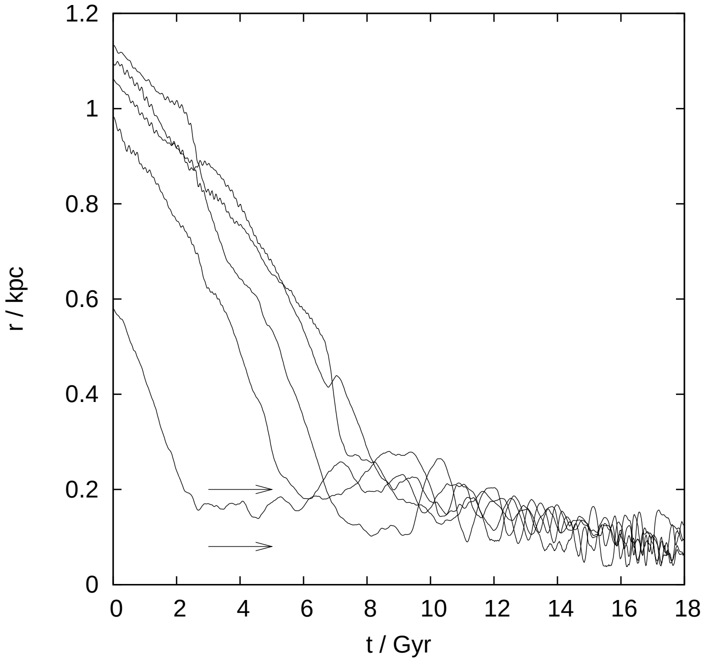

Figure 4: Radial distance of the five globular clusters from the centre of the host halo as function of time within the cored potential. The upper arrow indicates the size of the core and the lower arrow indicates the radius at which $M_{\mathrm{GC}} = M(r)$.

as $Q \sim 10^{-5} \mathrm{M}_{\odot}\,\mathrm{pc}^{-3} (\mathrm{km\ s}^{-1})^{-3}$ in our model, is primordial then it implies a warm dark matter particle of mass $\sim 0.5\,\mathrm{keV}$ (Hogan & Dalcanton 2000; Dalcanton & Hogan 2001). This is consistent with that required to largely solve the substructure problem (Moore et al. 1999a).

Although the dwarf spheroidals around the Milky Way do not contain prominent nuclei, about 30 percent of dwarf spheroidals (dE's) in clusters are nucleated. If these nuclei form by the merging of star clusters then we must conclude that these galaxies have cuspy mass distributions. This could be due to the fact that transformation to dE via galaxy harassment gives an exponential distribution of stars which usually dominate the central mass distribution. Therefore globulars could sink via friction against the stellar background. Most nucleated dE's are near the cluster centre where harassment is important which supports this idea.

Our numerical simulations show that the standard Chandrasekhar estimate of sinking timescales works well for cuspy cores but fails completely for

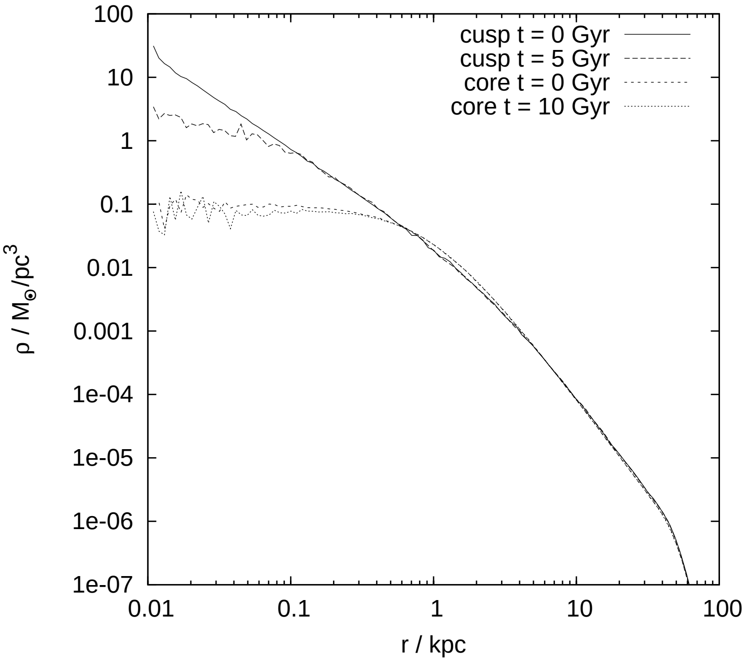

Figure 5: Radial density profile of the dark matter haloes. Only the dark matter is shown, the mass of the globular clusters is neglected. The initial conditions are compared with the final state of the system. An isolated halo, evolved for the same time, has exactly the same density profile as the initial conditions.

cored mass distributions. In addition we showed that over 10^6 particles are required within the core region to suppress heating from particle noise (Weinberg 1998). This is particularly important in a cored mass distribution where the potential minimum is quite shallow. The fact that cored mass distributions do not give rise to dynamical friction is an important result. We believe that this is due to orbit-resonant scattering. This will be the subject of a forthcoming paper (Read et al. 2006).

We have shown that a natural solution to the timing problems for Fornax's globular clusters is a central dark matter core. A prediction of this model is that the clusters have a well-defined minimum radius. Fornax is not alone in showing indirect evidence for such a core. The UMi dSph galaxy also has substructure which appears to have survived longer than is possible within a cuspy halo. Understanding the origin of these constant density cores could be one of the most exciting challenges facing astronomy in the next few years.

2.5 Acknowledgements

It is a pleasure to thank Tobias Huber for the fruitful discussions. Special thanks to Doug Potter for bringing to life the zBox2 supercomputer (http://www.zbox2.org) at the University of Zürich, on which all of the computations were performed.

3 Dynamical friction in constant density cores: a failure of the Chandrasekhar formula[5]

3.1 Abstract

Using analytic calculations and N-body simulations we show that in constant density (harmonic) cores, sinking satellites undergo an initial phase of very rapid (super-Chandrasekhar) dynamical friction, after which they experience no dynamical friction at all. For density profiles with a central power law profile, $\rho \propto r^{-\alpha}$, the infalling satellite heats the background and causes α to decrease. For $\alpha < 0.5$ initially, the satellite generates a small central constant density core and stalls as in the $\alpha = 0$ case. We discuss some astrophysical applications of our results to decaying satellite orbits, galactic bars and mergers of supermassive black hole binaries. In a companion paper we show that a central constant density core can provide a natural solution to the timing problem for Fornax's globular clusters.

3.2 Introduction

In a seminal paper, Chandrasekhar (1943) showed that a massive particle moving through an infinite, homogeneous and isotropic background of lighter particles experiences a force of dynamical friction given by:

$$M_\mathrm{c}\frac{\mathrm{d}v}{\mathrm{d}t} = -4\pi G^2 M_\mathrm{c}^2 \frac{v}{|v|^3} \ln\left(\frac{b_\mathrm{max}}{b_\mathrm{min}}\right) \int_0^{|v|} M(v')\mathrm{d}v' \tag{20}$$

where M_c and v are the mass and velocity of the in-falling particle, $M(v')\mathrm{d}v'$ is the mass density of background objects with speeds $v' \rightarrow v' + \mathrm{d}v'$, and b_max and b_min are the maximum and minimum impact parameters for the encounters[6]. From here on, we refer to the massive in-falling object as a 'Globular Cluster' (GC) and the background of lighter particles as simply 'particles'. However, we could equally refer to, for example, a bar moving in a background of stars and dark matter.

While equation 20 is only strictly valid for an infinite, homogeneous and

---

[5] This chapter has been published as Read et al. (2006).

[6] Note that $b_\mathrm{min} \rightarrow 0$ can be achieved (see e.g. White 1976; Binney & Tremaine 1987, p. 423), while $b_\mathrm{max} \rightarrow \infty$ cannot. This is because the derivation of equation 20 assumes an *infinite* background; b_max defines a scale on which the infinite background should be truncated. This is often, reasonably, take to be the radius at which the mean density falls by a factor of two or so.

isotropic background, it has been shown to work remarkably well for satellites orbiting in spherical galaxies with more general background distributions[7] (see e.g. White 1983; Bontekoe & van Albada 1987; Zaritsky & White 1988; Cora, Muzzio & Vergne 1997). Such successes make equation 20 of great practical value. But they beg the question: why has it been so successful, even when it is used so far beyond its expected regime of validity? Are we missing important physical insight into the dynamical friction process in spherical systems? Does Chandrasekhar fail to work well in some situations?

In order to address some of these issues, Tremaine & Weinberg (1984) (hereafter TW84) and Weinberg (1986) (hereafter W86) formulated a perturbative theory of dynamical friction which could be applied to spherical systems. Notice from equation 20, that most of the dynamical friction originates from particles with large impact parameters: it is the accumulation of many long range *small* interactions which leads to most of the dynamical friction; not the large angle scattering of close encounters. This is why perturbative methods can be used. TW84 and W86 consider a general, small, perturbation to a single background particle; and then sum over all particles in the system to obtain to total torque induced on the perturber.

In section 3.3, we will briefly summarise the essence of this perturbation method. For now, it is important to note the key assumptions in the method; and the key results. The two main assumptions are: (i) that the perturbation is small and (ii) that the frequency of the perturber changes with time, $\Omega_\mathrm{s} = \Omega_\mathrm{s}(t)$, *faster than the perturbation can grow non-linear.* For most potentials of interest this second assumption is satisfied. The perturber (the GC) will lose angular momentum to the background particles as a result of the dynamical friction, and Ω_s will then increase as the GC falls inwards.

Under the above assumptions, the perturbation method gives us new physical insight into the dynamical friction problem. To the order of the perturbation approximation, *all* of the torque comes from background particles which are close to resonance with the perturber. Non-resonant particles do not contribute to the friction at all. This is a key difference between the perturbation solution and that of equation (20). It suggests that if equation (20) is ever going to fail, it would do so for background particle distributions which are especially resonant.

In this paper, we describe such a super-resonant potential: that of the

---

[7] When corrected for velocity anisotropies, it has also been shown to work well in aspherical systems (see e.g. Binney 1977; Statler 1991; Peñarrubia, Just & Kroupa 2004).

constant density (harmonic) core. For this special potential, all particles and the perturber always move with constant angular frequency, Ω. In this case, perturbation methods can no longer be used. This is because $\Omega_{\mathrm{s}} = \mathrm{const}$; assumption (ii), above, is violated; and the perturbations, which are always driven at the same resonant frequency, can grow indefinitely[8].

To cope with this special case, we develop a non-perturbative analytic model using a 3D driven harmonic oscillator. This essentially generalises an earlier result derived by Kalnajs (1972). Using our analytic model and N-body simulations, we show that in constant density cores, equation (20) fails. Sinking satellites undergo an initial phase of very rapid (super-Chandrasekhar) dynamical friction, after which they experience little or no dynamical friction at all.

Weinberg & Katz (2007a,b) find similar stalling results for galactic bars (which may be thought of as two diametrically opposed satellites) inside constant density cores.

Constant density cores have recently become interesting in astrophysics. Observations of galaxies on all scales from dwarf spheroidals in the Local Group, up to giant spirals suggest that their central dark matter density has such a constant density core on the scale of $\sim 1\,\mathrm{kpc}$ (see e.g. Binney & Evans 2001; Borriello & Salucci 2001; de Blok et al. 2001; Kleyna et al. 2003); but see also Hayashi et al. (2004) and Rhee et al. (2004), for a discussion of the potential systematic errors in such observations. If cores are present at the centre of galaxies, their resonant properties can significantly affect the dynamics. Bars can be much longer lived[9], while in-falling satellites and GCs will stall at the core radius. In a companion paper, Goerdt et al. (2006), we investigate this last idea further (see also Hernandez & Gilmore 1998 and Sánchez-Salcedo, Reyes-Iturbide & Hernandez 2006). The Fornax dwarf spheroidal galaxy in the Local Group has 5 GCs at a range of projected radii. Application of Chandrasekhar dynamical friction suggests the clusters should rapidly fall to the centre of Fornax from their current positions; fine tuning is required to have them arrive at their present positions at the current epoch. In Goerdt et al. (2006) we show that a small core of radius greater than $0.24\,\mathrm{kpc}$ can solve this problem by causing some, or all, of Fornax's GC

---

[8] This is true for *any* perturbative scheme (e.g. Colpi, Mayer & Governato 1999).

[9] Debattista & Sellwood (1998) and Debattista & Sellwood (2000) show that low central dark matter densities lead to bars which remain fast. Here we discuss the extreme case of constant density cores, in which we show that bars would not slow down at all. This agrees well with earlier findings by Weinberg & Katz (2007a,b).

to stall.

This paper is organised as follows: in section 3.3 we briefly review the perturbative method for calculating dynamical friction and demonstrate that it fails for the special case of a constant density core. We show that insight can be gained from a non-perturbative approach by modelling the system as a driven harmonic oscillator. In section 3.4 we describe our semi-analytic and full N-body simulations. In section 3.5, we test our analytic model against these high resolution ($\sim 10^7$ particles) simulations of satellites sinking in harmonic cores. We demonstrate that such high resolution is required in order to reduce numerical precession of the GC orbit plane, but that near-converged results for the GC orbit can be obtained at lower resolution with O(10^6 particles). We discuss the importance of the initial GC orbit, mass, the underlying gravitational potential and the particle-particle interactions. Finally, in section 3.6 we briefly discuss the implications of these results and present our conclusions.

3.3 Analytic results

3.3.1 A brief review of the perturbation method

The essence of the TW84 perturbative approach to dynamical friction can be understood in the following way: consider a spherical potential, $\Phi(r)$, to which a small *non-axisymmetric* perturbation, Φ_s, is applied. The perturbation rotates with angular frequency Ω_s. In this case, the equations of motion of a test particle moving in a frame stationary with respect to the perturbation are given by:

$$\underline{\ddot{r}} + \underline{\nabla}[\Phi + \Phi_s] + 2\underline{\Omega}_s \times \underline{\dot{r}} + \underline{\Omega}_s \times (\underline{\Omega}_s \times \underline{r}) = 0 \tag{21}$$

where the third and fourth terms are the familiar Coriolis and Centrifugal inertial forces respectively.

The problem is symmetric about the plane containing the perturbation, so it makes sense to work in cylindrical coordinates: $\underline{r} = \underline{r}(R, \phi, z)$. Equation 21 then reduces to:

$$\ddot{R} - R\dot{\phi}^2 = -\frac{\partial[\Phi + \Phi_s]}{\partial R} + 2R\dot{\phi}\Omega_s + \Omega_s^2 R \tag{22}$$

$$R\ddot{\phi} + 2\dot{R}\dot{\phi} = -\frac{1}{R}\frac{\partial \Phi_s}{\partial \phi} - 2\dot{R}\Omega_s \tag{23}$$

and equation 23 can be rearranged to give:

$$\frac{d}{dt}\left(R^2\dot{\phi}\right) = \dot{J}_z = -\frac{\partial \Phi_s}{\partial \phi} - 2R\dot{R}\Omega_s \tag{24}$$

where J_z is the z-component of the specific angular momentum of the test particle and we have introduced the notation $\Omega_s = |\underline{\Omega}_s|$; and similarly for other vectors.

In order to solve equation 24, we must now specify the perturbation, $\Phi_s(R, \phi)$, and the angular motion of the test particle, $\phi(t)$. While it is not necessary in general, it also greatly simplifies the analysis to assume that $\dot{R} = 0$, which we do from here on. With this assumption, we can still illustrate usefully the key points of the perturbation method.

We consider the perturbation: $\Phi_s = Ae^{im\phi}$. This is instructive since it is then one component of a more general Fourier series sum. We can find $\phi(t)$ if we assume that the perturbation is small. The usual trick is to suppose that over short times the particle trajectory is the same as in the unperturbed case. For the *unperturbed* case, $\Phi_s, \Omega_s \rightarrow 0$ and equation 24 gives: $\phi_{in} = \Omega_* t +$const; where the subscript *in* reminds us that this is now with respect to an inertial frame. Transforming ϕ_{in} to the non-inertial frame rotating with Ω_s, gives: $\phi = (\Omega_* - \Omega_s)t + \mathrm{const}$.

Equation 24 may now be integrated to give:

$$J_z = -\mathrm{Re}\left\{\frac{A\exp[im(\Omega_* - \Omega_s)t]}{(\Omega_* - \Omega_s)}\right\} - R^2\Omega_s \tag{25}$$

It is clear from equation 25 that J_z just oscillates with no time averaged change[10](i.e. no dynamical friction) unless $\Omega_* = \Omega_s$. At this *resonant* frequency the test particle appears to have a pathological specific angular momentum. In practise this just means that the approximation that the perturbation is small fails.

TW84 show that if $\Omega_s = \Omega_s(t)$, then this problem can be solved. Provided Ω_s changes faster than the time taken for the perturbation to grow into the non-linear regime, then we can sum over all of the resonant interactions from the background particles and calculate the resulting torque on the perturber[11]. There are two regimes of interest: fast and slow passages through resonance.

---

[10] Recall that we have assumed that $R = \mathrm{const}$.

[11] Note that there is now an extra term which should also be included in equation 21: $\dot{\underline{\Omega}} \times \underline{r}$; we assume that this is small.

The fast passage through resonance recovers the LBK torque formula (Lynden-Bell & Kalnajs 1972). This is the perturbation theory equivalent of equation 20: it describes the dynamical friction. For slow passages through resonance, TW84 find quite different behaviour. The torque is stronger than in the LBK case, reversible, and can lead to the capture (gravitational binding) of background particles by the perturber. These differences led TW84 to refer to this as *dynamical feedback*, rather than friction. We return to this effect in section 3.3.2.

In this paper we discuss a special potential of interest generated by a constant density core. For this special case, the divergence in equation 24 persists because Ω_s stays fixed. The potential for a constant density core is the harmonic potential given by:

$$\Phi = \frac{\Omega^2}{2} r^2 + \text{const} \tag{26}$$

where Ω is the angular frequency of test particles (including the GC; $\Omega_s = \Omega$) in the harmonic core.

The equation of motion for the GC perturber moving in the harmonic potential is given by:

$$\ddot{\underline{r}}_c + \underline{\nabla}\Phi = 0 = \ddot{\underline{r}}_c + \Omega^2 \underline{r}_c \tag{27}$$

Which may be trivially solved to give the general solution:

$$\underline{r}_c = [X \sin(\Omega t + \phi_x), Y \sin(\Omega t + \phi_y)] \tag{28}$$

From equation 28 we can see that orbits in harmonic potentials are of fixed relative phase angle, closed and of constant angular frequency, Ω. This means that provided the potential remains harmonic, any perturbation to the GC orbit - including dynamical friction and loss of angular momentum - will not change Ω or $\Omega_s = \Omega$. In other words, $\Omega_s \neq \Omega_s(t)$ and we can no longer apply perturbation theory methods.

M. Weinberg (private communication) has made the valid point that the perturber itself, and the non-spherically symmetric background distribution it induces, cause deviations from true harmony. It may be possible to use a perturbative approach in this, more realistic, case.

3.3.2 A non-perturbative approach

Perturbation methods fail for the harmonic core. However, all is not lost analytically. We can still gain much insight by writing down the equations of motion for the GC and a tracer background population, and searching for stable solutions. As we shall show next, for the special case of a harmonic potential plus point mass perturber (the GC), solutions exist where the background particles rotate about the GC on stable epicycles. Stable orbits mean no time averaged angular momentum transfer and, therefore, no dynamical friction.

Such a model allows us to make firm qualitative (if not quantitative) statements about what will happen when a GC is introduced to an isotropic constant density core. Initially, particles will be in equilibrium in the constant density core. As the GC approaches the core, the system will need to rearrange itself and reach a new equilibrium state. The non-linear interplay between the GC and the background distribution during this rearrangement leads to a period of enhanced, super-resonant friction. After ~ 1 dynamical time, the distribution function of the background will now be the correct one for the GC plus harmonic core, and dynamical friction will cease. Note that this rearrangement may also be understood in terms of the TW84 *dynamical feedback* discussed in section 3.3.1.

Our model does not include the back-reaction of the test particles on the GC, nor does it include the interaction between the background particles themselves. However, we find a good agreement between our analytic model and full N-body simulations, which include the above effects, in section 3.4. This suggests that our simple model does capture the essential physics of the problem.

The analytic set-up is shown in Figure 6. The in-falling GC at a radius, $\underline{r}_c$ is marked by the black circle and is a phase angle, α, away from a given background particle at a radius, $\underline{r}_p$. We assume that the underlying potential is always harmonic (given by equation 26); the GC is well approximated by a point mass; and the background potential is nailed down (this is reasonable provided that $M_c \ll M_{en}$ where M_{en} is the mass enclosed by the GC). Under these assumptions, the equation of motion for a single background, massless *tracer*, particle is given by:

$$\ddot{\underline{r}}_p + \Omega^2 \underline{r}_p = \underline{F} = \frac{GM_c(\underline{r}_c - \underline{r}_p)}{|\underline{r}_c - \underline{r}_p|^3} \tag{29}$$

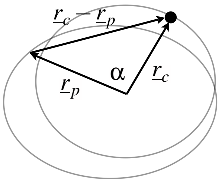

Figure 6: A schematic diagram of the analytic set-up. The in-falling GC is marked by the solid black circle. The GC and particle orbits are marked by the grey ellipses. See text for further details.

where $\underline{F}$ is the specific force on the particle from the GC, G is the gravitational constant and M_c is the mass of the GC.

We now search for stable solutions to equation 29 where the GC orbit is unchanged by the background. Combining equations 27 and 29 gives:

$$\ddot{\underline{r}}_d + \left(\Omega^2 - \frac{GM_c}{|\underline{r}_d|^3}\right)\underline{r}_d = 0 \tag{30}$$

where $\underline{r}_d = \underline{r}_c - \underline{r}_p$.

From equation 30, it is clear that stable solutions exist where the background particles move on circular epicycles about the GC with $|\underline{r}_d| = \text{const}$. However, more general solutions may be found by noting that equation 30 is spherically symmetric. Moving to spherical polar coordinates: $\underline{r}_d = (r, \theta, \phi)$, it is straightforward to show that the θ and ϕ specific angular momenta are conserved: $J_\theta = r^2\dot{\theta} = \text{const}; J_\phi = \text{const}$. This is to be expected given the symmetry of the problem. Equation 30 then reduces to:

$$\ddot{r} + \frac{d\Phi_{\text{eff}}}{dr} = 0 \tag{31}$$

$$\Phi_{\text{eff}} = \frac{\Omega^2 r^2}{2} + \frac{GM_c}{r} + \frac{J_\theta^2}{2r^2} \tag{32}$$

where Φ_{eff} is the effective potential.

From equation 31, we can see that in general, the background particles move on epicycles about the GC. These epicycles will not be closed, but they are quasi-periodic. Provided the distribution function of these background particles is the correct equilibrium distribution for the GC plus the harmonic core, there will be no time averaged momentum exchange between the GC and the background, and therefore no dynamical friction. The epicyclic orbits are stable, as can be readily seen by considering $\frac{\partial^2\Phi_{\mathrm{eff}}}{\partial r^2}$.

The existence of stable analytic solutions is a very special property of the harmonic potential; they exist because $\Omega = \mathrm{const}$. In more general potentials, $\Omega = \Omega(\underline{r}_p)$ and the symmetry of equation 30 is broken. This is an important issue. One can imagine a thought experiment where a GC is held (artificially) on a fixed orbit in a general spherical potential. After a few dynamical times, it will have scattered the resonant background particles, reducing the torque from the background to zero. It is important to stress that this is quite different to the situation we have described in this paper. In the above thought experiment, a tiny perturbation to the GC orbit (which must in practise occur as a result of its self-consistent interaction with the background) will expose the GC to an entirely new set of resonant background particles: dynamical friction will not cease. In our example, however, *any* perturbation to the GC orbit will not alter its orbital frequency at all: the resonances will remain unchanged. This is why our assumption, above, that the GC orbit is fixed is not an important one for the harmonic potential, but would be for any other potential. We test that this is indeed the case by relaxing the assumption of a fixed GC orbit in section 3.4.

We can use the above solution to calculate the final distribution of background particles at equilibrium when the dynamical friction ceases. The key point is that the final distribution will move on stable epicycles about the GC. Firstly, this means that we can expect a density enhancement around the GC, and a depletion of particles away from the GC. Secondly, we can expect a large depletion in counter-rotating particles with respect to the centre of the potential. All particles, whether they move on co- or counter-rotating epicycles have guiding centres which co-rotate with the GC. For $|\underline{r}_d| < |\underline{r}_c|$, the radius of the epicyclic orbit is smaller than that of the GC: none of these particles can counter-rotate with respect to the centre of the potential. For $|\underline{r}_d| > |\underline{r}_c|$, particles on counter-rotating epicycles can appear to counter-rotate with respect to the centre of the potential. These will be a small fraction of the total particles which remain. We test these qualitative expectations, using simulations, in section 3.4.

A final point, which will become important later on, is that the orbit plane of the GC matters. Equation 30 is spherically symmetric about the

GC and hides this fact. If the GC orbit changes (and noise within the full N-body simulations can cause this to happen) then the angular frequency vector of the GC, $\underline{\Omega}$, will change: the background distribution will no longer be in equilibrium with the GC. The system will have to move once again into equilibrium and this rearrangement will lead to some associated dynamical friction on the GC.

3.3.3 The Kalnajs solution

Our analytic method is a more general case of an earlier result found by Kalnajs (1972). Kalnajs studied dynamical friction in a uniformly rotating sheet in which all particles initially move on circular orbits. This is an equivalent problem to a GC moving on a circular orbit within a harmonic potential. He showed, using results from plasma physics, that in this case dynamical friction will vanish. Here we generalise this result to a GC moving on a general orbit within a harmonic potential. In our solution, the background perturbation need not lie in the plane of the GC orbit.

3.4 Simulations

In this section we compare semi-analytic and full N-body simulations to the analytic formulae derived in section 3.3. The simulations are labelled as in Table 2 and described in detail in the sub-sections below.

The analytic arguments given in section 3.3 suggest that once a GC is introduced to a constant density background, the system will move towards a stable equilibrium where the background particles move on epicycles about the GC. However, this simple analytic argument cannot say anything about interactions between the GC and the background particles prior to such an equilibrium being achieved; or of interactions between the background particles themselves. In this section we investigate this approach to equilibrium using numerical simulations. We use two types of simulation. The semi-analytic (SA) run solves equation 29 numerically. We still assume that the GC orbit is fixed, however we can study how the system moves from one equilibrium state (without the GC) to its final equilibrium with the GC. The full N-body (NB) run includes the interaction between the particles and the GC self-consistently. The GC is now free to respond to the background particles. This allows us to study the full effect of dynamical friction on the GC as the

Simulation	*Description*	*GC orbit*	
SA{c,e}	Semi-analytic	Fixed, {(c)irc., (e)llip.}	
NB{c,e}	N-body	Live	
NB3{c,e}	N-body	Live	
Simulation	*Resolution*	*Potential*	$M_{\rm c}$
SA{c,e}	10^5 tracer	Fixed, harmonic	$2 \times 10^5 {\rm M}_\odot$
NB{c,e}	10^7	Live, $\alpha, \beta, \gamma = [1.5, 3, 0]$	$2 \times 10^5 {\rm M}_\odot$
NB3{c,e}	10^7 3-shell	Live, $\alpha, \beta, \gamma = [1.5, 3, 0^*]$	$2 \times 10^5 {\rm M}_\odot^*$

Table 2: Simulation labels and parameters. From left to right the columns show the simulation label; a brief description (for more details see the relevant subsection in section 3.4); the initial GC orbit (see section 3.4.3); the background gravitational potential; the simulation resolution; and the mass of the GC ($M_{\rm c}$). Parameters marked with a $*$ are allowed to vary. In section 3.5.3, we measure the effect of changing γ on the NB3 simulation; in section 3.5.2, we measure the effect of changing $M_{\rm c}$.

system moves towards its new equilibrium state. We compare results for a GC initially on a circular orbit and an elliptical orbit.

3.4.1 The semi-analytic model: SA

In the semi-analytic model (SA) we solved equation 29 with the GC orbit held fixed (the GC initial conditions are described in section 3.4.3). The underlying potential was pure harmonic and static. We used $\Omega^2 = 4/3\pi G\rho_0$ and $\rho_0 = 9.93 \times 10^7\,{\rm M}_\odot$ kpc^{-3}. We used an isotropic, constant density, 3D, initial distribution of massless tracer particles. The equations of motion were solved using an RK4 numerical integrator (Press et al. 1992), with fixed timesteps of 1.5×10^{-5} Gyrs. This was found to conserve energy to machine accuracy over the whole simulation time in the limit $M_{\rm c} \rightarrow 0$. We ran the simulations for 1 Gyr, which is ~ 10 dynamical times for the GC at the core radius. This is the appropriate length of time for comparison with the full N-body run (see section 3.4.2). We tried runs with force softening for the GC and without. There was no significant change in the results for a force softening of 10 pc. The GC orbit was chosen to match the final stalled orbit observed in the N-body models. We ensured that the final position of the GC was identical in both models.

3.4.2 The N-body model: NB

In the full N-body (NB) model, we used the parallel multi-stepping N-body tree-code, Pkdgrav2, developed by Stadel (2001). The potential was calculated self-consistently from the live particle distribution. The GC was allowed to freely respond to the background particles.

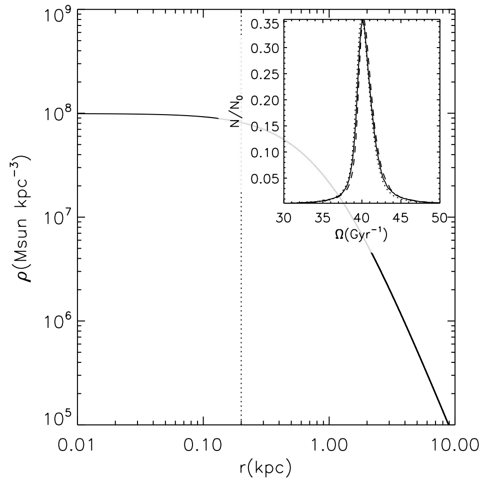

Figure 7: The density distribution for the background particles used in the numerical simulations, see equation 33. The dotted line marks the asymptotic central core where the density is constant and the potential harmonic. Inset in the plot is the distribution of orbital frequencies in the core region, plotted as $|\ddot{r}_\mathrm{i}/r_\mathrm{i}|$; $r_\mathrm{i} = x_\mathrm{p}, y_\mathrm{p}, z_\mathrm{p}$ (solid, dotted and dashed lines). These are equal and strongly peaked around a single value, showing that the core is indeed harmonic.

We constructed stable particle halos using the techniques developed by Kazantzidis, Magorrian & Moore (2004). The particles are drawn selfconsistently from a numerically calculated distribution function. We used a density distribution that is described by the α, β, γ law (Hernquist 1990; Saha 1992; Dehnen 1993; Zhao 1996):

$$\rho(r) = \frac{\rho_0}{\left(\frac{r}{r_\mathrm{s}}\right)^\gamma \left[1 + \left(\frac{r}{r_\mathrm{s}}\right)^\alpha\right]^{\frac{\beta-\gamma}{\alpha}}} \tag{33}$$

where we used $\rho_0 = 9.93 \times 10^7\,\mathrm{M_\odot\,kpc^{-3}}$, $r_\mathrm{s} = 0.91\,\mathrm{kpc}$, $\alpha = 1.5$, $\beta = 3.0$ and $\gamma = 0.0$. Note that r_s is the *scale* radius, not the core radius. The radius at which the log-slope of the density profile is shallower than -0.1 is $r_\mathrm{core} \sim 200\,\mathrm{pc}$, which defines the constant density region in this model. This halo has a virial mass of $2.0 \times 10^9\,\mathrm{M_\odot}$ and the concentration parameter is 40. A plot of the density profile is given in Figure 7, where r_core is marked by the vertical dotted line. Inset in the plot is the distribution of orbital frequencies in the core region, plotted as $|\ddot{r}_\mathrm{i}/r_\mathrm{i}|$; $r_\mathrm{i} = x_\mathrm{p}, y_\mathrm{p}, z_\mathrm{p}$ (solid, dotted and dashed lines). These are equal and strongly peaked around a single value, showing that the core is indeed harmonic (c.f. equation 26).

The NB run, with 10^7 particles, corresponds to just 10^3 particles within 300 pc. To achieve higher resolution, in the NB3 model we also used a novel 3-shell approach (Zemp 2006). We briefly summarise this approach here, but defer the details and tests to Zemp (2006). The 3-shell model breaks up the mass distribution into three concentric spheres. The particles in each sphere are reduced in mass and increased in number so that central regions are of higher resolution. Such a model is very useful for the current study where we would like many particles to accurately sample the central harmonic core, but are not interested in the outer density profile which may then be less accurately sampled. Massive particles from the outer sphere can and do enter the central core in this model, but they are given proportionately higher force softening to prevent them from causing spurious hard scattering. The model produces stable density profiles over $> 20\,\mathrm{Gyrs}$, very high central resolution, and no unwanted two body effects. More detailed tests are given in Zemp (2006), but for the present study we also explicitly verified that the single component model (NB) gives comparable two-body noise (see appendix 3.8).

We used a three shell model that has 10^6 particles for the innermost sphere with 300 pc radius, 10^6 particles for the shell between 0.3 and 1.1 kpc and 4×10^6 particles for the rest of the halo. This gives us $\mathcal{O}(10^6)$ particles within the core region. To achieve a similar number of particles within the central 300 pc without the 3-shell model would require 4×10^8 particles in total. This is not yet technically feasible. Yet, as we show in section 3.4.4 and appendix 3.8, such high resolution is required to avoid spurious precession of the GC orbit plane. The advantage of the 3-shell model, given such limitations, is clear. The softening lengths of the particles in these shells were 3, 30 and 300 pc respectively. The particle masses were $8.9\,\mathrm{M_\odot}$, $164.0\,\mathrm{M_\odot}$ and $757.2\ \mathrm{M_\odot}$.

Even the most massive particles were 100 times less massive than the GC. We experimented with varying the shell force softening and radii and found our results to be insensitive to these values.

3.4.3 The GC orbit

We used a GC mass of $M_\mathrm{c} = 2 \times 10^5\,\mathrm{M}_\odot$ with a force softening of 10 pc. This gives $M_\mathrm{c}/M_\mathrm{en} = 0.06$, where M_en is the total mass of background particles inside r_core. For the N-body simulations, the GC was placed initially at a radius of 1.069 kpc on a circular (NB3c) and elliptical (NB3e; $v_\mathrm{i} = 0.4 v_\mathrm{circ}$) orbit. In both cases the GC orbited in the $x_\mathrm{p}, y_\mathrm{p}$ plane. For the SA simulations, the GC orbit was chosen to match that of the GC in the N-body models after it hit the constant density core and stalled. Its orbital phase was chosen such that at the end of the SA simulation (after 1 Gyr) the GC would be in the same place as in the N-body simulations.

3.4.4 Particle noise, resolution and convergence

We had surprising difficulty in obtaining enough resolution in the N-body simulations for our results to be believable. The problem centred around the precession of the GC orbit plane. For a spherical potential (such as that studied here) all orbits, including that of the GC, should be planar. However, in our initial lower resolution runs, with a resolution of 10^5 particles within 300 pc, we found that the GC orbit plane would precess, sometimes by as much as 20^o over 10 Gyrs. Since we are trying to model an effect that relies critically on the orientation of the GC orbit plane, it is essential that the plane remains stable.

In appendix 3.8, we use a simple analytic model of a 2D random walk to prove that this precession is a result of two-body noise in the simulations. Reducing such noise drove us to use the three shell model discussed above. We show in appendix 3.8, that the noise is not some special property of the three shell model, but is present in all N-body simulations. We found that some initial GC orientations showed more precession than others, for the same resolution. This is to be expected from a random walk driven by two-body noise. The effect of such precession was found to be quite small. However, it does lead to a spurious (and very slow, sub-Chandrasekhar) decay of the GC orbit once it reaches the core. We present the results here from simulations which showed the minimal GC plane precession. However, our main results are not sensitive to such selection. Nor are our results sensitive to the use of the three shell model.

3.5 Results

3.5.1 The stalling of dynamical friction in the core

Figure 8 (straight solid line) shows the decay of the radius of the GC as a function of time for the NB3c and NB3e simulations (see Table 2). Overlaid is the prediction from the Chandrasekhar formula given in equation 20. For this we used a *constant* $\ln \Lambda = 5$, which is the value we use throughout this paper. If we equate $b_{\rm min}$ with the GC force softening, $b_{\rm min} = 10$ pc, this gives $b_{\rm max} \simeq 1.5\,$kpc, which is of order the 'size' of our system. This is consistent with values found in other numerical studies of dynamical friction on point mass particles (see e.g. Spinnato, Fellhauer & Portegies Zwart 2003).

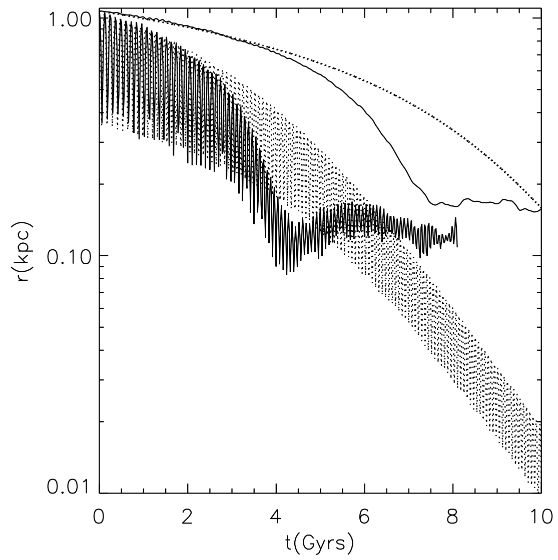

Figure 8: The decay of the radius of the GC as a function of time for a GC on a circular (straight solid line) and elliptical (oscillating solid line) orbit. Overlaid (dotted lines) are the predictions from the Chandrasekhar formula given in equation 20, using $\ln \Lambda = 5$. Notice that for the first few Gyrs the agreement with equation 20 is excellent. As the cluster nears the constant density core ($r_{\rm core} \sim 200\,$pc), it enters a phase of super-Chandrasekhar dynamical friction, after which dynamical friction practically ceases.

As the cluster nears the constant density core ($r_{\rm core} \sim 200\,{\rm pc}$), it enters a phase of super-Chandrasekhar dynamical friction, after which dynamical friction practically ceases. This occurs irrespective of the initial GC orbit. This is in excellent qualitative agreement with analytic expectations from section 3.3.

Figure 9 shows the distribution of particles in a slice about the orbit plane of the GC. The slice is defined such that $|\underline{J}_{\rm p} \cdot \underline{J}_{\rm c}| < |\underline{J}_{\rm p}||\underline{J}_{\rm c}|\cos(\theta)$, with $\theta = 10^{\rm o}$, where $\underline{J}_{\rm p,c}$ is the specific angular momentum of the particle and GC respectively. The left panel shows density contours for the particle distribution (which was initially constant-density) in the $x_{\rm p}, y_{\rm p}$ plane. The right panel shows velocity histograms for the v_ϕ component of the velocity; where v_ϕ is the velocity about the $z_{\rm p}$-axis. We do not show the $v_{\rm r}$ and v_θ components of the velocity, since they are not altered from the initial conditions and remain approximately Gaussian (r, θ and ϕ are the usual spherical polar coordinates). In the top panels, the solid lines show the slice just before the GC hits the core in the NB3c simulation (at time $t = 5\,{\rm Gyrs}$); the dotted contours show the SAc simulation at $t = 0$. The middle panels show similar results for the NB3c and SAc simulations at times $t = 8\,{\rm Gyrs}$ and $t = 1\,{\rm Gyrs}$, respectively. The bottom panels show the NB3e and SAe simulations at times $t = 4\,{\rm Gyrs}$ and $t = 1\,{\rm Gyrs}$, respectively. We analyse within this slice to highlight the changes in density caused by the GC. Outside of the slice, background particles still move on epicycles about the GC, but their projected positions onto the $x_{\rm p}, y_{\rm p}$ plane make it difficult to see the density enhancement about the GC.

Notice that the velocity histograms for v_ϕ (right panel, top) are double-peaked. This is because we have taken a thin slice in the orbit-plane of the cluster. The only particles that have $v_\phi = 0$ in this plane are those on pure radial orbits, which is a very small number of particles in the isotropic initial conditions.

In the top panels of Figure 9, the particles are close to their initial configuration. There has been some depletion in density at the centre and the on-set of some substructure, but the velocity histograms show that the velocity distribution of the background particles is still isotropic.

In Fig. 9 you see the distribution of particles in the $x_{\rm p}, y_{\rm p}$ plane for the N-body (solid lines) and semi-analytic (dotted lines) simulations. The left panels show density contours for the particle distribution (that was initially constant-density) in the $x_{\rm p}, y_{\rm p}$ plane. The right panels show velocity histograms for the

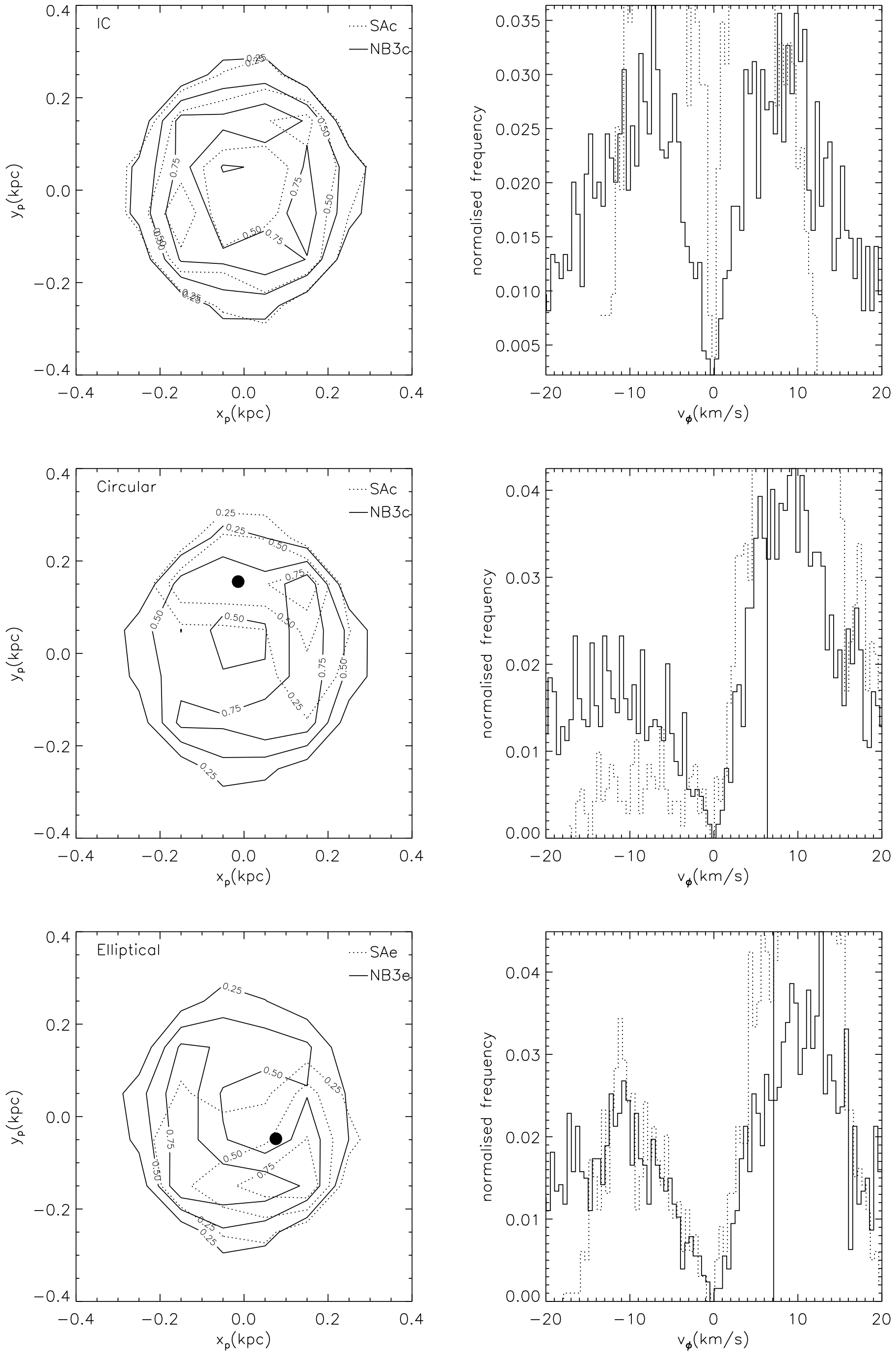

Figure 9: The distribution of particles in the x_p, y_p plane for the N-body (solid lines) and semi-analytic (dotted lines) simulations. The left panels show density contours and the right panels show velocity histograms for the v_ϕ component of the velocity.

v_ϕ component of the velocity; where v_ϕ is the velocity about the z_p-axis. The solid vertical line marks the GC velocity about the z_p-axis. The top two panels show the GC circular orbit simulations just before the GC experiences super-Chandrasekhar dynamical friction. This corresponds to $t = 0$ Gyrs for the SAc simulation, and $t = 5$ Gyrs for NB3c. Notice that, for the NB3c simulation (solid lines), the background particles are nearly unchanged from their initial distribution. The middle two panels show the GC on a circular orbit after the super-Chandrasekhar friction has finished and the GC has settled into a steady-state in the harmonic core. This corresponds to $t = 1$ Gyrs for the SAc simulation, and $t = 8$ Gyrs for NB3c. The bottom two panels show the GC on an elliptical orbit ($v_\mathrm{i} = 0.4v_\mathrm{circ}$) after it has reached the harmonic core. This corresponds to $t = 1$ Gyrs for the SAe simulation, and $t = 4$ Gyrs for NB3e. In all cases the final position of the GC in the SAc,e and NB3c,e simulations is identical and marked by the solid circle. Note that there is no GC marked in the top panels since, in the NB3c simulation, the GC lies outside of the plot area at this time.

The middle and bottom panels in Figure 9 show the distribution of particles in the slice after the super-Chandrasekhar friction has ended, and the GC has settled into equilibrium in the core. Notice the good agreement with the semi-analytic (SAc,e) simulations for both the density and velocity distribution in the slice, irrespective of the initial GC orbit. As expected from the arguments given in section 3.3, the number of counter-rotating particles has been significantly depleted.

The density distribution in the slice is peaked just behind the cluster; it has a tail which is longer for the full N-body run. This is likely due to particle-particle scattering which prevents high density regions from forming. Such a tail should lead to some dynamical friction on the GC from the background. We estimated the strength of this effect for the SAc model. To do this, we summed the force from all of the background particles on the GC, assuming that their total mass was M_en. What really matters is the *time averaged* force on the GC. This must be small, since little or no dynamical friction is observed after the GC reaches the core. However, even the total force at an instant is always smaller than the dynamical friction force, computed from equation 20.

Notice from equation 31, that we could construct *any* final density distribution using an appropriate combination of epicyclic orbits about the GC. In practise, however, the final density distribution is set by the initial configuration of background particles within the core. The transformation of this initial distribution by the arrival of the GC, must be determined numerically. The SA model is essential in this respect.

The keen observer will notice that the enhanced friction appears to set in rather near the region where the resolution in the 3-shell model increases (recall that the high resolution inner shell starts at 300 pc). This is almost certainly a coincidence. We performed two tests to check this. Firstly, an explicit test by starting a GC sinking *inside* the high resolution shell. Once again, we observed enhanced friction followed by stalling. Secondly, we performed a test-run starting the GC outside the 2nd shell. As it moved through the shell transition at 1.1 kpc, no detectable effect was observed.

3.5.2 The effect of varying $M_{\rm c}$

Figure 10 shows the decay rate of the GC as a function of the GC mass, $M_{\rm c}$ (solid lines); $M_{\rm c}$ is marked in solar masses. Overlaid are analytic predictions from equation 20 using $\ln\Lambda = 5$, as previously (dotted lines). For these simulations, we re-ran simulation NB3c but using 10 times the GC mass ($M_{\rm c} = 2 \times 10^6 {\rm M}_\odot$), and half of the GC mass ($M_{\rm c} = 1 \times 10^5 {\rm M}_\odot$). For reasons of computational expense, we ran these new runs at a lower resolution with 10^5 particles in each shell. We could not investigate smaller GC masses than $M_{\rm c} = 10^5 {\rm M}_\odot$, since then M_c approaches the mass of the heaviest particle and two-body effects dominate over dynamical friction.

Notice that the lower resolution runs are noisier and decay faster once the GC hits the core. This decay is due to the precession (due to numerical noise) of the GC orbit plane, discussed in section 3.4.4 and appendix 3.8, and is much smaller in the higher resolution runs. We explicitly checked that this is indeed the case using lower resolution runs of NB3c.

In all runs, the GC shows a reduced friction at the core region. Notice that the point at which the GC departs from Chandrasekhar like friction appears to be a weak function of the GC mass. This is to be expected: a more massive GC will more rapidly scatter the background particles and stall more quickly once it reaches the core region. However, it is tempting to suggest a simpler explanation: that equation 20 is failing simply because $M_{\rm en} = \eta M_c$; where $M_{\rm en}$ is the final mass enclosed and η is some constant of order unity. This is perhaps worrisome given the mass ratios, $M_{\rm en}/M_{\rm c}$, at the point of the onset of the stalling behaviour. These are, in order of increasing $M_{\rm c}$: [3,5,2]. However, we believe that the situation is not this simple for the following reasons: (i) if the stalling were a result only of $M_\mathrm{c} \simeq M_\mathrm{en}$, then it would not be a special property of constant density cores. We show in section 3.5.3, below, that the stalling behaviour does not occur for steeper density profiles, whatever the enclosed mass. (ii) The model we present in section 3.3 provides a good fit to the final density and velocity distribution of the background particles in the core suggesting that we have captured the correct physical explanation.

3.5.3 The effect of varying γ

Figure 11 shows the decay rate of the GC as a function of the central log-slope of the background density distribution, γ (solid lines); γ is marked on the plot. For these simulations, we re-ran simulation NB3c but using $\gamma = [0.1, 0.5]$. Also shown are results for a simulation with $\gamma = 1$ taken from Goerdt et al. (2006). Overlaid are analytic predictions from equation 20 using $\ln \Lambda = [8, 7, 3.5]$, in order of increasing γ (dotted lines). $\ln \Lambda$ is different for each of these simulations, reflecting the change in the underlying density distribution; similar results have been found elsewhere in the literature (see e.g. Just & Peñarrubia 2005). All simulations were high resolution ($\sim 10^6$ particles per shell), but since we are interested in the core stalling properties of the GC, we started the $\gamma = [0.1, 0.5]$ simulations at $\sim 400\,\mathrm{pc}$, rather than $\sim 1\,\mathrm{kpc}$ as previously.

The key point is that the $\gamma = 1$ model is well-fit by the Chandrasekhar form over the entire simulation time. This is despite the fact that $M_{en} \simeq M_c$ at $\sim 0.1\,\mathrm{kpc}$ for this run. This suggests that the core stalling behaviour is a special property of the harmonic core and not to do with the enclosed mass. However, the $\gamma = [0.1, 0.5]$ runs both show stalling behaviour despite not having a central core. This occurs because the GC itself *creates* a small core as it falls in and heats the background particle distribution. For initial density distributions steeper than $\gamma = 0.5$ this no longer occurs. In this case, the density profile does become shallower as a result of heating, but the heating is not sufficient to form a core in the centre before the GC falls all of the way in. The crosses on Figure 11 mark the radii at which the final density profile has a central log-slope shallower than -0.1. Recall that this is the same definition we used to define r_core earlier.

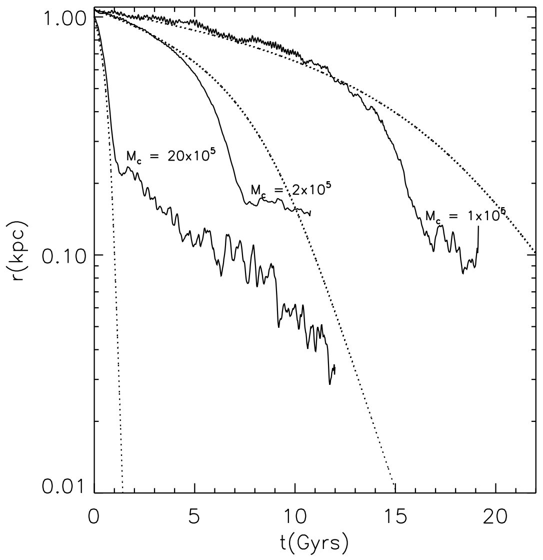

Figure 10: The decay rate of the GC as a function of $M_{\rm c}$ (solid lines); $M_{\rm c}$ is marked in solar masses. Overlaid are analytic predictions from equation 20 using $\ln\Lambda = 5$, as previously (dotted lines). For these simulations, we re-ran simulation NB3c (see Table 2) but using 10 times the GC mass ($M_{\rm c} = 2\times10^6{\rm M}_\odot$), and half of the GC mass ($M_{\rm c} = 1\times10^5{\rm M}_\odot$). $M_{\rm en}/M_{\rm c}$ at the point of the onset of the stalling behaviour is, in order of increasing $M_{\rm c}$: [3,5,2].

3.6 Conclusions

Using analytic calculations and N-body simulations we have shown that in constant density harmonic cores, sinking satellites undergo an initial phase of very rapid (super-Chandrasekhar) dynamical friction, after which they experience no dynamical friction at all. This occurs because, for the special case of harmonic potentials, there are stable solutions where the background particles move on epicycles about the in-falling satellite. The system moves rapidly into this stable configuration. In doing so, the satellite experiences a brief moment of enhanced friction. Once in equilibrium, there is no net momentum transfer between the background particles and the satellite and friction ceases. For density profiles with a central power law profile, $\rho \propto r^{-\alpha}$, the infalling satellite heats the background and causes α to decrease. For $\alpha < 0.5$ initially, the satellite generates a small central constant density core and stalls as in the $\alpha = 0$ case.

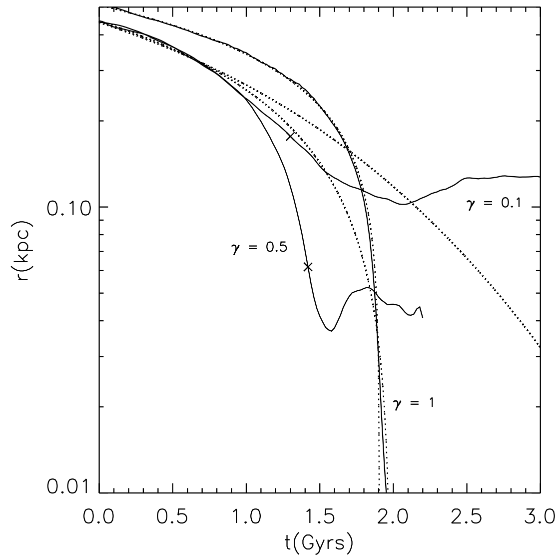

Figure 11: The decay rate of the GC as a function of the central log-slope of the background density distribution, γ (solid lines); γ is marked on the plot. Overlaid are analytic predictions from equation 20 using $\ln\Lambda = [8, 7, 3.5]$, in order of increasing γ (dotted lines). The crosses mark the radii at which the *final* density profile has a central log-slope shallower than -0.1. M_{en}/M_c at the point of the onset of the stalling behaviour is, in order of increasing γ: [4,1].

Our results concerning dynamical friction stalling in constant density cores are of broad astrophysical interest. Recent observational work suggests that galaxies may have central dark matter density cores, rather than the r^{-1} density cusps predicted by numerical simulations. Galactic bars orbiting in such potentials will experience very weak dynamical friction and can be very long-lived (in fact central density distributions do not need to be pure harmonic to see this effect, low-density will also lead to very little friction – see e.g. Debattista & Sellwood 1998 and Debattista & Sellwood 2000). Satellites falling into such galaxies will stall at the core radius and never make it to the centre. This point was investigated in a companion paper (Goerdt et al. 2006), where we suggested that a constant density core could solve the 'timing problem' for the GCs in the Fornax dwarf galaxy. Finally, recent work on merging black holes suggests that they can form a central constant density core in the background distribution (see e.g. Milosavljević et al. 2002; Ravindranath, Ho &

Filippenko 2002) prior to forming a hard binary. If true, our results suggest that this could further exacerbate the well-known problem of getting the binaries to coalesce. Their rate of hardening will stall, even before the majority of stars and dark matter have been ejected from the core, if the background distribution is close to constant density. This may point towards gas playing a more important role in bringing supermassive black holes together at the centre of galaxies (see e.g. Gould & Rix 2000).

3.7 Acknowledgements

We would like to thank Lucio Mayer, Victor Debattista, Scott Tremaine, Prasenjit Saha, Andrey Kravtsov, and the anonymous referee for useful comments which greatly aided the clarity of this work. AP is supported by a PPARC studentship. Special thanks go to Doug Potter, without whom none of this would have been possible. He has been the wizard of the zBox2 on which all of the simulations presented here were performed.

3.8 Two body noise and precession of the GC orbit plane

In this appendix we present a simple analytic model for the precession of the GC orbit plane due to particle noise and compare this with the simulations. We show that even quite small particle noise can lead to significant plane precession over ~ 100 dynamical times.

Under the assumption of linear background particle trajectories, it is straightforward to show that an interaction with one background particle will produce a velocity kick perpendicular to the GC's orbit plane given by (Binney & Tremaine 1987):

$$\delta v_z = \frac{2mbv^3}{G(M_c+m)^2}\left[1+\frac{b^2v^4}{G^2(M_c+m)^2}\right]^{-1} \tag{34}$$

where m is the mass of the background particle, M_c is the mass of the GC and b is the impact parameter (initial perpendicular separation) of the encounter. Such a kick occurs over $\sim$ a dynamical time.

Summing over all such encounters (all impact parameters) then gives the mean total velocity kick to the GC in $\sim$ a dynamical time. We sum over δv_z^2 to give the r.m.s. change; δv_z is of random sign and will sum to zero:

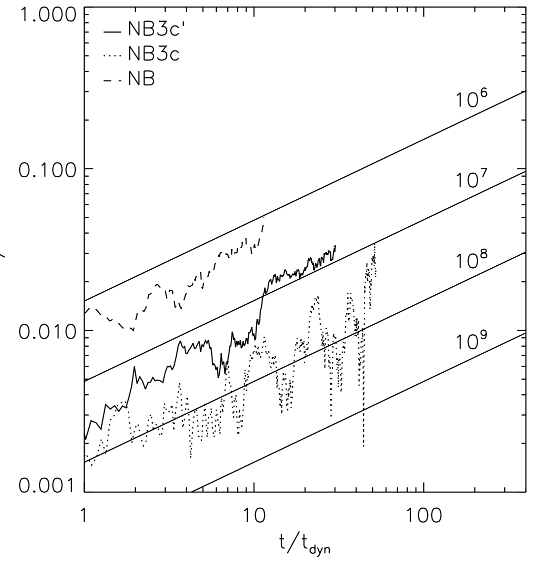

Figure 12: Evolution of the GC orbit plane in angle, θ, over the simulation time. The straight solid lines are for an analytic model that assumes a 2D random walk. Results are shown for increasing particle number, N. Overplotted are results from three typical N-body simulations: NB, NB3c and NB3c' - see Table 2 and this appendix for details; NB3c' is identical to NB3c, except that the GC initial orbit plane is different.

$$\begin{aligned}\frac{\Delta v_z^2}{v^2} &= \frac{1}{v^2}\int_{b_{\rm min}}^{b_{\rm max}} \delta v_z^2 \frac{2Nb}{b_{\rm max}^2} db \\ &= \frac{8}{2N}\left[\frac{x_{\rm min}^2 - x_{\rm max}^2}{(1+x_{\rm min}^2)(1+x_{\rm max}^2)} + \ln\left(\frac{1+x_{\rm max}^2}{1+x_{\rm min}^2}\right)\right] \\ &= \frac{8}{N}\ln\Lambda' \end{aligned} \tag{35}$$

$$x_{\rm max} = \frac{Nm}{M_c+m}\ ;\ x_{\rm min} = \frac{Nm}{M_c+m}\Lambda^{-1} \tag{36}$$

where v is now $\sim$ the velocity of the GC; $\Lambda = b_{\rm max}/b_{\rm min}$ is the term inside Coulomb logarithm that also appears in equation 20; N is the number of background particles inside $\sim b_{\rm max}$ (the GC orbit is assumed to lie in the x-y plane); and $\ln\Lambda' = 1/2[...]$ is defined by equation 35.

Notice that in the limit of large impact parameters, $b_{\rm max} \gg b_{\rm min} \gg$

$GM_c/v^2 \Rightarrow x_{\rm max} \gg x_{\rm min} \gg 1$, and equation 35 reduces to the more familiar form: $\Delta v_z^2/v^2 = (8/N)\ln\Lambda$. It is then independent of the GC mass.

In one orbit, the GC will move a mean z distance, $\Delta z \sim \Delta v_z t_{\rm dyn}$, where $t_{\rm dyn}$ is the orbit time. The mean change in angle over one orbit, $\Delta\theta$, of the vector normal to the GC orbit plane is then given by:

$$\Delta\theta \sim \tan^{-1}\left(\frac{\Delta z}{r}\right) = \tan^{-1}\left(2\pi\sqrt{\frac{8\ln\Lambda'}{N}}\right) \tag{37}$$

where we have assumed that the GC moves on a circular orbit of radius, r.

Any dependence on the underlying potential completely factors out in equation 37, and $\Delta\theta$ depends only on the number of particles, N, and very weakly on M_c/m.

The orbit plane can be tilted due to such scattering noise from the background distribution in two independent directions. Since the potential is spherical, there is no restoring force and once the plane has tilted, the probability it will tilt again is independent of its past history. Thus we may model the accumulated precession of the orbit plane by a 2D random walk. This gives:

$$\theta = \Delta\theta\sqrt{\frac{t}{t_{\rm dyn}}} \tag{38}$$

The orbit time at $r = r_{\rm core}$ for our model is given by $t_{\rm dyn} = 2\pi\sqrt{\frac{r^3}{GM(r)}} =$ 0.15 Gyrs. In Figure 12 we plot the mean orbit plane precession predicted by this random walk model, as a function of simulation time, $t/t_{\rm dyn}$. We use $b_{\rm max} = 1.5$ kpc and $b_{\rm min} = 10$ pc, which gives $\ln\Lambda = 5$, as in section 3.5. In section 3.5, we typically ran our N-body models for 10 Gyrs which corresponds to ~ 100 dynamical times. The straight solid lines show the effect of increasing the particle number, N. Notice that extremely high resolution is required to keep plane precession to a minimum over our simulation time: even with 10^7 particles we can expect a mean precession over the whole simulation of $\sim 7^{\rm o}$. Over-plotted are results from the NB, NB3c and NB3c' simulations (see Table 2). Recall that the NB model was a single shell model with 10^7 particles in total, with 10^3 within 300 pc. The NB3 simulations were three-shell models with 10^6 particles within 300 pc. NB3c' is a simulation which is identical to NB3c but with a different GC initial orbit plane. Notice that in all cases the plane precesses; it is not some numerical error introduced by the three shell model. The NB3 simulations show a smaller precession than the NB simulation as is expected given their higher effective resolution. Finally, notice that changing the initial GC orbit plane can alter the total precession quite dramatically (compare the NB3c and NB3c' simulations). This is to be expected given the random walk model, above.

The total particle number, N, in equation 37 is a slightly ill-defined quantity and so should not be equated exactly with the number of particles in the simulation (particularly for the 3-shell models). However, it is encouraging that our simple random walk model produces the correct mean slope for the plane precession and the correct scaling with particle number. It is clear that the 3-shell model has an advantage over the single shell model: it samples the core region with 1000 times the resolution of the single shell and shows much smaller two-body noise.

Throughout this paper, we present simulations which minimise the evolution of the orbit plane. It is important to note, however, that *all* of our simulations show the same central result: a period of super-Chandrasekhar friction, followed by stalling at the constant density core.

4 Core creation in galaxies via sinking massive objects: application to the puzzling binary nucleated galaxy VCC 128

4.1 Abstract

Massive objects sinking within galaxies or dark matter haloes via dynamical friction will exchange energy with central particles, ejecting them from the cusp and possibly creating a constant density inner region. We explore parameter space using numerical simulations and give empirical relations for the size of the resulting core within structures that have different initial cusp slopes. We show that simple energetic arguments can be used to predict these scaling laws. As an application we consider the dwarf spheroidal galaxy VCC 128 which has a double nucleus separated by less than a hundred parsecs. If this galaxy has a surrounding cold dark matter halo then these objects should sink the to centre of the cusp and coalesce in a few million years. We show that a likely solution is that the sinking nuclei would create a core equal to their current separation if the initial dark matter cusp is shallower than a slope of -1. The sinking objects would naturally stall at this radius for many Gyrs perhaps giving us an indirect observation of dynamical friction operating within the centre of a CDM halo.

4.2 Introduction

Any massive objects orbiting within a cuspy mass distribution are expected to lose energy and sink via dynamical friction (Chandrasekhar 1943; White 1983; Hernquist & Weinberg 1989; Capuzzo-Dolcetta & Vicari 2005). While spiralling inwards the massive perturber will transfer energy to central particles/stars etc, moving them to a larger orbital radius. One proposed effect of this process is to make a primordially cuspy dark matter distribution shallower (El-Zant, Shlosman & Hoffman 2001). A similar process will happen if a binary system is present at the centre of a distribution of lighter particles, for example a massive black hole binary in the centre of a stellar distribution can possibly explain the creation of a core in the light distribution as stars are ejected via three body encounters (Merritt et al. 2004).

In the prevailing ΛCDM cosmology primordial dark matter haloes are cuspy, having an inner density slope $\rho(r) \propto r^{\gamma}$ steeper than 1.0 (Dubinski

& Carlberg 1991; Diemand, Moore & Stadel 2005). Observations of dwarf galaxies seem to indicate that they have a cored mass distribution (Sánchez-Salcedo, Reyes-Iturbide & Hernandez 2006; Goerdt et al. 2006; Kleyna et al. 2003). Controversial evidence for cored mass distributions in dwarf spiral galaxies has been debated for over a decade (Moore 1994).

Any sufficiently compact sinking perturber will transform any host halo, that has been cuspy in the beginning, into a cored one at some scale. Once a core has formed then dynamical friction is no longer effective (Goerdt et al. 2006). Dynamical arguments show that sinking perturbers must stall at the outer edge of a core (Read et al. 2006).

In this paper we quantify this stalling behaviour as a function of perturber mass and central cusp slope. We give empirical scaling relations using high resolution N-body simulations and attempt to explain these using simple energetic arguments. As an example we attempt to explain the close separation of binary nuclei within the dwarf galaxy VCC 128 (Debattista et al. 2006). The two nuclei are expected to sink into the centre of a cuspy halo, and coalesce there on timescales which are extremely short compared to the age of the galaxy.

This paper is organised as follows: In section 2 we describe our analytical framework, which is supported using N-body simulations. In section 3 we apply our findings to VCC 128 and in section 4 we give our conclusions.

4.3 Transforming cusps to cores

We are interested in the effects of dynamical friction at modifying the central structure of dark matter haloes, stellar distributions etc, so we take as an initial distribution the α, β, γ law (Hernquist 1990):

$$\rho(r) = \frac{\rho_0}{(r/r_\mathrm{s})^\gamma \left[1 + (r/r_\mathrm{s})^\alpha\right]^{(\beta-\gamma)/\alpha}} \qquad (r \leq R_\mathrm{vir}) \tag{39}$$

In this equation we have 5 variables: ρ_0, r_s, α, β and γ. Since we focus on the very inner regions of the halo in our analysis, α and β are of little interest to us. We fix them at the commonly accepted values for cold dark matter haloes of 1.0 and 3.0, respectively. γ is the value we actually want to constrain so the missing parameters are ρ_0 and r_s.

We will take our fiducial model to represent a low mass dark matter halo typical of those surrounding dwarf galaxies with a circular velocity $v_\mathrm{c} = 50$

Halo	γ	$\rho_0/\mathrm{M}_\odot \mathrm{pc}^{-3}$	r_s	c
A	1.50	0.001333	10.3 kpc	7.5
B	1.00	0.009109	5.01 kpc	15.0
C	0.75	0.017732	3.91 kpc	19.0
D	0.50	0.027746	3.38 kpc	22.0

Table 3: The parameter list of the four different dark matter haloes, we use in our analytical and numerical calculations.

km s^{-1}. As our application, later we will consider VCC 128 which has an absolute bolometric luminosity of VCC 128 is $\mathrm{M_B}$ = -15.5 mag (Debattista et al. 2006). With that information we can estimate its circular velocity to be v_c = 35 - 65 km s^{-1} using the Faber-Jackson relation of dE's (de Rijcke et al. 2005). Assuming a concentration of 15 for $\gamma = 1.0$, which is a common value for cosmologically motivated dwarf spheroidals (Łokas 2002), we get a $r(v_\mathrm{peak})$ of 10.75 kpc. For our other models we keep v_peak as well as $r(v_\mathrm{peak})$ constant, just varying γ. This leads to the parameters given in Table 3 and to the circular velocity curves and radial density profiles, which are shown in Fig. 13 and Fig. 14, respectively.

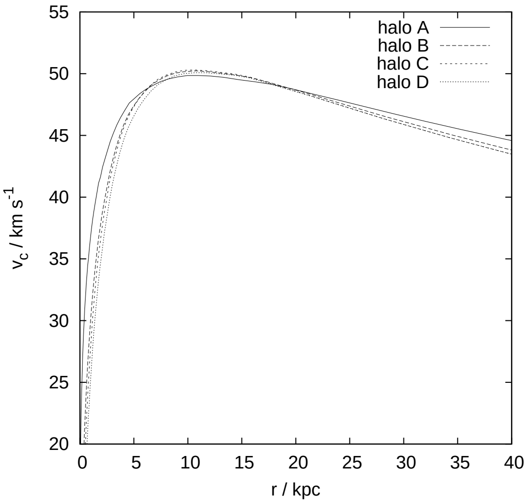

Figure 13: Circular velocities of the four different dark matter haloes, we use in our analytical calculations. All four of them peak at 50 km s^{-1}.

The dynamical friction sinking timescale of a massive compact object can be derived using the Chandrasekhar dynamical friction formula (Chan-

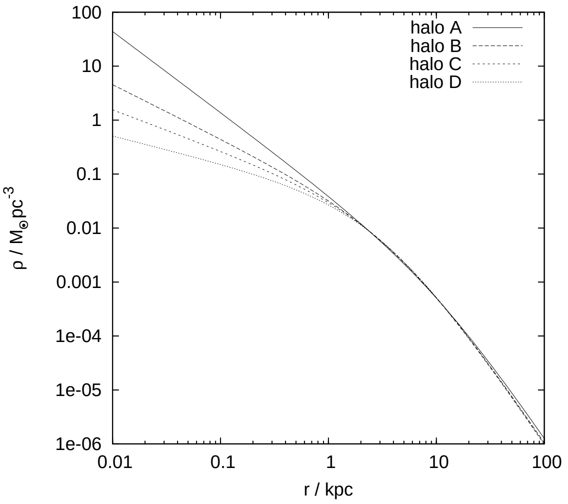

Figure 14: Radial density profiles of the four different dark matter haloes, we use in our analytical calculations.

drasekhar 1943). The final equation comes out to be:

$$\begin{aligned}\frac{\mathrm{d}r}{\mathrm{d}t} &= -\frac{4\pi\ln\Lambda(r)\rho(r)G^2M_{\mathrm{pert}}r}{v_{\mathrm{c}}^2(r)d\left[rv_{\mathrm{c}}(r)\right]/dr}\left\{\mathrm{erf}\left[\frac{v_{\mathrm{c}}(r)}{\sqrt{2}\sigma(r)}\right]\right.\\ &- \left.\frac{2v_{\mathrm{c}}(r)}{\sqrt{2\pi}\sigma(r)}\exp\left[\frac{-v_{\mathrm{c}}^2(r)}{2\sigma^2(r)}\right]\right\}, \qquad (40)\end{aligned}$$

where $v_{\mathrm{c}}(r)$ is the circular speed at radius r, $\ln\Lambda(r)$ the Coulomb logarithm, M_{pert} is the mass of the perturber. $\rho(r)$ is the density of the dark matter halo at radius r according to equation (39) and $\sigma(r)$ is the one-dimensional velocity dispersion of the halo.

4.3.1 N-body simulations

We have performed N-body simulations with the haloes presented in Table 3 to study the effects of different mass perturbers on modifying the density profiles. Equilibrium N-body representations of these haloes have been created with the algorithm described in Kazantzidis, Magorrian & Moore (2004) using the multimass technique of Zemp (2006). This gives structures that have an effective resolution in the region of interest equivalent to using $\sim 10^{10}$ single mass particles. We first use a single particle of mass $M_{\mathrm{pert}} = 5 \times 10^5$ M$_\odot$ with a softening length of 2 pc starting at 0.4 kpc on a circular orbit. You can see the trajectories of the single perturber in the four different haloes in Fig. 15.

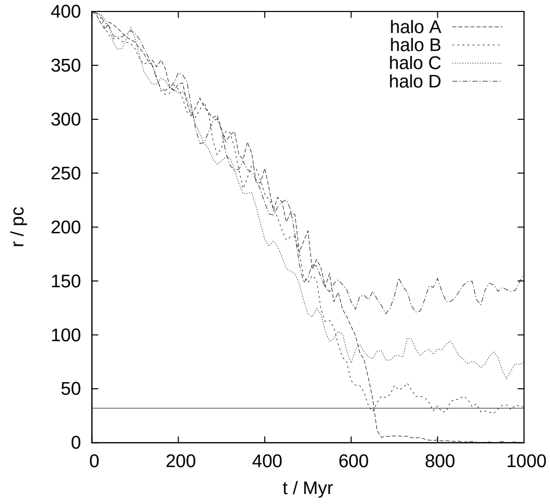

Figure 15: Simulated position of a single nucleus within its host halo as a function of time, assuming an initial true distance of 400 pc. The horizontal line shows the observed projected distances of the two nuclei in VCC 128.

On all trajectories you can see a kickback, which occurs after a first point of closest approach (fpca). Now the nucleus moves away for a while, reaches a maximum to come back to a second point of closest approach (spca), where it finally stalls. Usually the distance of the nucleus from the centre of the halo is pretty much the same at fpca and at spca. The total duration as well as the height of the kickback are linked to the perturbers mass via a power law. We define the height of the kickback to be the difference between the lowest and the highest point during the kickback period. The lowest point during kickback period is the smaller one of fpca and spca. It is interesting to see that the local minima to the right and to the left of the kickback, fpca and spca, are, to very good accuracy at the same height. We will talk about this phenomenon in more depth later.

The stalling radii at fpca as a function of γ are plotted in Fig. 16, they can be fitted with an equation of the following form:

$$r_{\mathrm{stall}} = A \exp\left(B\gamma\right) \tag{41}$$

with $A = 738$ pc and $B = -3.29$.

We ran two more series of simulations keeping the haloes fixed (haloes

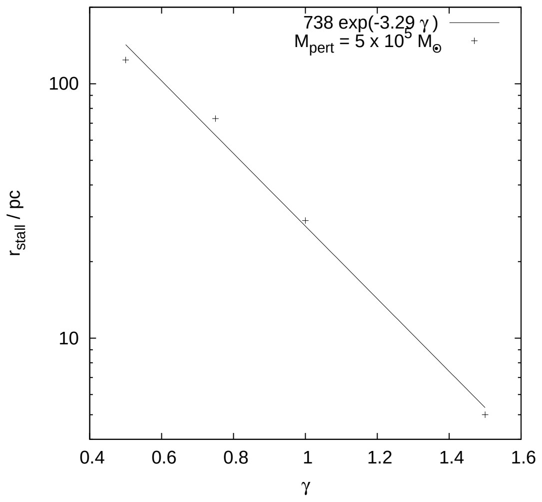

Figure 16: The stalling radii at fpca as a function of γ for $M_{\rm GC} = 5 \times 10^5$ $\mathrm{M}_{\odot}$, together with the best fit exponential.

B and C) and varying the mass of the perturber $M_{\rm GC}$. In the simulations with halo B the nuclei start at 0.8 kpc and in the simulations with halo C the perturber start at 1.2 kpc so that in each case the orbits starts well outside the final core radius. (We could have started the perturber in halo B at 1.2 kpc as well and we would have got the same results, but this would have produced avoidable computational costs.) Results in all simulations are shown using circular orbits but similar scaling laws were found using more eccentric orbits. You can see the trajectories of the single perturber in halo B in Fig. 17 and for halo C in Fig. 18. The stalling radii for haloes B and C as a function of $M_{\rm pert}$ are plotted in Fig. 24 for fpca and spca. The data can be fitted with equation (51) with $A = 0.07$ pc and $B = 0.48$ for $\gamma = 1.00$ and $A = 0.18$ pc and $B = 0.46$ for $\gamma = 0.75$ These values a very close to the theoretical values given in the last section. It is apparent that the slopes agree very well. The mass deficits within the stalling radii for haloes B and C as a function of perturbers mass are plotted in Fig. 25 at fpca and spca. The data can be fitted with an equation of the following form:

$$M_{\rm def} = A \left(\frac{M_{\rm pert}}{\mathrm{M}_{\odot}} \right)^{B} \tag{42}$$

with $A = 3.40$ $\mathrm{M}_{\odot}$ and $B = 0.84$ for $\gamma = 1.00$ and $A = 1.26$ $\mathrm{M}_{\odot}$ and

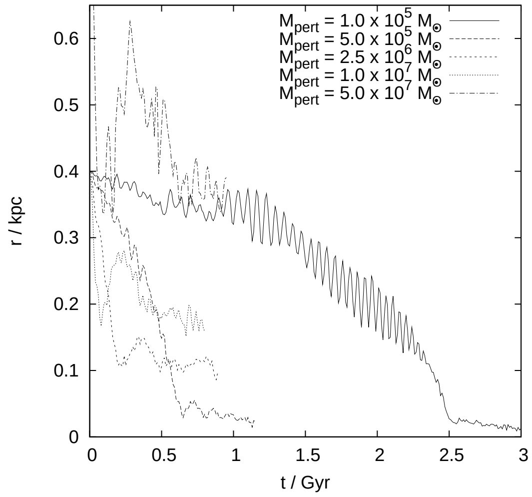

Figure 17: Distance from the centre of potential of a single perturber as a function of its mass within halo B as a function of time.

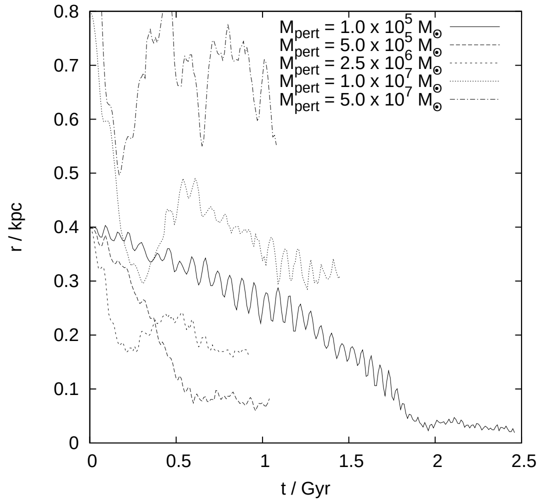

Figure 18: Simulated position of a single perturber with varying mass within halo C as a function of time.

$B = 0.93$ for $\gamma = 0.75$ [compare this expression with equations (56) and (58)]. It becomes apparent that the mass deficit does not change during the kickback period. Very unlike the mass distribution: The density profiles of the host halo at fpca an at spca are plotted in Figs. 19, 20, 21 and 22.

One can clearly see that the mass distribution changes significantly. The

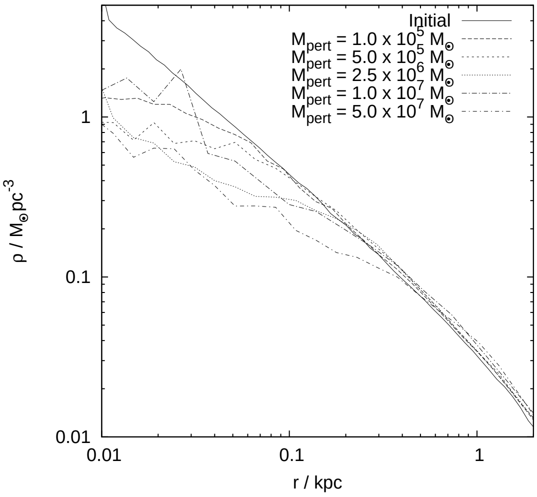

Figure 19: Density profiles of the host halo with $\gamma = 1.0$ (halo B) at the first point of closest approach for the different nuclei masses M_{pert}.

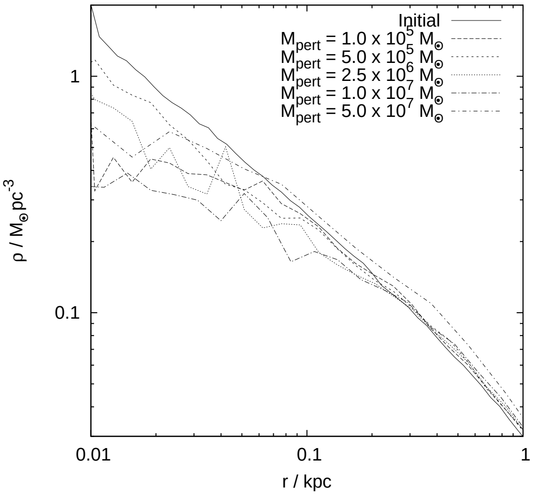

Figure 20: Density profiles of the host halo with $\gamma = 0.75$ (halo C) at the first point of closest approach for the different nuclei masses M_{pert}.

haloes settles down into a new equilibrium between fpca and spca. The radial density profiles change from being cuspy to having a core.

You can see the duration of the kickback as a function of M_{pert} in Fig. 26,

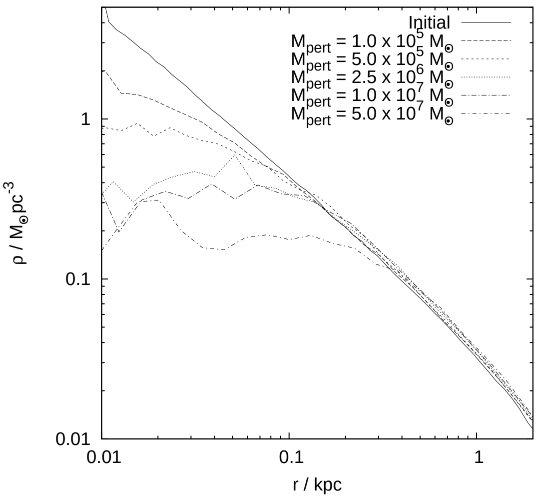

Figure 21: Density profiles of the host halo with $\gamma = 1.0$ (halo B) at the second point of closest approach for the different nuclei masses M_{pert}.

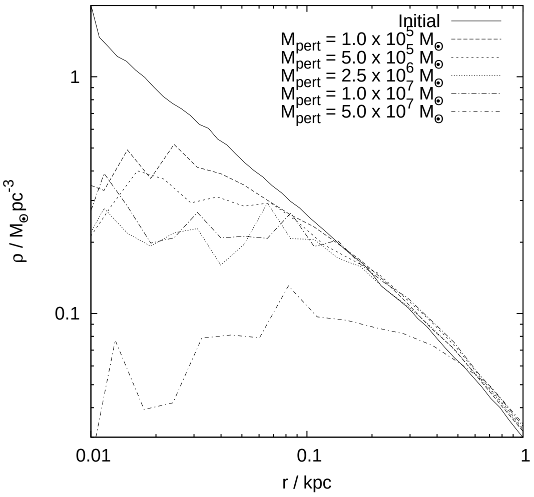

Figure 22: Density profiles of the host halo with $\gamma = 0.75$ (halo C) at the second point of closest approach for the different nuclei masses M_{pert}.

the data can be fitted with an equation of the following form:

$$t_{\text{kickback}} = A \left(\frac{M_{\text{pert}}}{\text{M}_\odot} \right)^B \tag{43}$$

with $A = 10.5$ Myr and $B = 0.21$ for $\gamma = 1.00$ and $A = 129.9$ Myr and

$B = 0.08$ for $\gamma = 0.75$, Which is very close to the theoretical approach of equations (63) and (64). You can see the height of the kickback as a function of M_{pert} in Fig. 23, the data can be very well fitted with an equation of the following form:

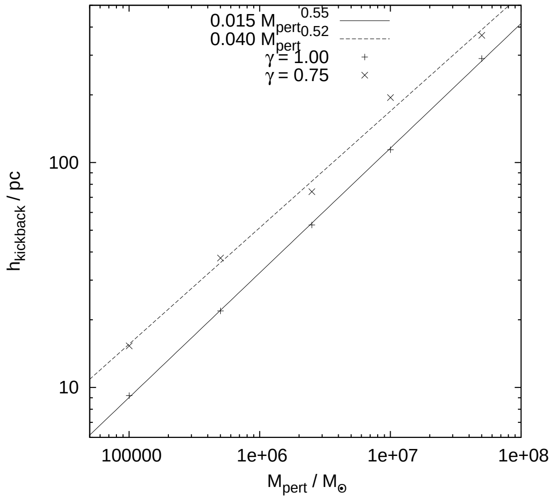

Figure 23: Height of the kickback as a function of M_{pert} for haloes B and C, together with their best fit exponentials.

$$h_{\mathrm{kickback}} = A \left(\frac{M_{\mathrm{pert}}}{\mathrm{M}_{\odot}} \right)^{B} \tag{44}$$

with $A = 0.015$ pc and $B = 0.55$ for $\gamma = 1.00$ and $A = 0.040$ pc and $B = 0.52$ for $\gamma = 0.75$.

4.3.2 Analytical model

While the massive object sinks in from its initial position r_{initial} down towards the stalling radius r_{stall}, which we assume to be the core radius of the halo r_{core} as well, it loses energy: Its kinetic energy gets less positive and its potential energy becomes more negative. This energy is transferred to the host halo, which is transformed from being a cuspy pure NFW-halo (Navarro, Frenk & White 1996) (In case of halo B, the expressions for halo C are analogue) with the usual density profile:

$$\rho_{\mathrm{cusp}}(r) = \frac{\rho_0}{(r/r_{\mathrm{s}})(1 + r/r_{\mathrm{s}})^2} \tag{45}$$

[see equation (39)] into a cored halo (compare Figs. 19 to 22) with the following density profile:

$$\rho_{\rm core}(r) = \begin{cases} \dfrac{\rho_1}{(r_{\rm core}/r_{\rm s})(1+r_{\rm core}/r_{\rm s})^2} & (r \leq r_{\rm core}) \\ \\ \dfrac{\rho_1}{(r/r_{\rm s})(1+r/r_{\rm s})^2} & (r \geq r_{\rm core}) \end{cases} \tag{46}$$

The new normalisation factor ρ_1 has to be chosen in a way the the mass between the centre of the halo and its virial radius is the same for both models. The total energy difference between this two models is half their potential energy difference, due to the virial theorem. The total potential energy of a halo is

$$E_{\rm pot} = \frac{1}{2}\int_0^{\infty} 4\pi r^2 \rho(r)\Phi(r){\rm d}r \tag{47}$$

The potential $\Phi(r)$ of a spherical symmetric halo is given by

$$\Phi(r) = -4\pi G\left[\frac{1}{r}\int_0^{\rm r} \rho(r')r'^2{\rm d}r' + \int_{\rm r}^{\infty} \rho(r')r'{\rm d}r'\right] \tag{48}$$

With the help of equations (45) to (48) one can calculate the total energy difference of the two halo models as a function of core radius $r_{\rm core}$.

The energy provided by the perturber is the difference between its total energy at $r = r_{\rm initial}$ within the cuspy halo and its total energy at $r = r_{\rm core}$ within the cored halo. So:

$$\begin{aligned} E_{\rm diff} &= M_{\rm pert}\left\{\frac{1}{2}\left[v_{\rm cusp}(r_{\rm initial})\right]^2 + \Phi_{\rm cusp}(r_{\rm initial})\right. \\ &- \left.\frac{1}{2}\left[v_{\rm core}(r_{\rm core})\right]^2 - \Phi_{\rm core}(r_{\rm core})\right\} \end{aligned} \tag{49}$$

$v_{\rm cusp}(r)$ and $v_{\rm core}(r)$ are the circular velocities within the respective haloes at position r. The can be computed according to

$$v_{\rm cir}(r) = \sqrt{\frac{4\pi G}{r}\int_0^{\rm r} r'^2\rho(r'){\rm d}r'}, \tag{50}$$

with $\rho(r')$ being the density profile of the respective halo. With equation (49) one can compute the energy lost by a sinking in globular as a function of $r_{\rm core}$. Combining equations (47) and (49) one gets an expression for the core radius $r_{\rm core}$ as a function of globular cluster mass $M_{\rm pert}$. This expression is plotted on top of the data of the N-body simulations from the next paragraph in Fig. 24. This analytic approach has naturally two shortcomings: (a) the energy

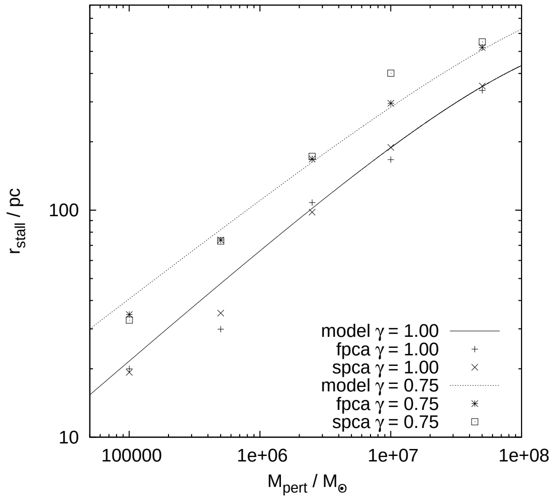

Figure 24: The stalling radii at the first as well as at the second point of closest approach as a function of perturber mass for haloes B and C, together with our theoretical models.

needed to create a core of given size r_{core} is too large because in our model the displaced mass is evenly distributed between r_{core} and r_{vir}. In reality this mass is rather located just outside r_{core}. (b): The stalling radius r_{core} depends too much on the initial radius r_{initial}, because in our model all the energy is transferred to the core. In reality the perturber transfers a significant amount of its energy on its way to the outer parts of its host halo. Since the fraction of particles affected is smaller in the outer regions the outer density profile is not significantly modified.

The theoretical models you can see in Fig. 24 can be approximated in the low M_{pert} regime by a power law of the form:

$$r_{\mathrm{stall}} = A \left(\frac{M_{\mathrm{pert}}}{\mathrm{M}_{\odot}} \right)^{B} \tag{51}$$

with $A = 0.09$ pc and $B = 0.48$ for $\gamma = 1.00$ and $A = 0.28$ pc and $B = 0.43$ for $\gamma = 0.75$. To calculate the mass deficit M_{def} in the centre of the halo, we assume that the stalling radius r_{stall} is equal to the core radius r_{core}. Additionally we know from equation (39) that the density $\rho(r)$ goes as r^{-1} in the central region of the halo for halo B. So:

$$\rho(r) = \frac{C}{r} \tag{52}$$

The mass difference between a cored and a cuspy halo can by computed via:

$$M_{\mathrm{def}} = \int_0^{\mathrm{r_{core}}} 4\pi r^2 \left[\rho\left(r\right) - \rho\left(r_{\mathrm{core}}\right)\right] \mathrm{d}r \tag{53}$$

using equation (52) this can be resolved to give:

$$\begin{aligned} M_{\mathrm{def}} &= 4\pi \left(\int_0^{\mathrm{r_{core}}} r'^2 \frac{C}{r'} \mathrm{d}r' - \int_0^{\mathrm{r_{core}}} r'^2 \frac{C}{r_{\mathrm{core}}} \mathrm{d}r' \right) \qquad (54) \\ &= \frac{2}{3}\pi C r_{\mathrm{core}}^2 \qquad (55) \end{aligned}$$

Substituting equation (51) for r_{core} we get the following expression for the mass deficit:

$$M_{\mathrm{def}} = \frac{2}{3}\pi A^2 C \left(\frac{M_{\mathrm{pert}}}{\mathrm{M}_{\odot}}\right)^{2B} \tag{56}$$

This expression is plotted on top of the data of the N-body simulations from the next paragraph in Fig. 25. For halo C equation (52) has to be replaced

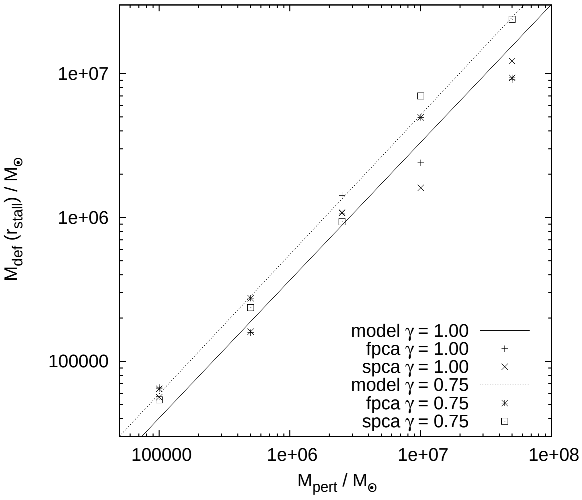

Figure 25: Mass deficits at the first point as well as at the second point of closest approach as a function of perturber mass for haloes B and C, together with our theoretical models.

by

$$\rho(r) = \frac{C}{r^{0.75}}, \tag{57}$$

when evaluating these expressions, one has to be careful, because C has different units for $\gamma = 1.0$ and $\gamma = 0.75$. The final equation comes out to be:

$$M_{\mathrm{def}} = \frac{4}{9}\pi A^{9/4} C \left(\frac{M_{\mathrm{pert}}}{\mathrm{M}_{\odot}}\right)^{9B/4} \tag{58}$$

This expression is plotted on top of the data of the N-body simulations from the next paragraph in Fig. 25 as well.

The duration of the kickback is proportional to the crossing time t_{cross} within the core, which is

$$t_{\mathrm{cross}} = \frac{r_{\mathrm{core}}}{v_{\mathrm{cir}}\left(r_{\mathrm{core}}\right)}. \tag{59}$$

Putting in the usual equation for $v_{\mathrm{cir}}(r_{\mathrm{core}})$, we get:

$$t_{\mathrm{cross}} = \frac{\left(r_{\mathrm{core}}\right)^{3/2}}{\sqrt{GM_{\mathrm{enc}}}}, \tag{60}$$

where M_{enc} is the mass within r_{core}, which can be computed as follows:

$$M_{\mathrm{enc}} = \int_0^{\mathrm{r_{core}}} 4\pi r^2 \rho(r)\mathrm{d}r \tag{61}$$

Using equation (52) this comes out to be:

$$M_{\mathrm{enc}} = 2\pi C r_{\mathrm{core}}^2 \tag{62}$$

Putting this into equation (60) and using equation (51) as well, we get as an expression for the duration of the kickback in case of halo B:

$$t_{\mathrm{kickback}} = D\sqrt{\frac{A}{2\pi CG}} \left(\frac{M_{\mathrm{pert}}}{\mathrm{M}_{\odot}}\right)^{B/2}, \tag{63}$$

with D being a free parameter, which comes out to be 27.188. This expression is plotted on top of the data of the N-body simulations from the next paragraph in Fig. 26. For Halo C we have to replace equation (52) again by

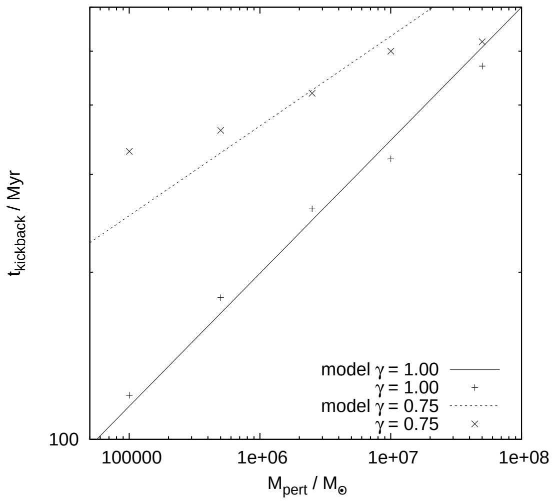

Figure 26: Duration of the kickback as a function of $M_{\rm pert}$ for haloes B and C, together with our theoretical models.

equation (57) and we get finally:

$$t_{\rm kickback} = D\frac{3A^{3/8}}{4\sqrt{\pi C G}}\left(\frac{M_{\rm pert}}{\rm M_\odot}\right)^{3B/8}, \tag{64}$$

with D = 27.188, as before. This expression is plotted on top of the data of the N-body simulations from the next paragraph in Fig. 26, as well.

4.4 Application to VCC 128

This stalling behaviour can nicely be applied to VCC 128, a dwarf spheroidal galaxy (dSph) at the outskirts of the Virgo cluster. A very close binary nucleus has recently been discovered there (Debattista et al. 2006). The two nuclei are very similar in their appearance with masses estimated to be 5×10^5 $\rm M_\odot$. These authors found altogether 3 dSph galaxies with double nuclei, looking at HST archival images of 50 dwarf spheroidals from a survey by Lotz, Miller & Ferguson (2004). The projected distance of the two nuclei in VCC 128 is 32 pc. This extremely small distance between the two nuclei that have masses comparable to globular clusters is very puzzling, because of dynamical considerations related to the friction-caused sink-in timescales (Chandrasekhar 1943).

Using equation (40) we can calculate the time it would take for one of the nuclei to sink to the centre of the system. In all our calculations we assume a constant Coulomb logarithm $\ln\Lambda(r) = 4.0$ (see Peñarrubia, Just & Kroupa 2004, for a detailed discussion of $\ln\Lambda$ varying with r). If one takes 44 pc as the initial true separation from the globular cluster to the centre of its host halo then for halo A the total sink-in time is computed to be 7.4 Myr, Halo B's sink-in-time is 13.9 Myr, Halo C's sink-in time is 38.1 Myr and Halo D's sink-in time is 171 Myr. The sink-in behaviour of the nuclei for all four cases can be seen in Fig. 27.

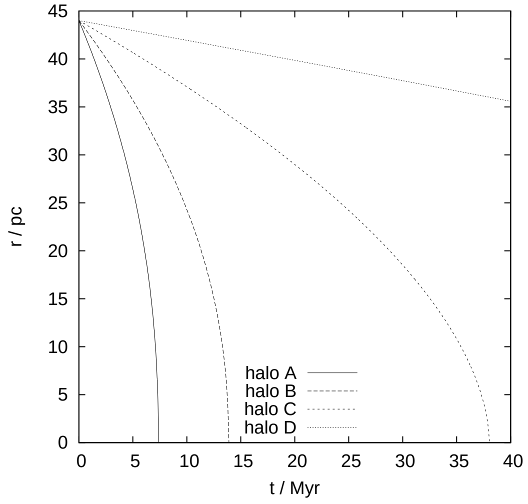

Figure 27: Analytical computed position as a function of time, during the Chandrasekhar sink-in period for our four haloes, assuming an initial true distance of the nucleus from the centre of 44 pc.

A possible mechanism which would stop a nucleus from sinking in is the stalling effect described by Read et al. (2006). Those authors found that a massive perturber would not sink in anymore but stall immediately as soon as it hits a harmonic constant density core. This effect is amplified by the fact that the sinking objects replace mass (El-Zant, Shlosman & Hoffman 2001; Merritt et al. 2004). So while a globular cluster is sinking into the very centre and it removes some of the dark matter particles from the innermost part of the halo. By doing so it transforms a primordial cusp into a core. This is mechanism which is easily capable of transforming cusps into cores unlike tidal stripping as N-body simulations of CDM satellites indicate (Kazantzidis et al. 2004) This happens by the following mechanism:

Debattista et al. (2006) tried to explain their discovery by employing a scheme of a nuclear disk surrounding a supermassive black hole (SMBH), a situation similar to the one in M31 (Tremaine 1995). This explanation, however, is not very convincing, because low mass galaxies are inefficient in forming SMBHs (Ferrarese 2002).

To emphasise how important these findings are we will, for this section, assume that the stalling effect described in the last two sections does not exist and the two nuclei in VCC 128 will sink in as predicted in equation (40) and Fig. 27. As already mentioned, the calculations presented here are based upon the observations from (Debattista et al. 2006). Refering to this work, we will taken as given throughout the paper that 3 out of 50 dSph have double nuclei with a projected distance of 32 pc. Our main assumptions are that all dwarf galaxies, for which no double nuclei have been observed, (a) do not have double nuclei at their centres, (b) lost their double nuclei because of a sink-in process due to dynamical friction, and (c) have double nuclei as close as the ones in VCC 128 (this assumption is made not only for the sake of numerical convenience, but also because of lack of precise observational measurements). However, it is important to mention that there are uncertainties entering these assumptions: Out of the 47 dwarf ellipticals, which do not have double nuclei, there might be some which actually do have such nuclei but the latter are too close to each other to be observed. Moreover, not all dwarf galaxies necessarily developed double nuclei during their lifetime.

We ran an additional series of simulations with two perturbers on either coplanar or perpendicular orbits. Again we used the haloes presented in Table 3. The stalling behaviour is shown in Fig. 28.

In halo A the nucleus does not stall, in halo B it stalls in a first step at exactly 32 pc (This can be seen very beautifully in Fig. 15), in haloes C and D it stalls in a first step way above 32 pc. These results suggest for slopes like 1.5 or steeper that Read stalling does indeed not crucially change the results we derived analytically. However for slopes shallower than 1.0 Read stalling does affect our results quite dramatically.

To summarise our findings: We can indeed exclude all very steep inner log density slopes like 1.5. The most likely explanation for the observation is however that the two nuclei transformed an initially fairly steep inner log density slope like 1.0 or 0.75 into a core during its initial sinking period. The nuclei would then stall at the edge of this freshly created core. So the existence of the binary nucleus in VCC 128 can be interpreted as an indirect evidence

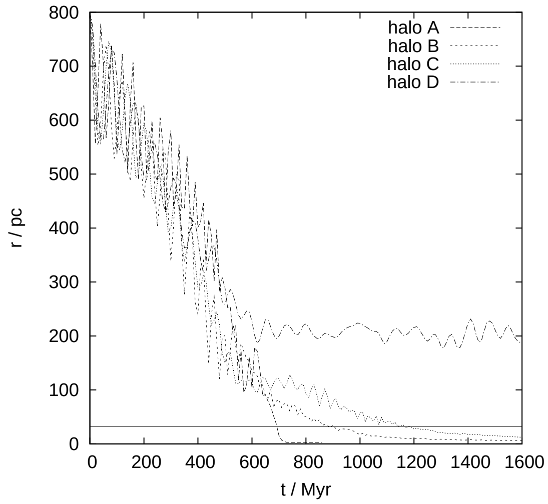

Figure 28: Separation of the two perturbers as a function of time, assuming an initial true separation of 800 pc and perpendicular orbits. The horizontal line shows the observed projected distances in VCC 128.

for dynamical friction. A very shallow inner log density slope like 0.75 or smaller seems to be quite unlikely as well, because the globular clusters would have stalled far further away then 32 pc. More likely distances here are 100 - 200 pc (See Fig. 28). Therefore one can deduce that an underlying dark matter halo obeying a NFW-halo provides the best explanation for the shown observations.

Further on, we can state, that the two globulars have to be on almost perfectly circular, very coplanar orbits, otherwise they would have collided and merged a long time ago, because their dynamical times are so small.

Throughout the paper we will assume that out of two orbiting nuclei one sinks to the centre of the underlying dark matter distribution and the other one is orbiting it afterwards. So we interpret the distance between the two nuclei as the distance of one nucleus to the centre of the dark matter distribution. We performed several N-body simulations to verify that this assumption holds.

We assume that the vector connecting the two nuclei has a random orientation. So the probability distribution of its inclination is $\Psi(i) = \cos(i)$. We define inclination so when it is equal to $0°$ there is a right angle between the line of sight and the vector. So for example we can say that in $P_{\mathrm{angle}} = 70\%$ of the cases the inclination is lower than $43°$ or the de-projected distance between the nuclei is lower than 44 pc. To make a start, we will use this value as the true distance.

As already mentioned earlier, for halo A the total sink-in time is computed to be 7.4 Myr. We assume that the current age of the galaxy is 5.0 Gyr. So the time it takes for the two nuclei to coalesce is about 0.15% of the lifetime of the galaxy. This means that it would be highly improbable to observe binary nuclei in the present. We will discuss the comparison of the probabilities later in the text. Halo B's sink-in-time is 13.9 Myr, which is 0.28% of the lifetime of the galaxy. Again this timescale seems short compared to occurrence of binary nuclei in dSphs to serve as an acceptable model. Halo C's sink-in time is 38.1 Myr. This is 0.76% of the lifetime of the galaxy. Even this timescale seems too short. Halo D's sink-in time is 171 Myr, about 3.4% of the galaxy's age, a timescale, which may be acceptable. The sink-in behaviour of the nuclei for all four cases can be seen in Fig. 27.

We want to elaborate a bit further on the comparison of probabilities. The sample we are working with has 50 galaxies in total, out of which 3 have double nuclei. For halo C the double nuclei would survive for about 0.76 % of the lifetime of the galaxy. So when we look at one random galaxy at a random time, the probability of seeing a double nucleus is $P_{\mathrm{dn}} = 0.0076$. The probability of seeing more than 2 galaxies with double nuclei in a sample of 50 is given by the cumulative binomial distribution:

$$P(n_{\mathrm{dn}} > 2) = 1 - \sum_{j=0}^{2} \binom{50}{j} (P_{\mathrm{dn}})^j (1 - P_{\mathrm{dn}})^{50-j} \tag{65}$$

For the values of our halo C we have $P(n_{\mathrm{dn}} > 2) = 0.662\%$ or alternatively $P(n_{\mathrm{dn}} < 3) = 99.34\%$. This values give the impression, that we can rule out model C to better than 95%. Unfortunately we assumed the inclination angle i to be smaller than 43°, this assumption holds only in $P_{\mathrm{angle}} = 70\%$ of all the cases. Therefore we can exclude halo C only with a probability of $P^{\mathrm{exclude}}_{\mathrm{Analytic}} = P_{\mathrm{angle}} P(n_{\mathrm{dn}} < 3) = 69.5\%$. So we start over and increase the maximum allowed inclination angle i_{max}, redoing the whole analysis in order to maximise $P^{\mathrm{exclude}}_{\mathrm{Analytic}}$ for each halo. In Table 4 you can see those values for the different haloes. A clear trend becomes apparent, what the excludability concerns: it increases with increasing γ. This is very intuitive, as well. So it is valid to say that there is an upper limit on γ.

In order to double-check these analytical predictions we presented here, we run a series of Monte Carlo simulations. These simulations were designed

Halo	γ	$i_{\max}$	P_{angle}	$P^{\text{exclude}}_{\text{Analytic}}$	$P^{\text{exclude}}_{\text{MonteCarlo}}$
A	1.50	72.6°	95.4%	93.87%	$98.68\% \triangleq 2.45\sigma$
B	1.00	69.1°	93.4%	90.98%	$97.86\% \triangleq 2.30\sigma$
C	0.75	62.9°	89.0%	83.85%	$95.52\% \triangleq 2.00\sigma$
D	0.50	46.9°	73.0%	52.52%	$73.49\% \triangleq 1.11\sigma$

Table 4: Summary of the statistical implication of our analytical calculations for the different halo models.

as follows: We draw a random inclination angle i, according to its probability density distribution $\Psi(i) = \cos(i)$. Then we calculate the true distance between the two nuclei and determine their sink-in time, as well as the sink-in time fraction f_{si} which is the fraction the sink-in time occupies out of the galaxies total lifetime. This value corresponds to the probability of seeing a double nucleus in a random galaxy at a random time P_{dn}, mentioned earlier in the text. Now we draw for each of the 50 galaxies a random time fraction f_{rt}, an evenly distributed number between 0 and 1. If more than 2 out of the 50 random time fractions are smaller than the sink-in time fraction ($f_{\text{rt}} < f_{\text{si}}$) the respective halo model cannot be ruled out. If for less then 3 galaxies the random time fractions are bigger then the sink-in time fraction ($f_{\text{rt}} > f_{\text{si}}$) the respective halo model can be ruled out. Instead of drawing 50 random time fractions one can modify the sink-in time fraction according to equation (65) to get a combined sink-in time fraction f_{csi}, a value which corresponds to the $P(n_{\text{dn}} < 3)$ mentioned earlier in the text. So for a random inclination angle i we can define:

$$f_{\text{csi}}(i) = \sum_{j=0}^{2} \binom{50}{j} \left[f_{\text{si}}(i)\right]^{j} \left[1 - f_{\text{si}}(i)\right]^{50-j} \tag{66}$$

Now we can compare the combined sink-in time fraction f_{csi} of our random inclination angle i with a single random time fraction f_{rt}. If the random time fraction is smaller then the combined sink-in time fraction ($f_{\text{rt}} < f_{\text{csi}}$) the respective halo model cannot be ruled out. If the random time fraction is bigger then the sink-in time fraction ($f_{\text{rt}} < f_{\text{csi}}$) the respective halo model can be ruled out. Repeating this calculation several times to get a Monte Carlo statistic we get the exclusion probabilities given in Table 4. The results by this method, can be obtained analytically as well, by integrating the combined sink-in time fraction f_{csi} over all angles normalised by their probability density:

$$P^{\text{exclude}}_{\text{MonteCarlo}} = \int_0^{\pi/2} \cos(i) f_{\text{csi}}(i) \mathrm{d}i \tag{67}$$

The Monte Carlo method gives systematically higher values than the analytical approach, because in the latter we did some implicit conservative assumptions in order to make the whole analysis feasible. Namely that the true distance is equal to (32 pc / cos i_{max}) with a probability of P_{angle} and equal to infinity with a probability of (1 - P_{angle}). In the Monte Carlo approach these assumptions are not necessary any more. Here we work with the true distributions. Therefore we are able to gain the most significance out of the information we have.

Looking carefully at the probabilities given in Table 4 we must come to the conclusion that in absence of the cusp-core transforming mechanism described in the last two section the inner log density slope of VCC 128 must be shallower than 1.0.

4.5 Conclusions

Taking as given the observations by Debattista et al. (2006), we have used dynamical and statistical arguments to show the following points:

- The inner log density slope γ of the dark matter halo underlying VCC 128 must be much less than 1.5. Otherwise the dynamical friction sink-in times are so tiny in comparison to the lifetime of the galaxy that one would run into a fine tuning problem.

- When simulating the situation in VCC 128, we see a stalling effect, as described by Read et al. (2006). The globular clusters coming from outside do not sink any further then a give stalling radius, which depends on the inner log density slope γ.

- The primordial inner log density slope γ must be much bigger than 0.75 for VCC 128. Otherwise globular clusters would stall much above the 32 pc they are seen at right know. One would have to wonder by what mechanism they would have sunk in to their current position.

- The binary nucleus of VCC 128 has to bee seen as an indirect evidence for dynamical friction, taking ΛCDM for granted: In this system dynamical friction always moves two globulars into positions which are of order 32 pc apart, completely independed of where they have been placed in the beginning.

- The two globulars have to be on almost perfectly circular, very coplanar orbits, otherwise they would have collided and merged a long time ago, because their dynamical times are so small.
- We describe a mechanism which is easily capable of transforming primordial cusps into cores unlike tidal stripping as N-body simulations of CDM satellites indicate (Kazantzidis et al. 2004). This mechanism might help solving the cusp core problem, because it naturally explains cores in a ΛCDM universe.

Like two other examples of dwarf spheroidal galaxies in the literature [Fornax (Sánchez-Salcedo, Reyes-Iturbide & Hernandez 2006; Goerdt et al. 2006) and Ursa Minor (Kleyna et al. 2003)], as well, this dwarf spheroidal seems to have at least very shallow if not cored underlying dark matter halo. The cusp-core transform mechanism described in this paper can help interpreting these observation within the prevailing ΛCDM paradigm, as having an initially cuspy (NFW) halo which has been transformed into a cored halo. Although the total number of galaxies taken into account was unavoidably small, our calculations demonstrate that should more data become available, our methods can serve as a powerful tool for estimating the value of γ. The most probable explanation for this observation is an primordial inner log density slope of about 1.0 which has been transformed into a harmonic core due to dynamical friction.

4.6 Acknowledgements

It is a pleasure to thank Ioannis Sideris for carefully reading the manuscript. For all N-body simulations we used PKDGRAV2 (Stadel 2001), a multistepping tree code developed by Joachim Stadel. All computations were made on the zBox2 supercomputer (www.zBox2.org) at the University of Zürich. Special thanks go to Doug Potter for bringing it to life.

5 The survival and disruption of CDM micro-haloes: implications for direct and indirect detection experiments[12]

5.1 Abstract

If the dark matter particle is a neutralino then the first structures to form are cuspy cold dark matter (CDM) haloes collapsing after redshifts $z \approx 100$ in the mass range $10^{-6} - 10^{-3}\,\mathrm{M}_\odot$. We carry out a detailed study of the survival of these micro-haloes in the Galaxy as they experience tidal encounters with stars, molecular clouds, and other dark matter substructures. We test the validity of analytic impulsive heating calculations using high resolution N-body simulations. A major limitation of analytic estimates is that mean energy inputs are compared to mean binding energies, instead of the actual mass lost from the system. This energy criterion leads to an overestimate of the stripped mass and underestimate of the disruption timescale since CDM haloes are strongly bound in their inner parts. We show that a significant fraction of material from CDM micro-haloes can be unbound by encounters with Galactic substructure and stars, however the cuspy central regions remain relatively intact. Furthermore, the micro-haloes near the solar radius are those which collapse significantly earlier than average and will suffer very little mass loss. Thus we expect a fraction of surviving bound micro-haloes, a smooth component with narrow features in phase space, which may be uncovered by direct detection experiments, as well as numerous surviving cuspy cores with proper motions of arc-minutes per year, which can be detected indirectly via their annihilation into gamma-rays.

5.2 Introduction

If dark matter is composed mainly of the lightest supersymmetric partner particle, the neutralino, the first self-gravitating structures in the universe are earth-mass haloes forming at high redshifts (Hofmann, Schwarz & Stöcker 2001; Diemand, Moore & Stadel 2005). As many as 10^{15} could be within our Galactic halo today. These abundant cold dark matter (CDM) micro-haloes have cuspy density profiles that can withstand the Galactic tidal field at the solar radius. The numbers of such haloes that lie within the vicinity of the

---

[12] This chapter has been published as Goerdt et al. (2007).

solar system depends on how many survive the complex merging history of early hierarchical structure formation. N-body simulations of CDM satellites indicate that tightly bound cusps are very stable against tidal stripping (Kazantzidis et al. 2004), and therefore dense micro-haloes accreting late onto more massive structures may survive relatively intact. The exact distribution of dark matter in the solar vicinity is important for direct and indirect dark matter detection experiments.

Substructures that survive the merging process will experience continuous perturbative encounters with stars, molecular clouds, and other dark matter subhaloes. As discussed in Diemand, Moore & Stadel (2005), we expect that these encounters lead to some mass loss but that the cusps of most micro-haloes remain intact. Recent studies by Zhao et al. (2005, 2007), Green & Goodwin (2007) and Berezinsky Dokuchaev & Eroshenko (2006) have raised the question whether these first haloes would be completely disrupted by close encounters with stars. Crossing the Galactic disc would also cause additional tidal heating. Moore et al. (2005) argued that the analytical impulse approximation and the semi-analytic models used in these studies may not fully describe the disruption of the high-density inner cores. Particle orbits deep in the cusp may remain adiabatically invariant to the perturbations and preserve the structure of the cusp. Only direct numerical simulations can describe these complex dynamical processes. In this paper, we use several sets of high resolution N-body simulations to test the validity of analytical heating models.

An important factor in the survival statistics of micro-haloes is how many survive similar-mass mergers during the build-up of the Galactic halo (Diemand, Kuhlen & Madau 2006). Even if only a few percent survive the hierarchical growth, many micro-haloes would still lie within one parsec from the Sun. Their dense cuspy cores would be sources of gamma-ray emission due to self-annihilation, which could be uniquely distinguished by their high proper motions on the sky of the order arc-minutes per year, assuming that the local dark matter density is $\rho(r_\odot) = 0.01 \mathrm{M}_\odot\,\mathrm{pc}^{-3}$ (Holmberg & Flynn 2000) and that micro-haloes obey a Maxwell-Boltzmann velocity distribution function set by the virial temperature of the Milky Way halo (for more details see Koushiappas 2006).

5.3 Heating by stars in the solar neighbourhood

There are various ways to define a virialized halo. The approach often used in cosmological simulations, which we adopt here, is that dark haloes virialize when their average density equals $\Delta = 200$ times the mean density of the universe, $\bar{\rho}(z) = 3\Omega_0 H_0^2 (1+z)^3/8\pi G$. Here H_0 is the Hubble constant, Ω_0 is the matter density parameter, and z is the redshift of virialization. Then the virial radius of the halo, defined by the relation $M_{\rm vir} \equiv \frac{4\pi}{3} R_{\rm vir}^3 \Delta \bar{\rho}(z)$, is

$$R_{\rm vir} = 0.31\,(1+z)^{-1} \left(\frac{M_{\rm vir}}{10^{-6}\,{\rm M}_\odot} \right)^{1/3} {\rm pc}, \tag{68}$$

for $\Omega_0 = 0.3$ and $H_0 = 70\,{\rm km\ s^{-1}\,Mpc^{-1}}$. The virial velocity is defined by the relation $V_{\rm vir}^2 \equiv GM_{\rm vir}/R_{\rm vir}$:

$$V_{\rm vir} = 12\,(1+z)^{1/2} \left(\frac{M_{\rm vir}}{10^{-6}\,{\rm M}_\odot} \right)^{1/3} {\rm cm\ s^{-1}}. \tag{69}$$

These parameters determine the binding energy of the haloes, which can be expressed using the half-mass radius of the system: $E_{\rm b} \approx 0.2GM_{\rm vir}/R_{1/2}$ (Spitzer 1987). Density profiles of dark matter haloes in cosmological simulations are often described by the NFW model with a concentration parameter, c. For $c < 10$, the radius containing half of the virial mass is approximately $R_{1/2} \approx (5c)^{-1/4}\,R_{\rm vir}$. High-redshift haloes have typically low concentrations, such that $R_{1/2} \approx 0.5R_{\rm vir}$. Therefore, the binding energy of first haloes is $E_{\rm b} \approx 0.4V_{\rm vir}^2$. As these small haloes merge into larger systems, two effects may modify their structure: tidal truncation by the host galaxy and tidal heating by massive, fast-moving perturbers (stars, molecular clouds, other dark matter substructures). In the vicinity of the Sun, the matter density is dominated by stars, which we assume to have the same mass $m_* = 0.7\,{\rm M}_\odot$, which is the mass of an average star in the solar neighbourhood. The stellar mass density is $m_* n_* \approx 0.1\,{\rm M}_\odot\,{\rm pc}^{-3}$ (Binney & Merrifield 1998), which is a half of the total density of the disc calculated from the Oort limit (Bahcall 1984). In order to remain gravitationally self-bound, the micro-haloes must have an average density above roughly $2m_* n_*$ (Binney & Tremaine 1987).

Fast encounters with massive perturbers increase the velocity dispersion of dark matter particles and reduce a halo's binding energy. A distant encounter at an impact parameter b with a relative velocity $V_{\rm rel}$ increases the energy per unit mass on the average by

$$\Delta E_1(b) \approx \frac{1}{2}\left(\frac{2Gm_*}{b^2\,V_{\rm rel}}\right)^2 \frac{2}{3}\left\langle r^2\right\rangle, \qquad (70)$$

where $\left\langle r^2\right\rangle \sim R_{1/2}^2$ is the ensemble average of the particle distance squared from the centre of the micro-halo.

At very small impact parameters, $b < b_1$, a single encounter would be sufficiently strong to unbind the whole halo: $\Delta E_1(b_1) = E_{\rm b}$. As we show later in section 5.5, a small central part always survives even such a strong perturbation, apart from direct collisions with $b = 0$. Nevertheless, it is instructive to define the disruptive encounter threshold, which is given by

$$b_1 = a_{\rm c}\left(\frac{Gm_* R_{\rm vir}}{V_{\rm rel}V_{\rm vir}}\right)^{1/2} \approx 0.2\,(1+z)^{-3/4}\ {\rm pc}, \qquad (71)$$

where $a_{\rm c} \approx 0.96\,(c/3)^{-1/8}$. Equation (70) is strictly valid only in the tidal approximation, $b \gg R_{\rm vir}$. An encounter at b_1 falls in that regime for redshifts $z < 50$, which is appropriate for our consideration of the micro-haloes.

The number of encounters over time t as a function of impact parameter is $dN_{\rm enc}(b) = n_* V_{\rm rel} t\, 2\pi b db$, where n_* is the number density of stars. We can obtain the cumulative effect of multiple non-disruptive encounters by integrating over the impact parameter:

$$\begin{aligned} \Delta E_{\rm tid} &= \int_{b_1}^{b_{\rm max}} \Delta E_1(b)\,\frac{dN_{\rm enc}}{db}\,db \\ &= 0.4 a_{\rm c}^4 \pi \frac{G^2 m_*^2 R_{\rm vir}^2 n_* t}{V_{\rm rel}}\left(\frac{1}{b_1^2} - \frac{1}{b_{\rm max}^2}\right). \qquad (72) \end{aligned}$$

The upper limit of integration is set by the condition that the encounter is impulsive, i.e. the duration of the encounter $b/V_{\rm rel}$ is shorter than the orbital time of particles in the halo, $R_{\rm vir}/V_{\rm vir}$. The maximum impact parameter is given by

$$\left(\frac{b_{\rm max}}{b_1}\right)^2 \approx a_{\rm c}^2 \frac{V_{\rm rel}^3\,R_{\rm vir}}{Gm_* V_{\rm vir}} \gg 1. \qquad (73)$$

The ratio of the tidal heating energy in non-disruptive encounters to the binding energy is

$$\frac{\Delta E_{\rm tid}}{E_{\rm b}} = a_{\rm c}^2 \pi \frac{Gm_* n_* t R_{\rm vir}}{V_{\rm vir}}. \qquad (74)$$

We can also calculate the effect of disruptive encounters, with $b < b_1$. The number of such encounters is simply

$$N_{\rm enc}(< b_1) = \pi b_1^2 n_* V_{\rm rel} t = a_{\rm c}^2 \pi \frac{G m_* n_* t R_{\rm vir}}{V_{\rm vir}}. \tag{75}$$

This number is the same as equation (74) meaning that the cumulative effect of disruptive encounters is the same as that of non-disruptive encounters. The total disruption probability, $N_{\rm tot}$, is then twice that given by equation (74).

To calculate this disruption probability, we note that while stars in the solar neighbourhood move on approximately circular orbits around the Galactic centre, small dark matter haloes would be moving on isotropic orbits inclined with respect to the Galactic disc. Their expected vertical velocity is $V_z \approx 200$ km s^{-1}. The crossing time of the disc with a scale height of $H = 0.2$ kpc is $2H/V_z = 2 \times 10^6$ yr. In the solar neighbourhood, haloes would cross the disc every 10^8 yr and have about 100 crossings in the Hubble time. The total amount of time the haloes would spend in the region of high stellar density $m_* n_*$ is then $t_d \sim 2 \times 10^8$ yr. The total disruption probability is

$$N_{\rm tot} = 2\, N_{\rm enc}(< b_1) = \left(\frac{1+z}{131}\right)^{-3/2} \left(\frac{m_* n_*}{0.1\,{\rm M_\odot\,pc^{-3}}}\right) \left(\frac{t_d}{2 \times 10^8\,{\rm yr}}\right). \tag{76}$$

Therefore, the haloes virialized after redshift $z = 130$ should suffer significant mass loss by passing stars in the solar neighbourhood. Due to biased halo formation typical subhaloes in the solar neighbourhood come from 2σ fluctuations (Diemand, Madau & Moore 2005), i.e. they virialize at half the expansion factor [or twice the (z + 1) value] than typical haloes of the same mass in the field (i.e. 1σ peaks). A formation time of z = 130 corresponds to about a 3σ peak. Such early structure formation is not uncommon in dense environments, for example the small, over dense region simulated in Diemand, Kuhlen & Madau (2006) already contains 845 micro-haloes at z = 130. A fraction of about 20% of the local mass comes from peaks above 3σ (Diemand, Madau & Moore 2005), implying that approximately 20% of the local subhalo population should therefore not suffer significant mass loss.

5.4 Heating by dark matter substructure

Virialized, self-gravitating subhaloes within larger haloes (the substructure) will also kinematically heat and disrupt their small cousins (c.f. Boily et al.

2004). N-body simulations (Diemand, Moore & Stadel 2004) show that the number of subhaloes with masses above M within a host of mass $M_{\rm host}$ scales as

$$N_{\rm sub}(> M/M_{\rm host}) \approx \left(\frac{M}{10^{-2}\, M_{\rm host}}\right)^{-1}. \tag{77}$$

Since stars occupy only a small fraction of the volume of their host haloes, it is important to consider if the tidal heating by dark matter subhaloes can disrupt a significant fraction of micro-haloes.

The analysis of section 5.3 can be generalised for perturbers with a range of masses, $M_{\rm vir} < M < 10^{-2}\, M_{\rm host}$. Let $f \equiv M/M_{\rm host}$ be the dimensionless subhalo mass. The threshold impact parameter, at which a single encounter with subhalo f is disruptive, is $b_1^2(f) \approx f V_{\rm host} R_{\rm host} R_{\rm vir}/V_{\rm vir}$, where we assumed the relative velocity to be the virial velocity of the host halo, $V_{\rm rel} \approx V_{\rm host}$. However, for most subhaloes this impact parameter is smaller than their size, $R_{\rm sub} \approx r[M_{\rm sub}/3M_{\rm host}(r)]^{1/3}$, which is determined by tidal truncation at distance r from the centre of the host halo. Tidal approximation applies only at $b > b_{\rm min} = R_{\rm sub}$. Therefore, most encounters will be non-disruptive.

The cumulative heating by multiple non-disruptive encounters with subhaloes of mass $M_{\rm sub} = f M_{\rm host}$ is [see equation (72)]:

$$\frac{\Delta E_{\rm tid}(f)}{E_{\rm b}} = \frac{\pi G^2 M_{\rm sub}^2 R_{\rm vir}^2 t}{V_{\rm host} V_{\rm vir}^2 b_{\rm min}^2} \frac{dn_{\rm sub}}{df}, \tag{78}$$

where $\frac{dn_{\rm sub}}{df}$ is the number density of subhaloes f. Taking an NFW model for the smooth component of the Galactic halo and restricting our analysis to the inner part of the halo, $r \lesssim r_s \approx 20$ kpc, we find the subhalo's truncation radius $R_{\rm sub} \approx r_s (fr/r_s)^{1/3}$. The density of subhaloes, assuming they have not been completely disrupted, is

$$\frac{dn_{\rm sub}}{df} \approx \frac{10^{-2} f^{-2}}{4\pi g(c) r_{\rm s}^2 r}, \tag{79}$$

where $g(c) \equiv \ln(1+c) - c/(1+c) \approx 1.6$ for a concentration parameter $c = 12$ (Klypin, Zhao & Sommerville 2002). For the Galaxy, a Hubble time corresponds to $t \sim 5R_{\rm host}/V_{\rm host}$.

Thus for the inner halo,

$$\frac{\Delta E_{\rm tid}(f)}{E_{\rm b}} = \frac{5 \times 10^{-2} c^5}{4 g(c)} \left(\frac{t V_{\rm host}}{5 R_{\rm host}}\right) \frac{R_{\rm vir}^2 V_{\rm host}^2}{R_{\rm host}^2 V_{\rm vir}^2} f^{-2/3} \left(\frac{r}{r_{\rm s}}\right)^{-5/3}. \tag{80}$$

Integrating over all subhaloes, $f < 0.01$, we find

$$\frac{\Delta E_{\rm tid}}{E_{\rm b}} \approx 0.063 \left(\frac{r}{r_{\rm s}}\right)^{-5/3} . \qquad (81)$$

Thus, micro-haloes may be disrupted by repeated encounters with more massive haloes within $r \lesssim 0.2 r_{\rm s} \approx 4$ kpc from the centre of the Galaxy.

5.5 Numerical tests of the impulsive approximation

In this section we test the response of a CDM micro-halo to repeated impulsive encounters using N-body calculations in order to test the validity of the impulse approximation, and to study in detail how the internal structure of the micro-haloes evolve with time.

The initial state for the micro-halo is an equilibrium profile with the same structural parameters as found by Diemand, Moore & Stadel (2005) at $z = 26$, the epoch at which such structures are typically accreted into larger mass systems. This halo obeys a cuspy density profile, the general α, β, γ law (Hernquist 1990):

$$\rho(r) = \frac{\rho_0}{\left(\frac{r}{r_{\rm s}}\right)^{\gamma} \left[1 + \left(\frac{r}{r_{\rm s}}\right)^{\alpha}\right]^{\frac{\beta-\gamma}{\alpha}}} \qquad (r \leq R_{\rm micro}), \qquad (82)$$

with $\alpha = 1.0$, $\beta = 3.0$ and $\gamma = 1.2$. The mass of the halo is $M_{\rm micro} = 10^{-6}\,{\rm M}_\odot$ within the $z = 26$ virial radius $R_{\rm micro} = 0.01$ pc. The concentration parameter is low, $R_{\rm micro}/r_{\rm s} = 1.6$, typical of micro-haloes in the field at $z = 26$. Some experiments we repeated with micro-haloes having concentrations of 3.2. The typical local subhalo forms earlier (by about a factor of two in redshift, see Diemand, Madau & Moore 2005) than the average micro-halo in the field. Therefore the typical local subhalo might be twice as concentrated and more robust against mass loss. However, to be conservative we use the low concentration of 1.6 throughout this paper unless stated otherwise. For numerical stability of the profile, we make a realization of this halo extending to approximately $4\,R_{\rm micro}$ using the techniques of Kazantzidis Magorrian & Moore (2004). At $r > R_{\rm micro}$, the density profile falls off exponentially as $\exp(-r/r_{\rm decay})$, with $r_{\rm decay} = 0.3\,R_{\rm micro}$. The total mass of the system is therefore $1.81\,M_{\rm micro}$. We use 10^6 particles of equal mass, $m_{\rm p} = 1.81 \times 10^{-12}{\rm M}_\odot$. The force calculations have a softening length of $0.005\,R_{\rm micro}$.

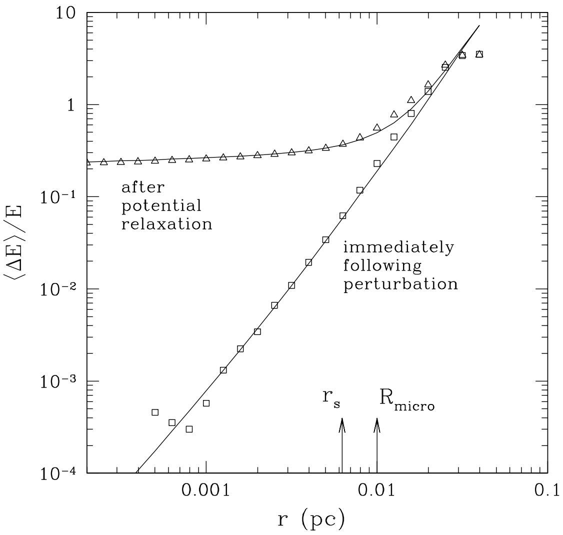

Figure 29: Energy change per particle as a function of radius immediately following the perturbation (*squares*) and after potential relaxation (*triangles*), for the encounter with $b = 0.02$ pc, together with the analytical predictions (*solid line*) according to equation (83).

We then subject the equilibrium micro-halo to a series of impulsive encounters with a star of mass $m_* = 0.7\,\mathrm{M}_\odot$, the mean mass per star in the disc of the Galaxy. First we run six simulations, which differ in the minimal distance from the star to the centre of the micro-halo. For these six simulations the impact parameters are $b = 0.005, 0.01, 0.02, 0.05, 0.1, 1\,\mathrm{pc}$. We have to keep in mind that the smaller an impact parameter the more damage it will do but the less likely it is to happen and vice versa. We choose this set of impact parameters because an impact at 1 pc hardly does any damage (c.f. Fig. 32) and an impact at 0.005 pc hardly ever occurs (in our Monte Carlo simulations at the end of this section it occurs on average once during a Hubble time). In all runs the star moves with the relative velocity $V_{\mathrm{rel}} = 300$ km s^{-1}. The initial separation of the star and the halo along the direction of motion is three times the impact parameter or three times the micro-halo radius of the halo, whichever is the greater. After the star reaches the point of closest approach, we let it move away the same distance from the halo. Then we remove the star and let the system evolve in isolation for 3×10^8 yr, which corresponds to 20 crossing times of the halo. Similar experiments date back to e. g. Aguilar & White (1985).

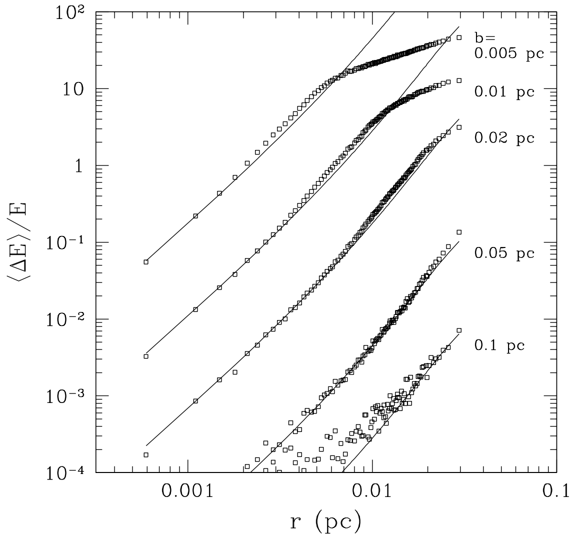

Figure 30: Energy change per particle as a function of radius immediately following the perturbation, for encounters with different impact parameters b.

Each encounter increases the internal energy of the micro-halo. Following the perturbation, the system undergoes a series of virial oscillations (contraction and expansion) until the potential relaxes into a new equilibrium configuration (Gnedin & Ostriker 1999). Depending on the strength of the perturbation, this potential relaxation takes between 10 and 20 crossing times of the halo. The final configuration has a lower binding energy and some particles may escape the system entirely.

Fig. 29 shows the energy change per particle for a flyby at $b = 0.02$ pc at two different times: directly following the encounter and after the potential relaxation. The duration of the encounter, $\tau = 2b/V_{\rm vel} \approx 130$ yr, is much shorter than the dynamical (crossing) time of the particles in the micro-halo, $t_{\rm dyn} \approx 1.5 \times 10^7$ yr. Therefore, we expect that the tidal heating can be calculated in the impulsive approximation [c.f. equation (70)]. For ensemble-average of stars with initial energy E, the energy per unit mass increases by the amount

$$\langle \Delta E \rangle = \frac{4}{3}\left(\frac{G m_*}{b^2\, V_{\rm rel}}\right)^2 r^2. \tag{83}$$

This prediction is plotted next to the numerical result (squares) in Fig. 29 and agrees with it very well.

Subsequent potential relaxation reduces the depth of the potential well of the system, leading to another effective energy change. (Gnedin & Ostriker 1999) found that this additional energy change can be approximated as a constant fraction of the initial potential, $\Phi_{\rm i}$:

$$\Delta E_{\rm pot}(r) = c\,[-\Phi_{\rm i}(r)], \tag{84}$$

where the constant c is such that the sum of $\Delta E_{\rm pot}(r)$ over all particles is twice the initial energy change of the system, $\Delta E_1(b)$, as required by the virial theorem. The final energy difference is $\langle \Delta E \rangle + \Delta E_{\rm pot}$. This prediction is plotted next to the numerical result (triangles) in Fig. 29 and again provides a very good fit.

Fig. 30 shows the energy changes immediately following the encounters at different impact parameters, b. The analytical formula (83) provides a good description of the numerical results, except in cases of extremely strong perturbations when the energy changes by more than 100%, $\langle \Delta E \rangle > |E|$. Fig. 31 shows the final energy redistribution after potential relaxation, for encounters

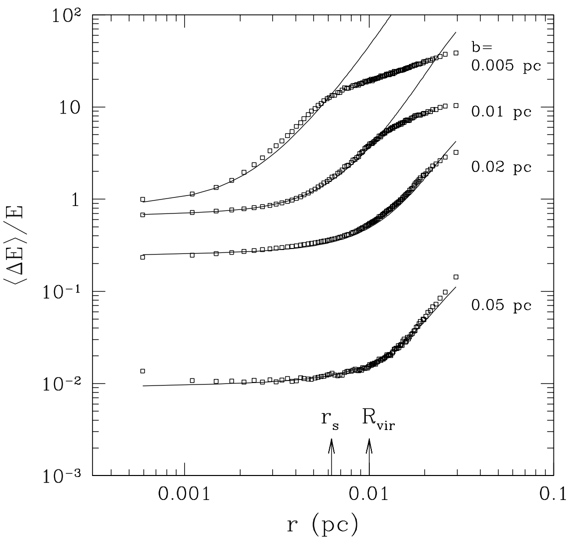

Figure 31: Energy change per particle as a function of radius after potential relaxation, for encounters with different impact parameters b.

with different impact parameters, b. Equations (83) and (84) describe the effect very accurately.

The change of the micro-halo potential leads to the change of the density profile. Particles that gain enough energy to escape the system form unbound tidal tails. The final density profiles for the encounters with different impact parameters are shown in Fig. 32.

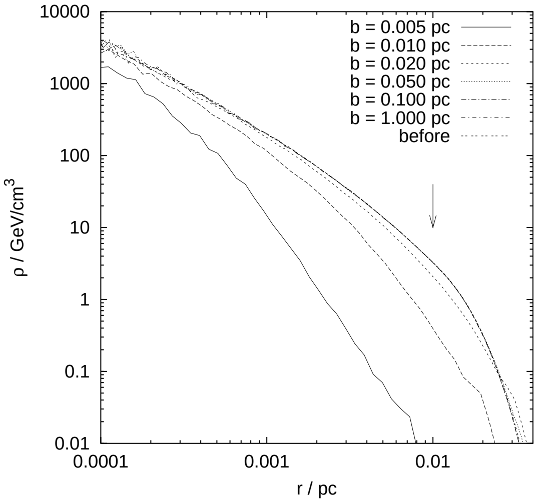

Figure 32: Density profile of the micro-halo in a new equilibrium, after encounters with different impact parameters, b. The arrow indicates the micro-halo radius.

The amount of mass stripped from the halo depends on the definition of the bound mass. The density of the outer halo profile extends as r^{-3} beyond the nominal micro-halo radius, and all of the particles are initially bound. We use two practical definitions. (i) We have defined an effective maximum radius, $R_{\rm max} \equiv 4R_{\rm micro}$, beyond which all particles are assumed to be lost from the micro-halo. In practice, this radius can be set by the external tidal field. (ii) We have also defined an effective tidal potential at that radius, $\Phi_{\rm t} \equiv \Phi(R_{\rm max})$. We use this tidal potential to construct another definition of unbound particles, as those with $E > \Phi_{\rm t}$. After the potential relaxation, the new potential Φ is used to define $\Phi_{\rm t}$ at the same fixed radius $R_{\rm max}$.

Fig. 33 shows the change of the total energy of the system immediately following the encounter, for all particles within $R_{\rm max}$. It is well described by equation (70), which is plotted as a solid line. Since the density profile of the system continues beyond the nominal micro-halo radius, the average radius

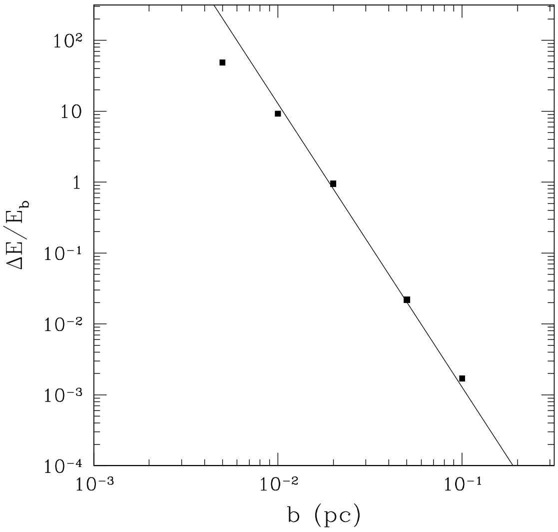

Figure 33: Total energy change of all particles immediately following the perturbation, as a function of impact parameter (*filled squares*) and the analytical prediction in the impulse approximation (*solid line*).

for all particles is $\langle r^2 \rangle = 1.63\, R_{\rm micro}^2$. We used this value for the plotted prediction.

Fig. 34 shows the mass loss as a function of impact parameter, using the two definitions based on the position and energy criterion, respectively. For large impact parameters (weak perturbations), the position criterion indicates systematically lower mass loss than the energy criterion. Therefore, some particles within $R_{\rm max}$ may be unbound at the end of the simulation. In the strong perturbation regime, both criteria give similar results.

While the total energy change of the system can be computed with sufficient accuracy using the impulsive approximation, the amount of mass lost cannot. Using our numerical simulations, we seek to establish a practical relation between $\Delta M/M$ and $\Delta E/E_{\rm b}$. We find that the following equation provides a good fit to the numerical results:

$$\frac{\Delta M}{M} = \frac{1}{1 + 2.1\left(\frac{\Delta E}{E_{\rm b}}\right)^{-1}}. \tag{85}$$

For weak perturbations the mass loss scales as the energy change, $\Delta M/M \approx$

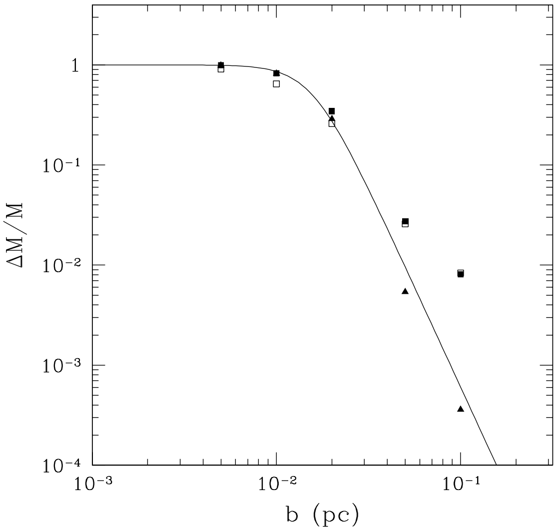

Figure 34: Mass loss of the halo as a function of the impact parameter b, determined using either the energy criterion, $E > \Phi_\mathrm{t}$ (*open squares*: immediately following the perturbation, *filled squares*: after the potential relaxation) or the position criterion, $r > R_\mathrm{max}$, after the potential relaxation (*triangles*).

$0.5\Delta E/E_\mathrm{b}$. For very strong encounters, the mass loss asymptotically approaches unity. Note however, that even for very small impact parameters, when $\Delta E/E_\mathrm{b} \gg 1$, a small fraction of the mass always remains bound, $\approx 2(\Delta E/E_\mathrm{b})^{-1}$.

A note on notation. Strictly speaking, the tidal approximation which was used to derive equation (70) is only valid for $b \gg R_\mathrm{micro}$. At smaller impact parameters the energy change does not scale as b^{-4}, but it can be calculated in the opposite asymptotic limit (e.g. Moore 1993; Carr & Sakellariadou 1999; Green & Goodwin 2007). We take an alternative approach by parametrising the mass loss in our numerical simulations [equation (85)] based on the formal extrapolation of equation (70) to all values of b.

As Fig. 32 shows, most of the mass remaining bound to the micro-halo after strong perturbations is concentrated near its centre. It is therefore interesting to calculate the fraction of lost mass that was initially contained within the power law density cusp, at $r < r_\mathrm{s}$. Fig. 35 shows that this fraction scales as $\Delta M_\mathrm{cusp}/M_\mathrm{cusp} \approx (1 + 5(\Delta E/E_\mathrm{b})^{-1})^{-1}$. We also performed another set of simulations, by repeatedly perturbing the micro-halo with the same star,

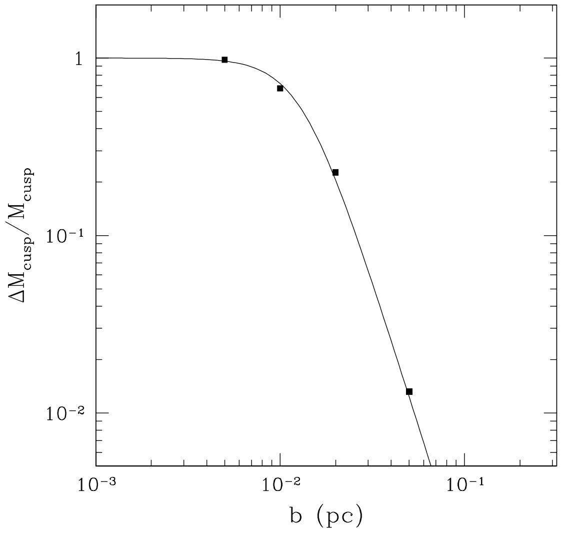

Figure 35: Mass lost inside the scale radius, $r < r_\mathrm{s}$, after the potential relaxation, as a function of impact parameter.

with the same relative velocity and at the same impact parameter $b = 0.02$ pc. After the halo has relaxed following the first encounter, we move the centre of mass of the remaining halo to the origin of the coordinate system and let a star pass by in exactly the same way and again let it relax, and then repeat the encounter a total of ten times.

The density profile of the micro-halo after n encounters is shown in Fig. 36. Every encounter heats the system and strips some mass, but each successive encounter is less and less effective. Fig. 37 shows the cumulative mass loss after each such encounter. It can be described by the following function:

$$\frac{\Delta M}{M}(n) = 1 - \exp\left(An^B\right), \tag{86}$$

with A = -0.34 and B = 0.87 for c = 1.6 and A = -0.23 and B = 0.81 for c = 3.2, which are also shown in Fig. 37.

We fitted each of the eleven density profiles, which are shown in Fig. 36, as well as the corresponding eleven density profiles for the halo with c = 3.2, which are not shown, with equation (82). To make the fits we used the Levenberg-Marquardt method (Marquardt 1963) in log-log space keeping γ fixed at 1.2. The variation of $\alpha, \beta, r_\mathrm{s}$ and ρ_0 from encounter to encounter is

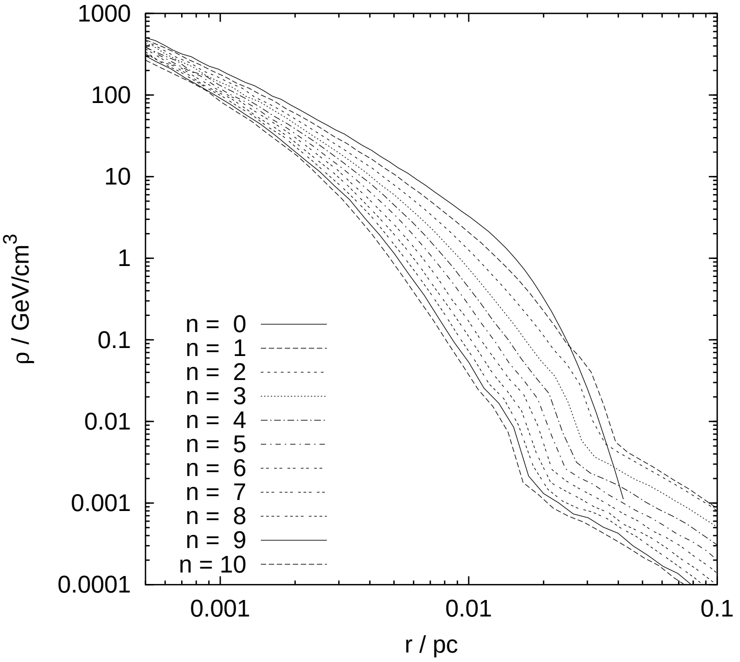

Figure 36: Density profile of the micro-halo after successive encounters with a star with the same mass and orbital parameters ($b = 0.02$ pc), marked by the encounter number n.

as follows: α increases from 1.0 to 1.5, β increases monotonically from 3.0 to 7.0, $\mathrm{r_s}$ stays constant around 7.0 milli-pc for the c = 1.6 halo and around 4.0 milli-pc for the c = 3.2 halo and finally ρ_0 oscillates around 20 GeV/cm^3 for c = 1.6 and decreases from 100 down to 50 GeV/cm^3 in case of the other halo. The resulting profiles could now be used to calculate the net flux coming from neutralino annihilation (e.g. Lake 1990; Koushiappas 2006) via:

$$F = k \int_{r_{min}}^{\infty} 4\pi r^2 \rho(r)^2 \mathrm{d}r \tag{87}$$

We have summed up the dependence of the flux on neutralino mass and interaction cross section in the constant k. The lower bound r_{min} is defined as the central region of the micro halo, in which the neutralinos already annihilated each other. The required number density for this to happen can be estimated with the help of

$$t_{\mathrm{h}} = \frac{1}{n\sigma v} \tag{88}$$

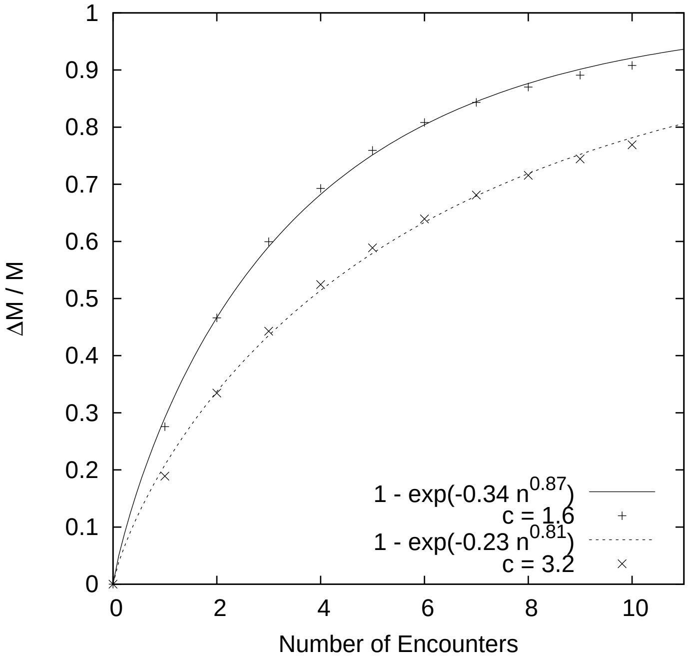

Figure 37: Cumulative mass loss of different micro-haloes after a number of identical encounters with $b = 0.02$ pc.

where $t_\mathrm{h} \approx 13$ Gyrs is the Hubble time, $\sigma v \approx 10^{-30}$ cm^{3}s^{-1} is a typical cross section and n is the number density of neutralinos. For more details see Calcáneo-Roldán & Moore (2000). The minimum radius can now be computed from comparing this minimum number density with the density profile in Fig. 36. Assuming a neutralino mass of 100 GeV and deploying the above mentioned density profile, r_min comes out to be 1.6×10^{-14} pc. Fig. 38 shows then the resulting annihilation flux. It is more or less independent of the assumed neutralino mass, because this mass only goes into the calculation of r_min, which is a tiny value anyway, and not directly into the computation of the flux.

In order to investigate the sensitivity of tidal heating to the structure of the micro-halo, we have run additional simulations with different initial profiles. We use the cuspy profile given by equation (82) and vary the slope $\gamma = 0$, 0.5, 1, and 1.5, in addition to our fiducial value, $\gamma = 1.2$. This suite of simulations is carried out using a fixed impact parameter, $b = 0.02$ pc, and other parameters as in the fiducial run. Our calculations are similar to earlier studies of impulsive heating e.g. Aguilar & White (1986), who studied the

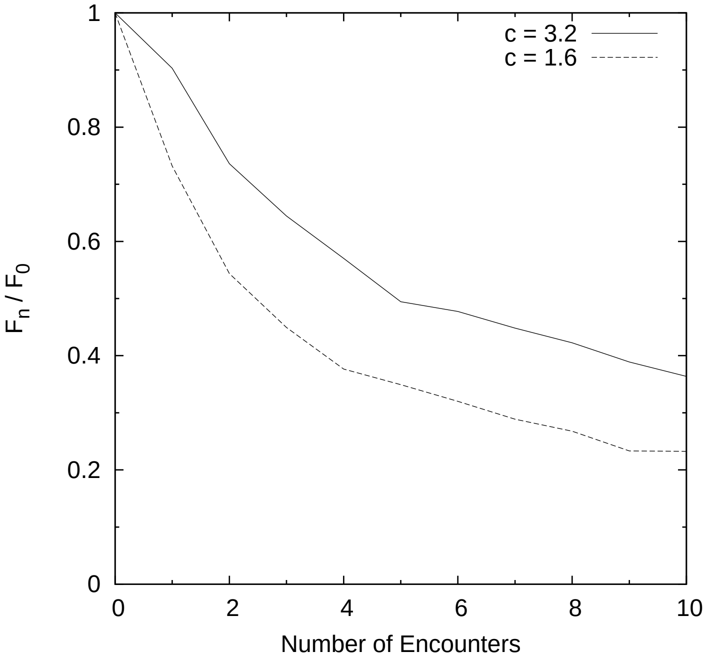

Figure 38: The relative flux of annihilation products from different micro-haloes after a given number of encounters ($b = 0.02\,\mathrm{pc}$). The typical mass loss from a halo would lead to a decrease in flux of between a factor of two or three.

structural change in systems with de Vaulouleur density profiles.

Fig. 39 shows that up to 30% more mass is lost from the cored halo ($\gamma = 0$) compared to the cuspy haloes ($\gamma > 1$). The effect is even stronger for the fraction of mass removed from within the scale radius, r_s: 2.5 times more material is lost from the cored halo. The strongly-bound material within the cusp is more stable against tidal disruption than that in cored profiles, which have been typically considered in previous studies of tidal heating.

In Fig. 36 we show the mass loss of the micro-halo for ten successive encounters with exactly the same impact parameter. This is unlike the situation in our Galaxy where micro-haloes orbit the disc for 10 Gyrs near the solar radius. It spends about 0.1 Gyr moving through the disc encountering stars at a relative velocity of approximately $300\,\mathrm{km/s}$ and a range of impact parameters. In order to model this behaviour more precisely, we use a Monte-Carlo method, which estimates the total amount of mass-loss it would suffer. We draw encounter impact parameters from a random distribution and calculate

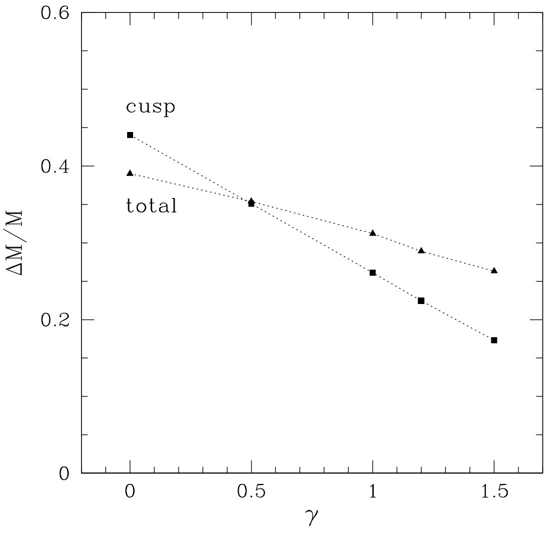

Figure 39: Total mass loss from the micro-halo as a function of the inner density slope, γ, determined using the the position criterion, $r > R_{\mathrm{max}}$, after the potential relaxation (*triangles*), as well as the fraction of mass lost from inside the scale radius, $r < r_{\mathrm{s}}$ (*squares*).

at each time the stripped mass. The random distribution of impact parameters is defined by the assumption that space is homogeneously and randomly filled with stars. Because we are only interested in the radial distance to a certain star in a 2D projection, the probability density distribution function of impact parameters comes out to be a linear raising function, being 0 for $b = 0$. After each encounter, the density profile of the micro-halo changes self-consistently according to the results found earlier with the N-body simulations. The mass loss due to the first encounter can easily be calculated using equation 85. From the second encounter onwards, the halo density profile changes and it is harder to strip during subsequent encounters as we have seen in Fig. 37. The mass M_{a}, the halo has after the ath encounter, determines the reduction of the mass, which is stripped in the $a + 1$st encounter. This is unfortunately not a variable of equation (86). This is a function of n only. So we calculate at the beginning of each encounter a “virtual encounter number” n, which is basically the inverse of equation (86):

$$n = \sqrt[B]{\frac{\log_{\mathrm{e}} M_{\mathrm{a}}}{A}}, \tag{89}$$

with A depending on the respective concentration [see equation (86)]. For a given M_{a} it computes the corresponding number of “standard encounters” with the impact parameter $\mathrm{b} = 0.02\,\mathrm{pc}$ from figure 37. Now we can calculate the mass $M_{\mathrm{a+1}}$ after the $a + 1$st encounter. This must be a deviation from equation (85) with some weighting function $w(n, M_{\mathrm{a}})$:

$$M_{\mathrm{a+1}} = M_{\mathrm{a}} \left[1 - \frac{w(n, M_{\mathrm{a}})}{1 + 2.1 \left(\frac{\Delta E}{E_{\mathrm{b}}} \right)^{-1}} \right], \tag{90}$$

This weighting function is the fraction of mass, which is stripped in the $n +$ 1st standard encounter divided by the fraction of mass stripped in the first standard encounter:

$$w(n, M_{\mathrm{a}}) = \frac{\frac{\Delta M}{M}(n+1) - \frac{\Delta M}{M}(n)}{\frac{\Delta M}{M}(1) \left(1 - \frac{\Delta M}{M}(n)\right)} \tag{91}$$

The $\frac{\Delta M}{M}(n)$ can be calculated according to equation (86). This weighting function reproduces the results from Fig. 37. Keeping in mind that $\left[1 - \frac{\Delta M}{M}(n)\right] = M_{\mathrm{a}}$, equation (90) reduces to:

$$M_{\mathrm{a+1}} = M_{\mathrm{a}} - \frac{M_{\mathrm{a}} - \exp\left[A(n+1)^B\right]}{\frac{\Delta M}{M}(1) \left[1 + 2.1 \left(\frac{\Delta E}{E_{\mathrm{b}}} \right)^{-1} \right]} \tag{92}$$

We use this equation recursively for each encounter and then repeat the calculation to obtain the probability distribution of final masses in Fig. 40. The central density (at our softening length) of a perturbed halo decreases only by a factor of about 2 (see Fig. 36), whilst the total mass decreases by an average of 90% (see Fig. 37).

5.6 Conclusions

We have studied the disruption of dark matter micro-haloes by stars and other substructures using both analytical impulse approximation and self-consistent N-body simulations. The analytic calculations presented here are

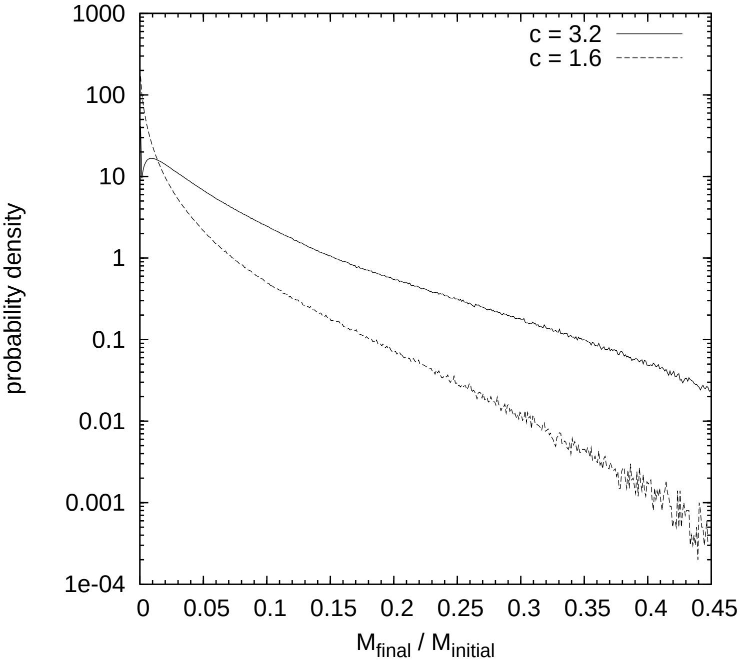

Figure 40: Probability density distribution function of the final masses of different haloes

quite similar to those of Green & Goodwin (2006) and we come to similar conclusions. Our calculations differed in that we used more realistic cuspy n-body models and we studied how the internal structure of these systems evolve due to perturbations. See also Angus & Zhao (2007) for an independent and complementary study. Earlier studies e.g. Aguilar & White (1986), also studied cuspy systems and found similar robustness to tidal heating in the central regions as we find. However our resolution allows us to study the response of CDM haloes deep within their central regions.

- The impulse approximation predicts that those micro-haloes in the solar vicinity which formed after z = 130 (about 80% of the local micro-halo population) should lose most of their mass due to close encounters with disc stars.

- Numerical simulations of individual encounters demonstrate that the usual condition of disruptive heating used in analytical studies, $\Delta E = E_{\rm b}$, does not lead to complete dissolution of haloes with cuspy density profiles. For the inner logarithmic slope $\gamma = 1.2$, on average only 30%

of the mass is lost from the system for this energy change. The relation between the fractional mass loss and the energy input in the tidal approximation is given by equation (85): $\Delta M/M \approx (1+2(\Delta E/E_{\rm b})^{-1})^{-1}$.

- The change of particle energies, after the system settles into a new virial equilibrium following the tidal encounter, is described accurately by the extension of the impulse approximation accounting for virial oscillations. An apparent resistance to tidal heating of the material deep in the cusp is due to the high binding energy inside the cusp.
- Repeated tidal encounters lead to diminishing mass loss from the same micro-halo. After 10 identical encounters at impact parameter $b = 2R_{\rm vir}$, 10% of the halo still remains self-bound even though $\Delta E = 5E_{\rm b}$.

Near the solar radius within the Galaxy most of the mass of the micro-haloes is tidally removed. This material forms cold streams in phase space providing a unique signal for direct detection experiments. The dense cuspy cores of these haloes survive reasonably intact, although the mass loss leads to a reduction in annihilation products of about a factor of only two to three. These cores could be distinguished by their high proper motions on the sky of the order arc-minutes per year.

Acknowledgements

For all N-body simulations we used PKDGRAV2 (Stadel 2001), a multistepping tree code developed by Joachim Stadel. All computations were made on the zBox supercomputer (www.zBox1.org) at the University of Zürich. OYG acknowledges support from NASA ATP grant NNG04GK68G.

6 The formation of ultracompact dwarf galaxies and nucleated dwarf galaxies

6.1 Abstract

Ultra compact dwarf galaxies (UCDs) have similar properties as massive globular clusters or the nuclei of nucleated galaxies. Recent observations of a high dark matter content and their steep spatial distribution within groups and clusters give us new clues as to their origins. We compare two formation mechanisms: the merging of globular clusters in the centre of a dark matter halo, or the massively stripped remnant of a nucleated galaxy. Both models produce density profiles as well as the half light radii that can fit the observational constraints very well. However, we show that the first scenario produces UCDs that are underluminous and contain no dark matter - the sinking process ejects most of the dark matter particles from the halo centre. Stripped nuclei give a more promising explanation, especially if the nuclei form via the sinking of gas, funneled down inner galactic bars, since this process enhances the central dark matter content. Even when the entire disk is stripped away, the nucleus remains and can be dark matter dominated. The total disruption of the galaxy beyond the nuclei only occurs on certain orbits and depends on the amount of dissipation during nuclei formation. By comparing the total disruption of CDM subhaloes in a cluster potential we show that this model also leads to the observed spatial distribution of UCDs which can be tested in more detail with larger data sets.

6.2 Introduction

A new type of galaxies has recently been discovered: the ultra-compact dwarf galaxies (UCDs) (Hilker et al. 1999). Different possible origins have been proposed (Evstigneeva, Gregg & Drinkwater 2005): (a) They are simply very big and luminous globular clusters, (b) They are nucleated dwarf galaxies, (c) They are the resulting objects of the coalescence of several globular clusters.

Fellhauer and Kroupa (2002) dedicated some work on the third creation scenario and discovered with the help of N-body simulations, that the object which results from merging several globular clusters together has the same appearance as an UCD. They argued, that a so-called supercluster, an accumulation of up to fifty globular clusters, might orbit a galaxy. In their simulations, they distributed globular clusters in such a way, so to construct such a supercluster. Then they added an artificial galactic potential as well as artificial dynamical friction so that the supercluster orbits the galaxy on fairly elliptical trajectories with distances around 20 kpc. Within the supercluster the globular clusters merge due to collisions, which occur while they orbit each other. The resulting object looked indeed like an UCD.

Inspired by their work and we attempt to simulate the creation of a UCD, deploying their scenario. Our idea is to combine it with the cold dark matter paradigm: Globular clusters form in dark matter haloes, which contain no other baryonic matter. We assume that the halos have masses comparable to Fornax, and allow the globular clusters orbit around their centre. Due to the dynamical friction, the globular clusters would be acted on, by the dark matter particles, they would spiral in towards the centre of the halo.

We run collisionless N-body simulations to show that the object resulting from the coalescence of the globular clusters reaching the centre of the halo looks like an UCD. The resulting surface brightness profile is similar in shape and the half light radius is comparable with observations. Unfortunately, this method has two major drawbacks, which rule out this scenario as we will show later: The first problem is the observed (Haşegan et al. 2005) high M/L ratio of an UCD. Such high values can never be reached by using this mechanism, because most of the dark matter particles are expelled from the very centre (El-Zant, Shlosmann & Hoffman 2001; Merritt et al. 2004). The second problem is the total luminosity of an UCD. You can hardly ever find a dark matter halo with a sufficient number of globular clusters in it to produce sufficient bright objects (Sharina, Puzia, & Makarov 1996). Further-on we come back to a different possible scenario, namely that UCDs could be remnants of stripped disk galaxies (Kazantzidis, Moore, Mayer 2003). Parts of this scenario have been discussed in Bekki et al. (2001, 2003). They perform numerical simulations on the dynamical evolution of nucleated dwarf galaxies orbiting NGC 1399 as well as the Fornax galaxy cluster and suffering from their strong tidal gravitational field. Adopting a plausible scaling relation for dwarf galaxies, they find that the outer stellar components of a nucleated dwarf are totally removed in both cases. This is due to them being tidally stripped over the course of several passages past the central region of their host. The nucleus, however, manages to survive. They also find that the size and luminosity of the remnant are similar to those observed for ultra compact dwarf galaxies, if the simulated precursor nucleated dwarf has a mass of $\sim 10^8$ $\mathrm{M}_\odot$. Their results suggest that ultra compact dwarf galaxies could have previously been more luminous dwarf spheroidal or elliptical galaxies with rather compact nuclei. Testing this scenario using SPH simulations suggests that there is an excellent agreement with observational constraints.

The setup of the merging simulations, their initial conditions and the properties of the merger objects are explained in section two. A more general merging model is discussed there, too. The galaxy threshing approach is presented in section three and the conclusions are drawn in section four.

6.3 The merging simulations

The N-body code we used, is PKDGRAV2, a multi stepping parallel tree code, developed by Joachim Stadel (Stadel 2001). For our simulations we create an NFW (Navarro, Frenk & White 1996) halo, deploying the techniques developed by Kazantzidis, Magorrian & Moore (2004), which has the following density profile:

$$\rho(r) = \frac{\rho_0}{r/r_\mathrm{s}\left[1 + (r/r_\mathrm{s})\right]^2}. \tag{93}$$

In our case $\rho_0 = 9228\,\mathrm{GeV/cm^3}$ and $r_\mathrm{s} = 1.5\,\mathrm{kpc}$. The halo has a virial mass of $1.5 \times 10^9\,\mathrm{M}_\odot$. The concentration parameter is 20. We use a three shell model (Zemp 2006), so it has 10^5 particles for the innermost sphere with 100 pc radius, 10^5 particles for the shell between 100 and 500 pc and 10^5 particles for the rest of the halo. The softening lengths for these shells are 1, 10 and 100 pc respectively. The ten globular clusters we use, consist of 10^5 particles, which are distributed according to the King (King 1966; Michie 1963; Michie & Bodenheimer 1963) model

$$\rho(\Psi) = \rho_1 \exp\left(\frac{\Psi}{\sigma^2}\right) \mathrm{erf}\left(\frac{\sqrt{\Psi}}{\sigma}\right) - \rho_1 \sqrt{\frac{4\Psi}{\pi\sigma^2}} \left(1 + \frac{2\Psi}{3\sigma^2}\right) \tag{94}$$

with a W_0 parameter of 6 and a total mass of $4.2 \times 10^5\,\mathrm{M}_\odot$. These ten globular clusters have central velocity dispersions of 11 km/s and absolute magnitudes of -8.5, assuming a mass to light ratio of 2. We use 1 pc as softening length. The ten globular clusters are initially distributed within the halo between 20 pc and 1000 pc. They are placed according to

$$\rho(r) \propto r^{-4}, \tag{95}$$

which is the way globular clusters are situated in dwarf galaxies (Sharina, Puzia & Makarov 1996), and put on circular orbits in random planes. We tried different distributions like r^{-3} or r^{0} with the same results as presented in this case. We let this system evolve for 0.72 Gyr. Afterwards we put it into an artificial NFW potential, which corresponds to a halo of mass $10^{14}\,\mathrm{M}_{\odot}$ with concentration 6. We let the particles start at a distance of 100 kpc with a velocity of 650 km/s so that it orbits the centre of the potential with a distance between 100 kpc and 500 kpc. For a second simulation we put just two of these globular clusters 10 pc apart from each other, without any initial velocity and let them evolve purely under the influence of their mutual gravity. For a third simulation we put fifty of these globular cluster in the aforementioned halo and let them spiral into the centre. These three simulations do not include gas dynamics, therefore they are only valid after the expulsion of gas from the star clusters.

All ten globular clusters in our first simulation merge to a single object within 0.4 Gyr. The associated timescale of this evolution can be calculated using the Chandrasekhar dynamical friction formula (Chandrasekhar 1943). The final equation is:

$$\begin{aligned}\frac{dr}{dt} &= -\frac{4\pi \ln\Lambda(r)\rho(r)G^2 M_{\mathrm{GC}} r}{v_{\mathrm{c}}^2(r) d\left[r v_{\mathrm{c}}(r)\right]/dr}\left\{\mathrm{erf}\left[\frac{v_{\mathrm{c}}(r)}{\sqrt{2}\sigma(r)}\right]\right. \\ &\quad - \left.\frac{2v_{\mathrm{c}}(r)}{\sqrt{2\pi}\sigma(r)}\exp\left[\frac{-v_{\mathrm{c}}^2(r)}{2\sigma^2(r)}\right]\right\}, \qquad (96)\end{aligned}$$

where $v_{\mathrm{c}}(r)$ is the circular speed at radius r, $\ln\,\Lambda(r)$ the so-called Coulomb logarithm, M_{GC} is the mass of one globular cluster. $\rho(r)$ is the density of the dark matter halo at radius r according to equation (93) and $\sigma(r)$ is the one-dimensional velocity dispersion of the halo. For the derivation of equation (96) see Goerdt et al. (2006). When we solve it numerically we get for the dynamical friction timescale $t_{\mathrm{fric}} = 0.4$ Gyr, which is surprisingly close to the value we get with the simulation.

The different globular cluster approach the central compact object as seen in Fig. 41. The centre of mass of the luminous matter orbits the centre of mass of the total matter as shown in Fig. 42.

The central compact object has a three-dimensional density profiles as shown in Fig. 43. This is very similar to observations (de Propris et al. 2005) as well as previous simulations (cf. Fig. 5 in Fellhauer & Kroupa (2002)).

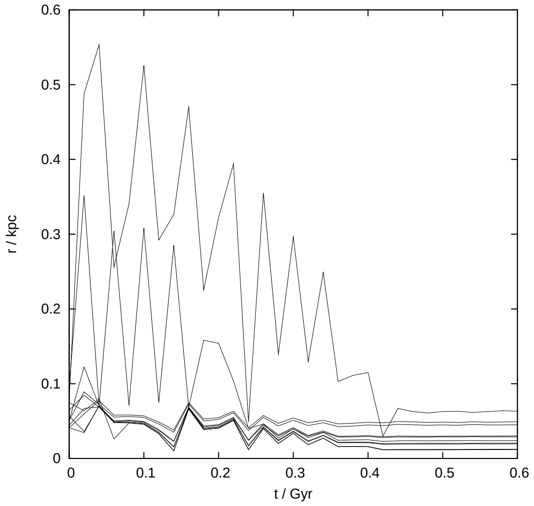

Figure 41: Median radial distance of the particles of the ten globular clusters from the centre of their host halo as function of time, as they orbit within the cuspy density distribution.

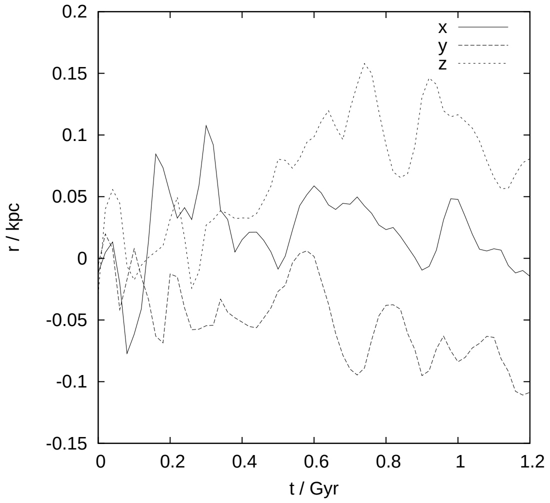

Figure 42: Movement of the centre of luminous mass (i.e the GCs) with respect to the centre of mass of the dark matter, shown are the x, y and z components.

The density profile of the baryonic matter only (i.e. just the material, which has been in the globular clusters before) can be well-fitted with a Plummer

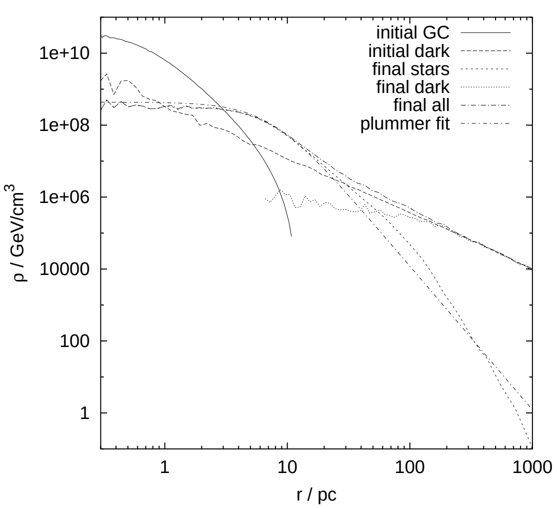

Figure 43: Density profile of the UCD, before it has been put into an external potential. The profile of all the matter, the one of the stars only and the one of only the dark matter is shown. On top the density profile of the initial globular cluster and the best fit plummer model is drawn.

model (Plummer 1911):

$$\rho(r) = \frac{3M}{4\pi b^3}\left(1 + \frac{r^2}{b^2}\right)^{-5/2} \tag{97}$$

In our case $M = 1.45 \times 10^6\,\mathrm{M}_\odot$ and $b = 7.26\,\mathrm{pc}$. The resulting object has a half mass radius of 25 pc and a central velocity dispersion of 20 km/s. The projected surface density profile can bee seen in Fig. 44. This can as well be fitted with a Plummer model. The equation for the fit has been found by Evans & An (2005):

$$\Sigma(r) = \frac{A}{\pi\left(1 + r^2/b^2\right)^2} \tag{98}$$

For our fit we find: $A = 3.3 \times 10^4\,\mathrm{M}_\odot/\mathrm{pc}^2$ and $b = 8.7\,\mathrm{pc}$. It looks fairly similar to observations and previous simulations (cf. Fig. 5 in Haşegan et al. (2005) or Fig. 6 in Fellhauer & Kroupa (2002)). If we assume a mass to light ratio of three, we expect an absolute visual magnitude of -11. For comparison, one of the UCDs found in Fornax has a central velocity dispersion of 22 km/s, an absolute magnitude of -12 and a half mass radius of 25 pc (Haşegan et al. 2005; Drinkwater et al. 2003). So one would need to merge much more globulars to reach the observed luminosity. This turns out to be a crucial

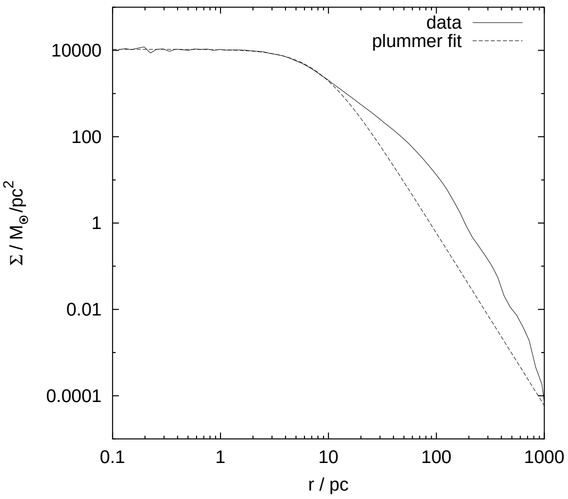

Figure 44: Projected surface density profile of the UCD, before it has been put into an external potential. The profile of the luminous matter together with the best fit plummer model is plotted.

point in this creation scenario because more than ten globulars in such a halo are extremely rare (Sharina, Puzia & Makarov 1996). An interesting feature to notice in the final UCD is that all the dark matter is expelled from the core. In our simulation one does not find a single dark matter particle within the inner 5 pc. This effect has been discussed in more detail in Read et al. (2006). It is the second fact which excludes the underlying creation scenario. The observed M/L ratio cannot possibly be reached without dark matter. Another peculiarity is that the Plummer model does not follow the data exactly. Instead the data curve has a small "belly" between radii of 20 pc and 120 pc (See Fig. 44). This might be the case because the stars from the globular clusters, which have been furthest away (about 120 pc) have been randomly scattered.

The two globular clusters in our second simulation merged completely within a few million years. The resulting object had a central velocity dispersion of 16 km/s and an absolute magnitude of -9.3, again assuming a mass to light ratio of two. The fifty globular clusters in our third simulation merged completely within a few million years. The resulting object had a central velocity dispersion of 37.3 km/s and an absolute magnitude of -12.75, assuming a mass to light ratio of three. Its position is marked in Fig. 45. Its position would roughly match an UCD.

We mark the initial globular cluster and the three objects resulting from our simulations in a σ_0-$\mathrm{M_V}$ plane. We determine $\mathrm{M_V}$, by choosing the M/L to be 3 and calculating the magnitude according to the mass. σ_0 is determined by the movement of the particles in our simulations. Now we can read off two merging vectors. These two merging vectors point in roughly the same direction. Looking at Fig. 45 it becomes evident, that our three objects as well as the merging vector lie on the line on which the globular clusters and the UCDs are centred. This is due to Jeans equation (Jeans 1919):

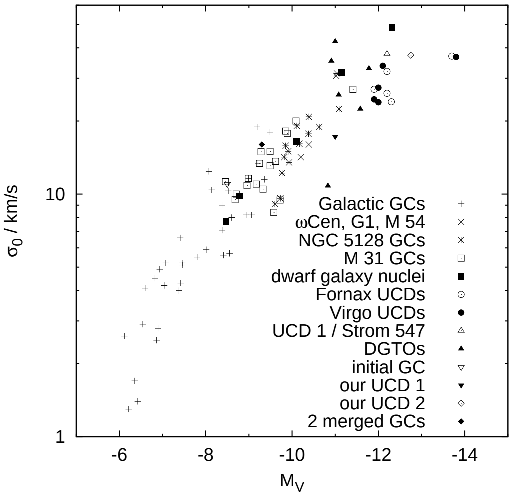

Figure 45: Central velocity dispersion versus absolute visual magnitude for hot stellar systems. Observations are plotted together with the results from our simulations. Data taken from Haşegan et al. (2005); Evstigneeva, Gregg & Drinkwater (2005) and references therein.

$$\frac{\partial \nu}{\partial t} + \frac{\partial(\nu \bar{v}_i)}{\partial x_i} = 0 \tag{99}$$

This scenario does not work, because it is very unrealistic to have a sufficient amount of globular clusters in a halo of that size. It becomes apparent in Fig. 45 that it is not sufficient to merge only ten globulars, but fifty globulars, which would be needed, one would not find in such a halo (Sharina, Puzia, Makarov 1996). The second big drawback of this model is that even if found that many globular clusters in such a halo, which would merge to give the UCD-like object, the stars of the globulars, would replace the dark matter particles, expel them from the centre of the halo (El-Zant, Shlosman

& Hoffman 2001; Merritt et al. 2004) and thus lower the M/L ratio beyond observational constraints (Haşegan et al. 2005).

6.4 Are UCDs stripped disk galaxies?

To test the idea, if the UCDs are remnants of stripped disk galaxies we set up a spherical equilibrium halo with an NFW profile and structural parameters consistent with predictions of the standard ΛCDM model (Kazantzidis, Magorrian & Moore 2004). We include a fraction of the total halo mass, f_b, as a hot baryonic component with the same radial distribution and a temperature profile such that the gas is initially in hydrostatic equilibrium for an adiabatic equation of state (EOS) for the gas.

The gas has a specific angular momentum distribution and spin parameter consistent with values found for dark matter haloes within cosmological N-body simulations (Bullock et al. 2001). We constructed a dark plus gaseous halo model with parameters that are expected to produce disks similar to the Local Group galaxy M33. The model parameters are: $M_\mathrm{vir} = 5 \times 10^{11}$ $\mathrm{M}_\odot$, $r_\mathrm{vir} = 167$ kpc, $v_\mathrm{vir} = 115$ km/s, $c = 6.2$, baryonic fraction $f_\mathrm{b} = 6\%$ and spin parameter $\lambda = 0.105$. The hot gaseous halo is resolved with 2×10^6 particles of equal mass $\sim 2 \times 10^4$ $\mathrm{M}_\odot$. We sampled the dark matter halo with 2.2×10^6 particles having variable masses, the resolution increasing towards the centre of the system (Zemp 2006). With a single-resolution model one would need about ten million particles to reach a comparable resolution in the central region. This allows us to simulate the central dark matter cusp with softening of 100 pc and particle mass of $\sim 4.4 \times 10^4$ $\mathrm{M}_\odot$. The detailed description of the initial conditions and results of the evolution of the disk are presented in Kaufmann et al. (2006a) and Kaufmann et al. (2006b).

We use the parallel Tree+SPH code GASOLINE (Wadsley, Stadel & Quinn 2004), which is an extension of the pure N-Body gravity code PKDGRAV developed by Stadel (2001). It uses an artificial viscosity which is the shear reduced version (Balsara 1995) of the standard Monaghan (1992) artificial viscosity. GASOLINE uses a spline kernel with compact support for the softening of the gravitational and SPH quantities. The energy equation is solved using the asymmetric formulation, which is shown to yield very similar results compared to the entropy conserving formulation but conserves energy better (Wadsley, Stadel & Quinn 2004). The code includes radiative cooling for a primordial mixture of helium and (atomic) hydrogen. Because of the lack of molecular cooling and metals, the efficiency of our cooling functions drops rapidly below 10 000 K, but we adopt a temperature floor of $T_{\mathrm{f}} = 15\,000$ K, to crudely mimic the effect of heating sources such as supernovae explosions and radiation (e.g. ultraviolet) backgrounds. These simulations run without any star formation.

Due to cooling the hot gas halo loses its hydrostatic equilibrium configuration quite quickly. The inner disk rapidly forms out of cooling gas coming from a nearly spherical region close to the centre (within $\sim$ 10 kpc) of the halo. After 2.5 Gyr of evolution the disk attains a near exponential surface density profile over a large fraction of its extent, except within a few hundred parsecs from the centre, where a dense nucleus produces a central spike in the profile (Fig. 46). It has a mass of $\sim 3 \times 10^7$ M$_\odot$, which is $\sim$ 0.6% of

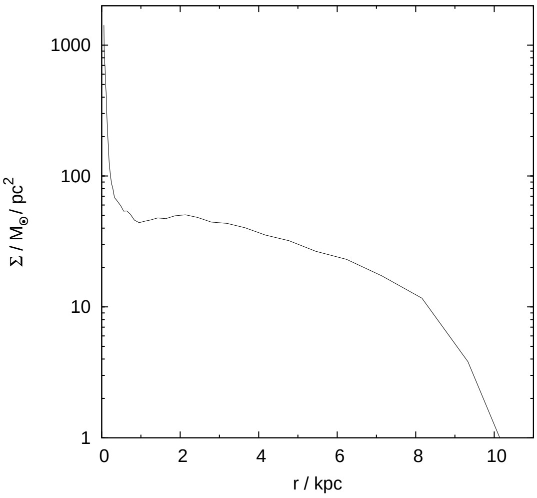

Figure 46: The logarithmic surface density of the M33 gas disk is plotted after 2.5 Gyr. The nucleus in the centre is clearly visible.

the total disk. Central dense stellar nuclei have been seen in several late-type spiral galaxies, for example, in M33 (Regan & Vogel 1994), but also in other late-type spirals (Carollo 1999; Carollo, Stiavelli & Mack 1998). Recent observations by Ferrarese et al. (2006) show that they are expected in 50 - 80% of low- and intermediate- luminosity galaxies.

In order to strip the dark matter particles and the gas disk, we put it, together with its dark matter halo, into an artificial NFW potential. So we are neglecting the effects of ram pressure stripping. This potential roughly reassembles the Virgo cluster: It has a virial mass of 3 $\times 10^{14}$ $M_\odot$, a concentration of 6 and a virial radius of 1.8 Mpc. We start the disk at pericentrum, 100 kpc far from the centre of the artificial potential, and give it a perpendicular velocity of 260 km/s, such that it should reach an apocentrum at 30 kpc. The plane of the disk is tilted by 45° with respect to the plane of the orbit. All dark matter particles, as well as the gas disk are actually stripped from the nucleus. The surface brightness profile of the resulting object is shown in Fig. 47. It is clearly visible, that it does resemble the observations quite well. The

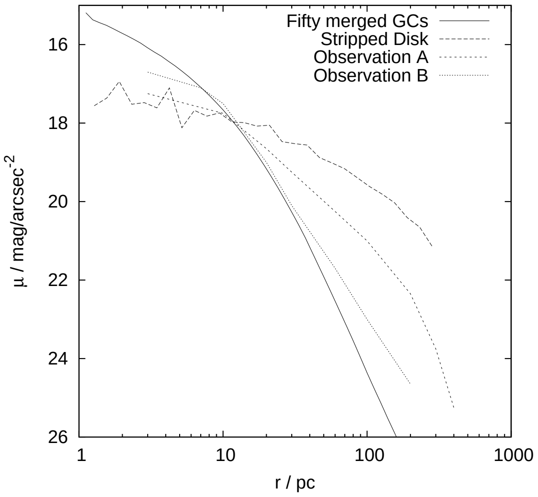

Figure 47: Surface brightness profiles of our simulations and observations. Observational data is taken from De Propris et al. (2005).

half light radius is in good agreement with observations, so is the M/L ratio.

A further hint on the plausibility of this formation scenario can give the positions of the UCDs found so far. All of them are located in galaxy clusters close to the cluster centre. No one is further away from the centre than 200 kpc. On the other hand dE(N)s appear only in galaxy clusters as well but normally they are further away from the centre. Now we did an extensive set of simulations to test, on which orbits our disk gets completely stripped to produce an UCD and on which orbits it remains almost completely intact to produce a dE(N). Therefore we repeated the stripping simulation just described with varying apo- and pericentres. If this formation scenario is correct then there must be a very sudden transition between these two cases, because in nature we only observe these very distinct two types of galaxies and no third intermediate object. In Fig. 48 you can see the surface brightness pro-

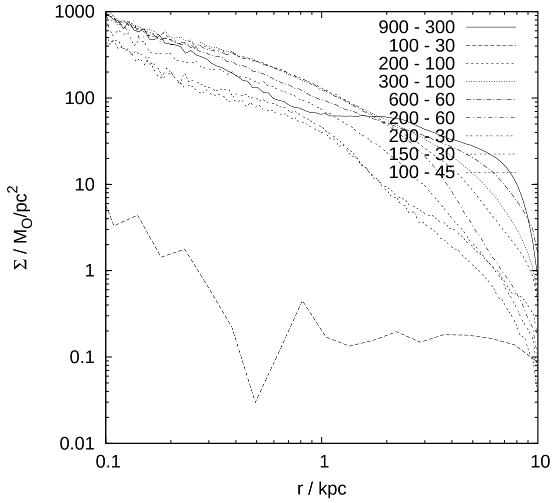

Figure 48: Surface brightness profiles of the stripped disk after orbiting an artificial Virgo cluster potential for 5 Gyr. The numbers in the legend give the apo- and pericentres of the various orbits in kpc.

files of our disk after orbiting the artificial galaxy cluster potential for 5 Gyr on various orbits. As you can clearly see, there is a sudden transition: if either there is almost no stripping or there is complete stripping destroying the disk. In Fig. 49 you can see whether the disk got stripped or not for any given apo- and pericentres. The dividing line between complete stripped disk and complete survival can be expressed as:

$$r_{peri} = A r_{apo} + B \tag{100}$$

with A = -0.32 and B = 68. We repeated those stripping experiments with the dark matter halo only, leaving out the gas disk. In Fig. 50 you can see whether the nucleus of the halo got stripped or not for any given apo- and pericentres. The dividing line between complete stripped disk and complete survival can be expressed as:

$$r_{peri} = A r_{apo} + B \tag{101}$$

with A = -0.20 and B = 91.

As a next step we analysed the dynamics of a dark matter halo from a cos-

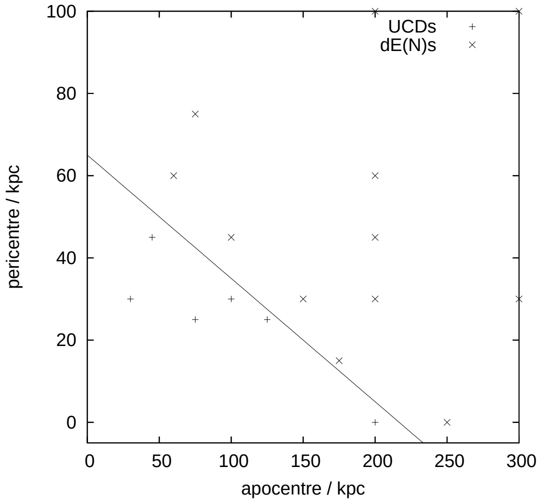

Figure 49: Disrupted and non disrupted disk as a function of apo- and pericentre for all disk-simulations we have done.

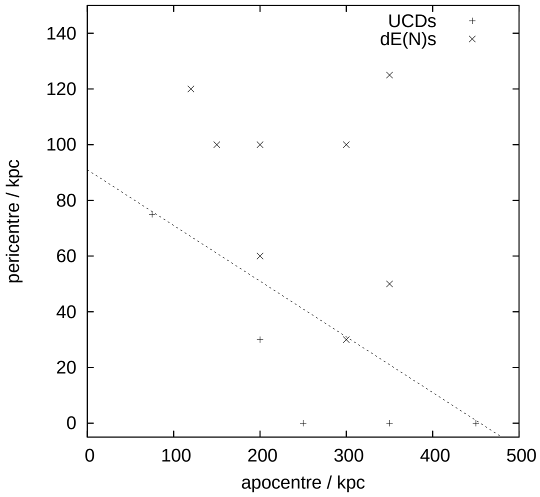

Figure 50: Disrupted and non disrupted nucleus as a function of apo- and pericentre for all dark matter only simulations we have done.

mological simulation (see appendix 6.7), which is comparable to the halo the Virgo galaxy cluster is expected to have. We used a halo from a cosmological simulation instead of an artificial halo, because in the latter case the orbits of the particles are usually unrealisticly less eccentric (Kazantzidis, Magorrian & Moore 2004). The radial density profile can be described by a generalisation of equation (93), the α, β, γ law (Hernquist 1990):

$$\rho(r) = \frac{\rho_0}{\left(\frac{r}{r_s}\right)^{\gamma}\left[1+\left(\frac{r}{r_s}\right)^{\alpha}\right]^{\frac{\beta-\gamma}{\alpha}}} \qquad (r \leq R_{\text{vir}}), \tag{102}$$

This halo had $\alpha = 1.23$, $\beta = 3.74$, $\gamma = 1.38$, $\rho_o = 3.54$ MeV/cm^3 and $r_s =$ 722 kpc. We took this halo, and evolved it in isolation for 5 Gyr. We binned all the particles according to their projected distance from the centre in the last output (i.e. $\sqrt{x^2+y^2}$, neglecting the z-coordinate). Then we computed the fraction of particles which lie below the solid line in Fig. 49 and or in Fig. 50. This fraction is then compared to the fraction of the number of UCDs to the sum of the number of UCDs and the number of dE(N)s in nature (See Fig. 51). The the pure N-body simulations with the dark matter halo only lead to the upper cosmological prediction and the SPH simulations with the gas disk included lead to the lower cosmological prediction. The observational data has been prepared the following way: We took the projected distances of the UCDs and dE(N)s measured in arcsec from Jones et al. (2006) and converted them into kpc assuming distances to the Virgo galaxy cluster of 16

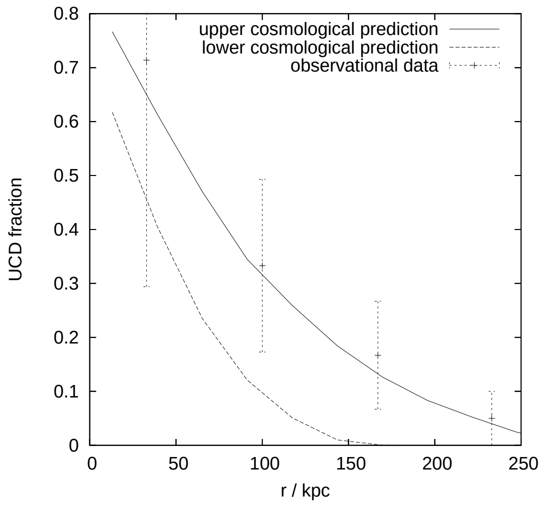

Figure 51: The ratio of the number of UCDs to the sum of the number of UCDs and the number of dE(N)s as a function of radius. The upper cosmological prediction comes from the simulations with only dark matter in it and the lower cosmological prediction comes from the SPH simulations with the gas disk. Observational data is taken from Jones et al. (2005).

Mpc and to the Fornax galaxy cluster of 20 Mpc. In a ΛCDM universe all haloes are selfsimilar, i.e. scalable. This enables us to add up the occurrences of our objects to get a better statistic. We rescale the projected distances of all our objects in a way that their host halo fits the values for the halo we took from our cosmological simulation [see equation (102)] as good as possible. After rescaling we binned the occurrence of the UCDs and dE(N)s according to their rescaled projected distance to their mutual galaxy cluster centre into common bins. The content of each bin gets a Poissonian error attached to it. Finally we divide the number of UCDs in each bin by the sum of the numbers of UCDs and dE(N)s and propagate the errors accordingly. From comparing our two cosmological prediction with the data, we conclude that (a) both UCDs and dENs develop from the same progenitors and (b) this progenitor must be something in between the disk and the dark matter halo we tried in our simulations. You have to keep in mind though, that only 15 UCDs have been discovered so far. We put those 15 data points into 4 bins, resulting in a very poor statistic, which is indicated by the rather large error bars. However, our cosmological prediction agrees very well with the data, as you can clearly see.

6.5 Conclusions

Our simulations reveal, that a swarm of ten to fifty globular clusters born in a Fornax size dark matter halo will normally evolve to an object, which has the same density profile as an UCD. Moreover the density profile, as well as the half light radius of this object is in excellent agreement with observations. The fact that in the σ_0-$\mathrm{M_V}$ plane the start and end points of our simulations lie on the same 'merging line' could give rise to the suggestion that it is possible to construct UCDs of different masses from a number of different globular clusters, as long as both lie on this 'merging line'. The drawbacks of this model are, that it is very unrealistic to have so many globular cluster in a halo of that size. It becomes apparent in Fig. 45 that it is not sufficient to merge only ten globulars: fifty are necessary. However such a halo may not exist (Sharina, Puzia & Makarov 1996). The second big drawback of this model is that even if you would find that many globular clusters in such a halo, which would merge to give the UCD-like object, the stars, consisting the globulars, would replace the dark matter particles and expel them from the centre of the halo (El-Zant, Shlosman & Hoffman 2001; Merritt et al.

2004) lowering the M/L ratio beyond observational constraints (Haşegan et al. 2005). Therefore we performed a second series of simulations in which we grow a gaseous disk, form an object in the very centre and strip the disk away. This central object has, up to the resolution limit, all the features the observed UCD have. On top of that this model gives a prediction of the occurrence of UCDs respective d(E)Ns within a single galaxy cluster. This predictions agrees very well with the observations, even if one has to say that the data, we have so far, are not sufficient for making proper statistics.

6.6 Acknowledgements

It is a pleasure to thank Monica Haşegan, Bryn Jones, Katya Evstigneeva and Michael Drinkwater for their kindness to send us data to help with our figures. All computations were made on the zBox or zBox2 supercomputers (http://www.zbox1.org or http://www.zbox2.org) at the University of Zürich. Special thanks go to Doug Potter for bringing them to life.

6.7 The cosmological simulations

The haloes have been extracted from an existing cosmological N-body simulation. This simulation have been performed with PKDGRAV, a tree code written by Joachim Stadel and Thomas Quinn (Stadel 2001). We adopt a flat ΛCDM cosmology using the parameters from the first year WMAP results (Spergel et al. 2003): matter density $\Omega_M = 0.268$, baryon density $\Omega_b = 0.044$, Hubble constant $h \equiv H_0/(100kms^{-1}Mpc^{-1}) = 0.71$, and a scale-invariant, Harrison-Zeldovich power-spectrum with normalisation $\sigma_8 = 0.9$. The initial conditions are generated with the GRAFIC2 package (Bertschinger 2001), which also computes the transfer function as described in Ma & Bertschinger (1995). The starting redshifts z_i are set to the time when the standard deviation of the smallest density fluctuations resolved within the simulation box reaches 0.2. The code uses spline kernel softening, for which the forces become completely Newtonian at 2 softening lengths. Individual time steps for each particle are chosen proportional to the square root of the softening length, ϵ, over the acceleration, a: $\Delta t_i = \eta\sqrt{\epsilon/a_i}$. Throughout, we set $\eta = 0.2$, and we keep the value of the softening length constant in comoving coordinates during each run. The physical values of ϵ at $z = 0$ is 1.16 kpc. Forces are computed using terms up to hexadecapole order and a node-opening angle θ which we change from 0.55 initially to 0.7 at $z = 2$. This allows a higher force accuracy when the mass distribution is nearly smooth and the relative force errors can be large. The simulation has periodic boundary conditions, a Box size of 90 Mpc and we evolved 600^3 equal mass dark matter particles, obtaining a mass resolution of $1.26 \times 10^8 M_\odot$.

The haloes are identified using a SO (Spherical Overdensity) algorithm. As a first step, candidate haloes are located using the standard friends-of-friends (FOF) algorithm, with a linking length $bn^{-1/3}$, with n the mean particle density and b a free parameter which we set to 0.2. We only keep FOF haloes with at least $N_{\rm min} = 200$ particles, which we subject to the following two operations: (i) we find the point, C, where the gravitational potential due to the group of particles is minimum, and (ii) we determine the radius $R_{\rm vir}$, centred on C, inside of which the density contrast is $\Delta_{\rm vir}$. For our adopted cosmology $\Delta_{\rm vir} \simeq 98$ (using the fitting function of Mainini et al. 2003). Using all particles in the corresponding sphere we iterate the above procedure until we converge onto a stable particle set. The set is discarded if, at some stage, the sphere contains less than $N_{\rm min}$ particles. If a particle is a potential member of two haloes it is assigned to the more massive one. For each stable particle set we obtain the virial radius, $R_{\rm vir}$, the number of particles within the virial radius, $N_{\rm vir}$, and the virial mass, $M_{\rm vir}$.

7 Concluding remarks and future prospects

In this thesis, I have studied a number of related aspects on the currently prevailing theory of structure formation in a universe dominated by cold dark matter. The concordance ΛCDM cosmological model for structure formation has been remarkably successful in explaining most of the properties of the universe on large scales and at various cosmic epochs. Recent results from microwave background experiments and large redshift surveys have highlighted the ability of this model to reproduce observations as diverse as the abundance and clustering of galaxies and clusters and the statistical properties of the Lyα forest within constraints set by measurements of the primordial fluctuation spectrum, observations of distant Type Ia supernovae, and gravitational lensing statistics. However, on non-linear scales the ΛCDM model has been neither convincingly verified nor disproved, and several outstanding issues remain unresolved.

One of the major shortcomings of any CDM model is the difficulty in matching the steep observed luminosity function with the flat mass spectrum of haloes predicted from simulations or Press-Schechter models. From cosmological N-body simulations this problem manifests itself as a lack of observed substructure in the vicinity of our Milky Way and other galaxies. Several alternative dark matter candidates have been proposed to address this and related problems, such as the harmonic core at the centre of the Fornax dwarf spheroidal, many of which can be tested using observations of galaxies on small scales. An alternative cosmology, which provides a natural explanation for the lack of substructure, is warm dark matter, which introduces an additional free parameter - the free streaming scale.

In chapter 2, I discussed that the dark matter dominated Fornax dwarf spheroidal has five globular clusters orbiting at $\sim 1\,\mathrm{kpc}$ from its centre. In a cuspy CDM halo the globulars would sink to the centre from their current positions within a few Gyrs, presenting a puzzle as to why they survive undigested at the present epoch. I show that a solution to this timing problem is to adopt a cored dark matter halo. I use numerical simulations and analytic calculations to show that, under these conditions, the sinking time becomes many Hubble times; the globulars effectively stall at the dark matter core radius. I conclude that the Fornax dwarf spheroidal has a shallow inner density profile with a core radius constrained by the observed positions of its globular clusters. If the phase space density of the core is primordial then it implies a warm dark matter particle and gives an upper limit to its mass of $\sim 0.5\,\mathrm{keV}$, consistent with that required to significantly alleviate the substructure problem.

In chapter 3, I showed using analytic calculations and N-body simulations that in constant density (harmonic) cores, sinking satellites undergo an initial phase of very rapid (super-Chandrasekhar) dynamical friction, after which they experience no dynamical friction at all. This occurs because, for the special case of harmonic potentials, there are stable solutions where the background particles move on epicycles about the in-falling satellite. The system moves rapidly into this stable configuration. In doing so, the satellite experiences a brief moment of enhanced friction. Once in equilibrium, there is no net momentum transfer between the background particles and the satellite and friction ceases. For density profiles with a central power law profile, $\rho \propto r^{-\alpha}$, the infalling satellite heats the background and causes α to decrease. For $\alpha < 0.5$ initially, the satellite generates a small central constant density core and stalls as in the $\alpha = 0$ case.

The existence of galaxies with binary nuclei, like VCC 128 observed recently by Debattista et al. (2006), provide a puzzle for cold dark matter models which ubiquitously predict central cusps. VCC 128 has two dense stellar clusters separated by 50 parsecs. In chapter 4, I have calculated the dynamical friction timescale for these two nuclei to sink and coalesce within different dark matter cuspy haloes. For a CDM halo, I find that this should happen within a few million years, thus to observe this system in its current state appears to be unlikely. I investigated the statistics of such systems and thus place constraints on the inner cusp slopes of the galaxies - shallower slopes give rise to longer friction timescales. Furthermore, as I showed earlier, long lived binary nuclei can only exist in constant density cores - which again may be connected to the nature of the dark matter.

If the dark matter particle is a neutralino then the first structures to form are cuspy cold dark matter (CDM) haloes collapsing at redshifts $z \approx 100 - 50$ in the mass range $10^{-6} - 10^{-3}\,M_{\odot}$. In chapter 5, I carried out a detailed study of the survival of these micro-haloes in the Galaxy as they experience tidal encounters with stars, molecular clouds, and other dark matter substructures. I test the validity of analytic impulsive heating calculations using high resolution N-body simulations. A major limitation of analytic estimates is that mean energy inputs are compared to mean binding energies, instead of the actual mass lost from the system. This energy criterion leads to an overestimate of the stripped mass and underestimate of the disruption timescale since CDM haloes are strongly bound in their inner parts. I showed that a significant fraction of material from CDM micro-haloes can be unbound by encounters with Galactic substructure and stars, however the cuspy central regions remain relatively intact. Thus I expect a significant smooth component with narrow features in phase space, which may be uncovered by direct detection experiments, as well as numerous surviving cuspy cores with proper motions of arc-minutes per year, which can be detected indirectly via their annihilation into gamma-rays.

Ultra compact dwarf galaxies (UCDs) are a new and interesting class of galaxies that have some resemblance to very large globular clusters. Indeed, a popular formation mechanism for UCDs is via the sinking of globular clusters by dynamical friction, thus merging at the galactic centre to form a single dense nucleus. In chapter 6, I have studied this process with high resolution numerical simulations and find that this produces density profiles and half light radii which fit the observed UCDs very well. Unfortunately, this model has two major drawbacks. The observed UCDs are too luminous and have a mass-to-light ratio which is too high. Therefore I investigated a second possible formation scenario - that UCDs are the dense nuclei of stripped disk galaxies. My results show that this explanation seems to match all the observational constraints and also gives a prediction of their radial distribution in clusters.

There are several key unsolved problems within the standard cosmological model. One of the most outstanding issues is to understand the formation of galaxies and their stellar components such as globular clusters. The connection between these components and the dwarf galaxies may bring together several areas of research. To reveal their formation mechanisms would help solving some of the contemporary mysteries of our universe. Interesting unanswered questions in cosmology and galaxy formation are for example:

The formation of globular clusters is still a fascinating unsolved problem in cosmology. Literally thousands of papers have been written on observational studies of these objects, yet theoretical studies have not made much progress in the last thirty years. One wishes to explore the possible connection between dark matter substructures at high redshift and globular clusters. Recent studies have made a connection between the radial distribution of biased dark matter and the radial distribution of galactic globulars. One is interested in the gas processes that occur within the first dark matter structures that are massive enough to cool baryons and which may be the sites of cluster formation. Using smoothed particle hydrodynamical simulations one would like to attempt to follow the fragmentation of the gas clouds within these early systems and to study the effects of supernovae and merger triggered star formation.

The history and evolution of our very own Milky Way has always been a very interesting topic. Its stellar disk is believed to have grown slowly over time. A globular cluster orbiting around the this stellar disk over its whole lifetime would have experienced its changing potential. Several old globular cluster and streams of distorted objects have been observed in the outer halo of our galaxy. One is running N-body/SPH simulations of objects orbiting a growing disk to compare to those observations. By doing so, one hopes to gain some insight about the evolution history of the Milky Way.

Dynamical friction is an essential component in galaxy formation and galactic dynamics. Without dynamical friction we could not have the hierarchical build up of structures as observed in numerical simulations. Indeed, it is a fundamental prediction of cosmological models in which the dark matter is a collisionless particle. Therefore it would be of extreme interest to actually verify that dynamical friction happens in nature. This could be a direct test of the collisionless nature of dark matter for example. I am investigating observational tests which include looking for the visible density enhancements, for example in the wakes in the diffuse intra-cluster stars behind orbiting galaxies, or the wakes introduced in elliptical galaxies from the motions of dark matter substructures.

For globular clusters orbiting a disk galaxy coplanar within its disk, many of the assumptions Chandrasekhar made in deriving his dynamical friction formula do not hold. For example, the net velocity of background stars maybe comparable to the motion of the globular cluster. The bias in sinking times of prograde versus retrograde clusters maybe lead to interesting observable consequences, such as a net rotational signature of the globular cluster system. One would like to study this effect using high resolution stable galactic models in an attempt to understand the kinematics of the disk population of Galactic globular clusters, as well as checking the validity of the friction formula under such circumstances.

It would be interesting to quantify the stripping behaviour of haloes in general. The work presented in chapter 5 gave the rather unexpected result that the stripping behaviour, as a function of repeated encounters, of the microhaloes, we used, is easily quantifiable. It would be interesting to investigate further on this and try to find a theoretical underlying for the empirically found relationships. Another goal could be to predict the final density profile of a halo of a given mass after n encounters.

Many galaxies have dense, stellar nuclei, from large ellipticals to dwarf spheroidals. The origin of these nuclei is debated and suggestions have ranged from sinking star clusters to gas flows in stellar bars. The properties of these nuclei have recently been connected to the scaling relations involving supermassive black holes. Using high resolution smoothed particle hydrodynamical simulations, one aims to investigate the properties of these dense nuclei that form via hydrodynamical instabilities. For example, the formation of a bar during the early phase of galaxy formation may be responsible for funneling gas to the central regions of galaxies. One wishes to study how the properties of this gas flow, and the final central baryonic mass, correlate with the environment and initial conditions.

However the most puzzling questions of cosmology *"What is the physical nature of the dark matter?"* is still far from being solved. This question is also of particular interest for particle physics. One of the most popular candidate for a DM particle is the neutralino from super-symmetric (SUSY) scenarios. Experiments at the LHC at CERN will search for indirect evidence of these particles. Besides new data from such experiments, there is a huge amount of new astronomical and cosmological observations expected (e.g. new WMAP results, GAIA or LISA) in the next few years. Theoretical models that try to keep up and explain the observations will likely have to include more details on the physical processes. Computational resources are becoming more powerful than ever. So it appears that in future numerical astrophysics will become even more outstanding.

References

Aarseth S. J, 1984, in Methods of Computational Physics, eds. J. U. Brackhill, B. J. Cohen, Academic, New York

Aguilar L. A, White S. D. M, 1985, ApJ, **295**, 374

Aguilar L. A, White S. D. M, 1986, ApJ, **307**, 97

Angus G. W, Zhao H. S, 2007, MNRAS, **375**, 1146

Ashman K. M, Zepf S. E, 1992, ApJ, **384**, 50

Bahcall J. N, 1984, ApJ, **276**, 169

Balsara D. S, 1995, J. Comput. Phys, **121**, 357

Barmby P, Huchra J. P, 2001, ApJ, **122**, 2458

Barnes J, Hut P, 1986, Nat, **324**, 446

Bekki K, Couch W. J, Drinkwater M. J, 2001, ApJ, **552**, 105

Bekki K, Couch W. J, Drinkwater M. J, 2003, MNRAS, **344**, 399

Bennet C. L, Halpern M, Hinshaw G. et al, 2003, ApJS, **148**, 1

Bertschinger E, 2001, ApJS, **137**, 1

Berezinsky V, Dokuchaev V, Eroshenko Y, 2006, PhRvD, **73**, 063504

Binney J, 1977, MNRAS, **181**, 735

Binney J, Evans N. W, 2001, MNRAS, **327**, 27

Binney J, Merrifield M, 1998, Galactic Astronomy (Princeton, NJ, Princeton University Press)

Binney J, Tremaine S, 1987, Galactic Dynamics (Princeton, NJ, Princeton University Press)

Boily C. M, Nakasato N, Spurzem R, Tsuchiya T, 2004, ApJ, **614**, 26

Bontekoe T. R, van Albada T. S, 1987, MNRAS, **224**, 349

Borriello A, Salucci P, 2001, MNRAS, **323**, 285

Bullock J. S, Dekel A, Kolatt T. S. et al, ApJ, **555**, 240

Calcáneo-Roldán C, Moore B, 2000, PhRvD, **62**, 123005

Capuzzo-Dolcetta R, Vicari A, 2005, MNRAS, **356**, 899

Carollo C. M, 1999, ApJ, **523**, 566

Carollo C. M, Stiavelli M, Mack J, 1998, AJ, **116**, 68

Carr B. J, Sakellariadou M, 1999, ApJ, **516**, 195

Carroll B, Ostlie D, 1996, An Introduction to Modern Astrophysics, Weber State University.

Chandrasekhar S, 1943, ApJ, **97**, 255

Clowe D, Bradač M, Gonzalez A. H. et al, 2006, ApJ, **648**, 109

Coleman M. G, Da Costa G. S, Bland-Hawthorn J, Freeman K. C, 2005,

AJ, **129**, 1443
Colpi M, Mayer L, Governato F, 1999, ApJ, **525**, 720
Cora S. A, Muzzio J. C, Vergne M. M, 1997, MNRAS, **289**, 253
Dalcanton J. J, Hogan C. J, 2001, ApJ, **561**, 35
Dauphole B, Geffert M, Colin J. et al, 1996, A&A, **313**, 119
Davis M, Efstathiou G, Frenk C. S, White, S. D. M, 1985, ApJ, **292**, 371
de Blok W. J. G, McGaugh S. S, Bosma A, Rubin V. C, 2001, ApJ, **552**, 23
de Propris R, Phillipps S, Drinkwater M. J, 2005, ApJ, **623**, 105
de Rijcke S, Michielsen D, Dejonghe H, Zeilinger W. W, Hau G. K. T, 2005, A&A, **438**, 491
Debattista V. P, Ferreras I, Pasquali A, et al, 2006, ApJ, **651**, 97
Debattista V. P, Sellwood J. A, 1998, ApJ, **493**, 5
Debattista V. P, Sellwood J. A, 2000, ApJ, **543**, 704
Dehnen W, 1993, MNRAS, **265**, 250
Diemand J, Madau P, Moore B, 2005, MNRAS, **364**, 367
Diemand J, Moore B, Stadel J, 2004, MNRAS, **352**, 535
Diemand J, Moore B, Stadel J, 2005, Nat, **433**, 389
Diemand J, Kuhlen M, Madau P, 2006, ApJ, **649**, 1
Dinescu D. I, Keeney B. A, Majewski S. R, Girard T. M, 2004, AJ, **128**, 687
Drinkwater M. J, Gregg M. D, Hilker M et al, 2003, Nat, **423**, 519
Dubinski J, Carlberg R. G, 1991, ApJ, **378**, 496
Efstathiou G, Davis M, Frenk C. S, White S. D. M, 1985, ApJS, **57**, 241
Eggen O. J, Lynden-Bell D, Sandage A. R, 1962, ApJ, **136**, 748
El-Zant A, Shlossman I, Hoffman Y, 2001, ApJ **560**, 636
Elmegreen B. G, Efremov Y. N, 1999, AJ, **480**, 235
Evans N. W, An J, 2005, MNRAS, **360**, 492
Evstigneeva E. A, Gregg M. D, Drinkwater M. J, 2005, astro-ph/0504289
Fellhauer M, Kroupa P, 2002, MNRAS, **330**, 642
Ferrarese L, 2002, ApJ, **578**, 90
Ferrarese L, Cote P, Bonta E. D. et al, 2006, ApJ, **644**, 21
Flynn C, Gould A, Bahcall J. N, 1996, ApJ, **466**, 55
Freudenreich H. T, 1998, ApJ, **492**, 495
Gnedin O. Y, Ostriker J. P, 1999, ApJ, **513**, 626
Goerdt T, Gnedin Y. O, Moore B, Diemand J, Stadel J, 2007, MNRAS, **375**, 191
Goerdt T, Moore B, Read J. I, Stadel J, Zemp M, 2006, MNRAS, **368**, 1073

Gould A, Flynn C, Bahcall J. N, 1998, ApJ, **503**, 798

Gould A, Rix H. W, 2000, ApJ, **532**, 29

Green A. M, Goodwin S. P, 2007, MNRAS, **375**, 1111

Haşegan M, Jordan A, Cote P. et al, 2005, ApJ, **627**, 203

Hayashi E, Navarro J. F, Power C. et al, MNRAS, **355**, 794

Hernandez X, Gilmore G, 1998, MNRAS, **297**, 517

Hernquist L, 1990, ApJ, **356**, 359

Hernquist L, Weinberg M. D, 1989, MNRAS, **238**, 407

Hilker M, Infante L, Viera G. et al, 1999, A&AS, **134**, 75

Hockney R. W, Eastwood J. W, 1981, Computer Simulations using Particles, McGraw-Hill

Hofmann S, Schwarz D. J, Stöcker H, 2001, PhRvD, **64**, 083507

Hogan C. J, Dalcanton J. J, 2000, PhRvD, **62**, 3511

Holmberg J, Flynn C, 2000, MNRAS, **313**, 209

Hut P, Makino J, 1999, Science, **283**, 501

Huxor A.P, Tanvir N.R, Irwin M.J, R. Ibata R, 2005, MNRAS, **360**, 993

Ivezić Ž, Goldston J, Finlator K, Knapp G. R. et al, 2000, AJ, **120**, 963

Jeans J. H, 1919, Phil. Trans. Roy. Soc. London A, **218**, 157

Jernighan J. G, Porter D. H, 1989, ApJS, **71**, 871

Jones J. B, Drinkwater M. J, Jurek R. et al, 2006, AJ, **131**, 312

Just A, Peñarrubia J, 2005, A&A, **431**, 861

Kalnajs A. J, ed. Lecar M, 1972, Gravitational N-Body Problem

Kazantzidis S, 2005, PhD thesis, Univ. Zürich

Kazantzidis S, Magorrian J, Moore B, 2004, ApJ, **601**, 37

Kazantzidis S, Mayer L, Mastropietro C, et al, 2004, ApJ, **608**, 663

Kazantzidis S, Moore B, Mayer L, 2003, astro-ph/0307362

Kaufmann T, Mayer L, Wadsley J, Stadel J, Moore B, 2006, MNRAS, **370**, 1612

Kaufmann T, Mayer L, Wadsley J, Stadel J, Moore B, 2007, MNRAS, **375**, 53

Kleyna J. T, Wilkinson M. I, Gilmore G, Evans N. W, 2003, ApJ, **588**, 21, Erratum-ibid, 2003, **589**, 59

King I. R, 1966, AJ, **71**, 64

Klypin A, Zhao H. S, Somerville R. S, 2002, ApJ, **573**, 597

Koushiappas S. M, 2006, PhRvL, **97**, 191301

Kuijken K, Gilmore G, 1989, MNRAS, **239**, 605

Lake G, 1990, Nat, **346**, 39

Lin D. C. N, Tremaine S, 1983, ApJ, **264**, 364

Łokas E. L, 2002, MNRAS, **333**, 697

Lotz J. M, Miller B. W, Ferguson H. C, 2004, ApJ, **613**, 262

Lotz J. M, Telford R, Ferguson H. C, et al, 2001, ApJ, **552**, 572

Lynden-Bell D, Kalnajs A. J, 1972, MNRAS, **157**, 1

Ma C. P, Bertschinger E, 1995, ApJ, **455**, 7

Mackey A. D, Gilmore G. F, 2003, MNRAS, **340**, 175

Mainini R, Macciò A. V, Bonometto S. A, Klypin A, 2003, ApJ, **599**, 24

Markevitch M, Gonzalez A. H, Clowe D, 2004, ApJ, **606**, 819

Marquardt D. W, 1963, J. Soc. Ind. Appl. Math, **11**, 431

Merritt D, Piatek S, Zwart S. P, Hemsendorf M, 2004, ApJ, **608**, 25

Michie R. W, 1963, MNRAS, **125**, 127

Michie R. W, Bodenheimer P. H, 1963, MNRAS, **126**, 269

Milosavljević M, Merritt D, Rest A, van den Bosch F. C, 2002, MNRAS, **331**, 51

Moore B, 1993, ApJ, **413**, L93

Moore B, 1994, Nat, **370**, 629

Moore B, Diemand J, Stadel J, Quinn T, 2005, astro-ph/0502213

Moore B, Ghigna S, Governato F, et al, 1999a, ApJ, **524**, 19

Moore B, Quinn T, Governato F, Stadel J, Lake G, 1999b, MNRAS, **310**, 1147

Monaghan J. J, 1992, ARAA, **30**, 543

Navarro J. F, Frenk C. S, White S. D. M, 1996, ApJ, **462**, 563

Oh K. S, Lin D. N. C, 2000, ApJ, **543**, 620

Oh K. S, Lin D. N. C, Richer H. B, 2000, ApJ, **531**, 727

Ortolani S, Bica E, Barbuy B, 1995, A&A, **300**, 726

Peñarrubia J, Just A, Kroupa P, 2004, MNRAS, **349**, 747

Picaud S, Robin A. C, 2004, A&A, **428**, 891

Plummer H. C, 1911, MNRAS, **71**, 460

Plummer H. C, 1915, MNRAS, **76**, 107

Press W. H, Teukolsky S. A, Vetterling W. T, Flannery B. P, 1992, Numerical recipes in C. The art of scientific computing, Cambridge University Press

Ravindranath S, Ho L. C, Filippenko A. V, 2002, ApJ, **566**, 801

Read J. I, Gilmore G, 2005, MNRAS, **356**, 107

Read J. I, Goerdt T, Moore B. et al, 2006, MNRAS, **373**, 1451

Regan M. W, Vogel S. N, 1994, ApJ, **434**, 536

Rhee G, Valenzuela O, Klypin A, Holtzman J, Moorthy B, 2004, ApJ, **617**, 1059

Saha P, 1992, MNRAS, **254**, 132

Sánchez-Salcedo F. J, Reyes-Iturbide J, Hernandez X, 2006, MNRAS, **370**, 1829

Searle L, Zinn R, 1978, ApJ, **225**, 79

Sharina M. E, Puzia T. H, Makarov D. I, 2005, A&A, **442**, 85

Spagna A, Carollo D, Lattanzi, M. G, Bucciarelli B, 2004, A&A, **428**, 451

Spergel D. N, Verde L, Peiris H. V. et al, 2003, ApJS, **148**, 175

Spinnato P. F, Fellhauer M, Portegies Zwart S. F, 2003, MNRAS, **344**, 22

Spitzer L, 1987, Dynamical Evolution of Globular Clusters (Princeton, NJ, Princeton University Press)

Stadel J, 2001, PhD thesis, Univ. Washington

Statler T. S, 1991, ApJ, **375**, 544

Strom S. E, Strom K. M, Wells D. C. et al, 1981, ApJ, **245**, 416

Tremaine S. D, 1976, ApJ, **203**, 345

Tremaine S. D, 1995, AJ, **110**, 628

Tremaine S. D, Ostriker J. P, Spitzer L, 1976, ApJ, **196**, 407

Tremaine S. D, Weinberg M. D, 1984, MNRAS, **209**, 729

Umemura M, Ikeuchi S, 1985, ApJ, **299**, 583

Vittorio N, Silk J, 1984, ApJ, **285**, 39

Wadsley J, Stadel J, Quinn T, 2004, NewA, **9**, 137

Walker M. G, Mateo M, Olszewski E. W, et al, 2006, AJ, **131**, 2114

Weinberg M. D, 1986, ApJ, **300**, 93

Weinberg M. D, 1998, MNRAS, **297**, 101

Weinberg M. D, 1999, AJ, **117**, 629

Weinberg M. D, Katz N, 2007a, MNRAS, **375**, 425

Weinberg M. D, Katz N, 2007b, MNRAS, **375**, 460

White S. D. M, 1976, MNRAS, **174**, 467

White S. D. M, 1983, ApJ, **274**, 53

Zaritsky D, White S. D. M, 1988, MNRAS, **235**, 289

Zemp M, 2006, PhD thesis, ETH Zürich

Zhao H, 1996, MNRAS, **278**, 488

Zhao H. S, Hooper D, Angus G. W, Taylor J, Silk J, 2007, ApJ, **654**, 697

Zhao H. S, Taylor J, Silk J, Hooper D, 2005, astro-ph/0502049

Acknowledgements

I am very grateful to:

- my PhD thesis supervisor Prof Ben Moore for providing me with the interesting topic of this thesis. His inexhaustible source of new scientific ideas not only deeply impressed me but also helped me a lot finishing this thesis quickly. His social involvement contributed much to the fact that I always enjoyed my time here in Switzerland.

- Dr Joachim Stadel and Doug Potter for providing the superb support for all the hard- and software without which this work would not have been possible.

- All other coauthors of my publications: Dr Justin Read, Prof Oleg Gnedin, Dr Jürg Diemand, Prof George Lake, Dr Marcel Zemp and Andrew Pontzen for the excellent work.

- my parents Dr Ludwig and Dr Ursula Goerdt for their continuous mental and financial support.

- my siblings Thomas Goerdt, Dr Katrin Kreutzer and Dr Alexander Goerdt, for always giving valuable advice, up to continuously planning my career rigorously.

- Eva Poulsen for carefully reading the manuscript.

- my office mate Simone Weinmann for the endless discussions about credits and debits of science and industry.

- all the former and contemporary members of the Institute of Theoretical Physics for the nice atmosphere at lunch and coffee breaks, especially: Dr Andreas Kaiser for being from Westphalia, Dr Christoph Meier for the excellent food, Dr Sabine Schilling for the nice theatre nights, Dr Tobias Kaufmann for the unforgettable Helsinki nights, Dr Tobias Huber for watching football matches together, Dr Daniel Maître for teaching me how to ski, Dr Fabiana De Luca for the amazing trip to Croatia, Beat Toedtli for the nice opera nights, Christian Kurz for the inspiration, Nico Greiner and Tobias Motz for the unforgettable Oxa nights.

- the people outside of physics, which made life in Zürich more enjoyable for me: Martin Eggenberger, Simone Gundermann, Karsten Hartmann, Seraphima Hoffmann, Daria Hofmann, Mustafa Karaman, Bori Kovács and Can Kut.
- my *homebase* in Bochum: Björn Beulmann, Boris Bobe, Denis Brune, Sebastian Erdmann, Aidan Hogan, Jacek Janski, Alexander John, Till Knaudt, Saskia Schmidt and Daniel Stark.

Thank you so much.

Tobias Goerdt

Personal data

Date of birth : 25th May 1980
Place of birth : Bochum, Germany
Nationality : German

Education

09/2004 - 09/2007:	University of Zürich, Switzerland Dr. sc. nat. (PhD) in Theoretical Physics Thesis title: *Dynamical friction: Fact or fiction?* Supervisor: Prof Ben Moore
09/2000 - 06/2004:	University of St Andrews, Scotland
23rd June 2004:	MSci in Astrophysics Thesis title: *Differential rotation of solar type stars* Supervisor: Prof Andrew Collier Cameron
08/1999 - 09/2000:	Compulsory service: Alternative service at Janusz-Korczak-Schule, Bochum School for mentally handicapped children
08/1990 - 05/1999:	Gymnasium am Ostring, Bochum Highers: mathematics, chemistry, religion, music
17th May 1999:	Abitur

Languages

German:	Native language
English:	Business fluent
Spanish:	Conversant